CWP-091
October 1989

Modeling and Inversion in the Ocean Waveguide Using Born and Rytov Approximations

by

Linda Boden

— Doctoral Thesis —

Center for Wave Phenomena
Department of Mathematics
Colorado School of Mines
Golden, Colorado 80401
Phone (303) 273-3557

TABLE OF CONTENTS

	Page
ABSTRACT	iv
INTRODUCTION	1
1. MODELING THE SOUND FIELD IN THE OCEAN WAVEGUIDE	3
1.1 Introduction	3
1.2 Numerical Models	3
1.3 Examples of Waveguide Propagation	5
2. THE FORWARD MODEL	8
2.1 Introduction	8
2.2 The Background Solution	8
2.3 The Distorted-Wave Born (DWB) Solution	9
2.4 The Distorted-Wave Rytov (DWR) Solution	10
2.5 Discussion of Errors	11
2.6 Explicit Solutions	12
3. CONSTANT BACKGROUND TEST CASES	14
3.1 Introduction	14
3.2 Constant Velocity Waveguide	14

ACKNOWLEDGMENTS 43

REFERENCES 44

APPENDIX A: Derivation of the Normal Mode Field Representation 47

APPENDIX B: Derivation of the Range Dependent Solution 50

APPENDIX C: Derivation of the Full DWR Solution 53

APPENDIX D: Evaluation of the Range-Dependent Solution 55

APPENDIX E: Modal Decomposition of the Perturbative Solutions 60

FIGURES 63

INTRODUCTION

In the last decade, the inverse problem in the ocean has received considerable attention from the ocean acoustics and oceanographic scientific communities. In 1979, Munk and Wunsch proposed a inverse method that is now known as ocean acoustic tomography. This technique consists of measuring ray travel times between source-receiver pairs and inverting these to determine perturbations to an assumed background profile. Many experiments have been conducted proving the validity and usefulness of the technique as well as its limitations (for some of the earliest results see Spiesberger, Spindel and Metzger 1980; Brown et al. 1980; Munk and Wunsch 1982; Spiesberger 1983; Munk and Wunsch 1983). Because the travel time equations are linearized, the background or guess profile must be known to within $\sim$2 m/s of the true profile. The inversion methodology is in the class known as indirect inversion techniques; a background profile is chosen, the forward model is run repeatedly and the results compared to the experimental data. In other words, the technique is based on iteration of a forward model.

In this thesis, we attempt a different approach and formulate a direct inversion algorithm. Using first order perturbation expansions, the scattered field data as a function of frequency and the profile perturbation as a function of the phase can be directly related as a Fourier transform pair. However, because the inversion is based on the forward model we first must investigate the range of validity of the perturbative solutions in the ocean waveguide. The theoretical analysis of the forward model is done in chapter 2 and numerical examples are presented in chapters 3 and 4.

We study two perturbative solutions; the Born amplitude expansion (Born 1926) and the Rytov phase expansion (Rytov 1937; Chernov 1960). The background field, on which the perturbative solutions are based, is chosen to be the proper mode solution; the discrete part of the normal mode solution. The normal mode representation, which contains both the discrete and continuous spectrum, is exact under certain restrictions (see chapter 1). In the far field, the continuous spectrum can be neglected and the proper or propagating modes are the main contribution to the solution.

In order to obtain simple error estimates for a waveguide geometry, we first investigate the perturbative solutions in a constant background environment. When the background is chosen to be a constant, the solutions are known simply as the Born and the Rytov approximations.

Although the maximum deviation in the sound speed in the deep ocean is only about 10% over the entire waveguide, the background velocity structure in the ocean cannot be assumed constant. Therefore, we must choose a depth-dependent background sound speed structure to obtain valid zeroth order solutions in the refractive ocean waveguide. In this case, the perturbative approximations are called the distorted-wave Born (DWB) and the distorted-wave Rytov (DWR) to distinguish the solutions from those based on a homogeneous background.

1. MODELING THE SOUND FIELD IN THE OCEAN WAVEGUIDE

1.1 Introduction

The underwater sound channel or SOFAR (Sound Fixing And Ranging) channel, discovered in the early 1940's by M. Ewing and J.L. Worzel (1948), is the most characteristic feature of the deep ocean at moderate and equatorial latitudes. This acoustic channel is formed by temperature, pressure and salinity variations in the ocean. The temperature and salinity decrease below the ocean surface causing a corresponding decrease in the sound speed. At approximately 1 kilometer (km) below the surface, a leveling off of the temperature decrease and steadily increasing pressure causes a nearly linear increase in the sound speed as the depth is further increased. Thus, an acoustic waveguide is created in which sound can propagate, through refraction, for hundreds of kilometers.

Although the ocean has both regular and random inhomogeneities, this thesis will only deal with regular or deterministic effects; in particular, propagation in the underwater sound channel. The sound field is modeled using the acoustic wave equation assuming a pressure release surface and either a rigid bottom or an infinite half space below the waveguide bottom. We will use a point cylindrical monochromatic source representation and assume the medium is cylindrically symmetric. In general, the sound speed is a function of both depth and range.

In the next section, we briefly discuss the attributes of several numerical propagation models in use today (for a summary of numerical propagation loss models, see DiNapoli and Deavenport 1979); in particular, the choice of a background model on which the perturbative solutions are based. The last section of this chapter illustrates the variation of the sound field as a function of source depth and frequency for several sound speed profiles. These plots are generated from the proper or discrete mode solution; the background model used throughout this thesis.

1.2 Numerical Models

A variety of propagation codes have been developed to model the sound field in the ocean. Each is valid within a certain range of chosen medium parameters. Including even a condensed discussion of all the computer codes currently in use is impossible. Instead, we first briefly describe two propagation loss models; the classical ray method and the parabolic approximation to the Helmholtz equation. Next, we focus on a third, the discrete mode solution, which is the background model used in this thesis. The rationale for basing the perturbative solutions on this particular model will be made clear in the remainder of this section.

The classical ray equations and the parabolic approximation are derived based on assumptions about the propagation environment. The ray equations are formed from a high frequency assumption and by neglecting diffraction effects (Born and Wolf 1965).

1.3 Examples of Waveguide Propagation

In this section, several examples of waveguide propagation are illustrated with the use of color pixel maps. The field strength in the waveguide is represented by the transmission loss in decibels (dB). The transmission loss is defined by $-20\log_{10}|P/P_{ref}|$, where P is the pressure field and P_{ref} is the field strength at 1 meter (m) from the source.

In order to illustrate the focusing effect that the SOFAR channel has on sound propagation, we compare the propagation loss in a constant velocity waveguide to that of a bilinear profile with a sound speed minimum at 1 km depth. Effects of source placement in depth and changes in the source frequency are also compared. Before illustrating the acoustic field behavior for different waveguide geometries, we first briefly discuss the discrete modal solution.

Recall that we are solving the Helmholtz equation. If the sound speed in the waveguide is constant or at most depends on depth, the homogeneous form of the equation is separable. The range solution is an outgoing wave Hankel function. The vertical wave function, ψ, satisfies the equation

$$\left[\frac{d^2}{dz^2} + \left(k_o^2 n^2(z) - \xi^2\right)\right]\psi = 0$$

with boundary conditions at the surface and bottom of the ocean. The index of refraction, $n(z)$, is given by $c_o/c(z)$ and the reference wavenumber is $k_o = 2\pi f/c_o$; c_o is the reference sound speed, usually chosen as the minimum value in the waveguide, $c(z)$ is the depth-dependent sound speed and f is the source frequency. Because we are solving a boundary value problem, there are non-trivial solutions, ψ_n only for a discrete set of values of the parameter, ξ_n. Therefore, the ψ_n are the eigenfunctions and the ξ_n are the eigenvalues of the problem. As will be illustrated, the number of eigenvalues contributing to the solution depends on the boundary conditions, the source frequency and the sound speed structure in the waveguide.

Figures 1 and 2 illustrate the transmission loss in a constant velocity waveguide for source frequencies of 25 and 100 Hertz (Hz), respectively. (The maximum allowable phase velocity is chosen to be 1600 m/s.) The source is placed at a depth of 500 m. We have a pressure release surface ($P = 0$ at the ocean surface) and a hard bottom ($P_z = 0$, where the subscript denotes the depth derivative).

Because the velocity is constant over the full waveguide, there is no refraction; the energy propagates through surface and bottom reflections. We have total internal reflection due to the bottom boundary condition; in general, the angular aperture extends from 0 to $\pm 90^\circ$ measured from the horizontal at the source position. As is evident from the isolated bright spots, the energy focuses only locally.

The different structure in Figures 1 and 2 is due solely to the change in source frequency. At 25 Hz, there are 50 modes contributing to the field, while at 100 Hz, we have 4 times as many. A higher source frequency does not imply higher angles but

In subsequent chapters, we will investigate the behavior of two perturbative solutions to the total acoustic field in which the background solution is chosen to be the discrete part of the normal mode representation. Although the solutions and their errors are initially analyzed in several constant velocity waveguides, we stress that a constant background solution is not a valid zeroth order solution in a refractive ocean waveguide. The analysis is done simply to better understand and predict the validity of the solutions in the inhomogeneous ocean environment.

wish to approximate, ∇^2 is the cylindrical Laplacian, $n(r,z) = c_o/c(r,z)$ is the normalized sound speed in a depth and range dependent environment, and $k_o = \omega/c_o$ is the reference wavenumber. The source is located at a range $r = r_o$ and a depth $z = z_o$. We consider the general case of $r_o \neq 0$ in order to construct the scattered field.

The choice of the reference sound speed, c_o, is arbitrary. Because the Helmholtz equation is independent of c_o, so are its solutions. From this it follows that any approximate solution must depend only weakly on the choice of the reference sound speed in order to be a valid representation of the total field.

The distorted-wave perturbative solutions are derived with the assumption that information regarding the gross (i.e. purely depth-dependent) sound speed structure of the ocean waveguide is known. Using this knowledge, a background field, $P_o(k_o,r,r_o,z,z_o)$, which satisfies

$$\left[\nabla^2 + k_o^2 n_o^2(z)\right] P_o(k_o,r,r_o,z,z_o) = -\frac{\delta(r-r_o)\delta(z-z_o)}{2\pi r}, \tag{2}$$

can be calculated. Since $n_o(z)$ is known, the P_o field can be thought of as an *incident* field in this inhomogeneous environment. Because the oceanic sound speed structure has an inherent depth variability, but depends weakly on range, the background, $n_o(z)$, is chosen to be strictly depth-dependent, but is 'close' (in a sense specified below) to the true index of refraction, $n(r,z)$, for all ranges and depths. By perturbing around the incident field solution, approximate solutions to the total field can be formed.

2.3 The Distorted-Wave Born (DWB) Solution

The DWB solution is formed by expanding the total field, $P(k_o,r,r_o,z,z_o)$, and the index of refraction, $n^2(r,z)$, in powers of a small parameter, ϵ. The total field, which satisfies Eq. (1), is written as

$$P(k_o,r,r_o,z,z_o) = P_o + \epsilon P_1 + \cdots \tag{3}$$

and the square of the index of refraction as

$$n^2(r,z) = n_o^2(z) + \epsilon n_1(r,z) + \cdots \tag{4}$$

Substituting Eqs. (3) and (4) into Eq. (1), equating powers of ϵ and retaining terms only up to $O(\epsilon)$ results in two equations. The $O(\epsilon^o)$ equation is Eq. (2). and the $O(\epsilon)$ equation is

$$\left[\nabla^2 + k_o^2 n_o^2(z)\right] P_1(k_o,r,r_o,z,z_o) = -k_o^2 n_1(r,z) P_o\,. \tag{5}$$

Because Eq. (5) is the Helmholtz equation with a source term, and our Green's function is the incident field, P_o, the solution to Eq. (5) is formed by integrating over all source points. The field solution is independent of theta due to cylindrical

where $\phi_1 = P_s/P_o$ is the first term in a formal phase expansion,

$$\Phi = \phi_1 + \phi_2 + \cdots \tag{12}$$

and ϕ_1 is $O(\epsilon)$, ϕ_2 is $O(\epsilon^2)$, etc. The full DWR field is derived in Appendix C.

Because we are mainly interested in the behavior of the first order approximations, the terms DWB and DWR will denote the first order approximations unless otherwise indicated.

2.5 Discussion of Errors

As is evident from Eqs. (7) and (11) and the derivation of the DWR from the DWB, the first order solutions are closely related. However, as derived by Keller (1969) for the constant background solutions, and by Belykin (1985) for the distorted-wave solutions, the first order relative error in the two approximations is quite different. By relating terms in the series in Eqs. (3) and (12), Beylkin establishes the relative DWB error

$$\frac{P - P_1^{(B)}}{P} = O\left[\phi_2 - \frac{1}{2}{\phi_1}^2\right], \tag{13}$$

while the relative DWR error is

$$\frac{P - P_1^{(R)}}{P} = O\left[\phi_2\right]. \tag{14}$$

Although both expressions are order ϵ^2, the DWB error has an extra term, ${\phi_1}^2$. Since (as we shall see later) both ϕ_1 and ϕ_2 depend on range to the first power, the DWB error term is $O(\epsilon^2 r^2)$, while the DWR is $O(\epsilon^2 r)$. Because of this, the amplitude of the DWB field will grow like r as we propagate in range. The DWR is expected to give a better approximation to the transmitted field.

We must keep in mind, however, that these are only first order errors and, in addition, they are based on the assumption that the scattered field is much less than the incident field. As previously discussed, the DWB requires that $| P_s/P_o | \ll 1$ in order for the approximation to be valid. But, although the DWR was derived from the DWB using this assumption, the latter is not a necessary condition for the validity of the DWR.

However, the DWR approximation has additional terms which are not evident in the simple derivation of the DWR from the DWB. In Appendix C, where the full DWR approximation is derived, the assumption is made that the integral of $[\nabla\Phi]^2$, where Φ is the full DWR phase, is of lower order. This term will be of $O(\epsilon^2)$ only if the phase gradient is small; we can have no sharp discontinuities in the complex phase term. This makes the behavior of the DWR difficult to predict because the above error estimate is locally inaccurate if the ratio P_s/P_o is changing rapidly.

If $\xi_m = \xi_n$ in Eq. (17), then we write the solution symbolically as

$$P_1^{(B)}(k_o, r, 0, z, z_o) = P_o + P_{sn}\,. \tag{18.a}$$

P_{sn}, the scattered field term for $\xi_m = \xi_n$, is given by

$$P_{sn}(k_o, r, r_o, z, z_o) = -\frac{ik_o^2 r}{8}\int_o^h \sum_n \psi(z', \xi_n)\psi(z, \xi_n) n_1(z')$$

$$\cdot\, \psi(z', \xi_n)\psi(z_o, \xi_n)\frac{H_1^{(2)}(\xi_n r)}{\xi_n}\, dz'\,. \tag{18.b}$$

where $H_1^{(2)}(\xi_n r)$ is the first order Hankel function. If $\xi_m \neq \xi_n$ then

$$P_1^{(B)}(k_o, r, 0, z, z_o) = P_o + P_{snm} \tag{18.c}$$

and the scattered field defined as P_{snm} is

$$P_{snm}(k_o, r, r_o, z, z_o) = \frac{ik_o^2}{4}\int_o^h \sum_n \psi(z', \xi_n)\psi(z, \xi_n)\, n_1(z')$$

$$\cdot \sum_m \psi(z', \xi_m)\psi(z_o, \xi_m)\frac{H_o^{(2)}(\xi_m r)}{{\xi_m}^2 - {\xi_n}^2}\, dz'\,. \tag{18.d}$$

The DWR, formed from the DWB as previously described, is

$$P_1^{(R)}(k_o, r, 0, z, z_o) = P_o \exp\left[\frac{P_{sn}}{P_o}\right] \tag{19.a}$$

if $\xi_m = \xi_n$. Similarly, for $\xi_m \neq \xi_n$, we obtain

$$P_1^{(R)}(k_o, r, 0, z, z_o) = P_o \exp\left[\frac{P_{snm}}{P_o}\right]. \tag{19.b}$$

In the next chapter, the above equations will be evaluated for several constant velocity profiles (i.e. the depth dependent solutions are found explicitly) and the behavior of the Born and Rytov in these simple cases is investigated. Although not representative of the velocity structure in an ocean waveguide, analyzing these cases gives an indication of how the DWB and DWR approximations will behave in a complex environment.

wavenumbers are the λ_n. The sine eigenfunctions arise from a particular choice of boundary conditions. The pressure field is chosen to be zero at the surface and the z-derivative (since we have a flat bottom) to be zero at the ocean bottom. The factor $(2/h)^{1/2}$ is the normalization constant for this set of orthonormal eigenfunctions.

The initial guess field, for the constant velocity waveguide with index of refraction, n_o is given by

$$P_o(k_o,r,0,z,z_o) = \frac{i}{4}\sum_n \frac{2}{h}\sin\lambda_n z_o \sin\lambda_n z\, H_o^{(2)}(\xi_n r)\,, \tag{21}$$

where the horizontal wavenumber eigenvalues for the background solution are given by the ξ_n which are defined by ${\xi_n}^2 = k_o^2 n_o^2 - {\lambda_n}^2$. As is evident from Eqs. (20) and (21), the eigenfunctions are identical. In a constant velocity waveguide, the only difference in the two solutions are the values of the horizontal wavenumbers.

From Eq. (17), the Born solution in a constant velocity medium is given by

$$\begin{aligned} P_1^{(B)}(k_o,r,0,z,z_o) = P_o &- \frac{k_o^2 n_1 \pi}{2h^2}\int_o^r\int_o^h \sum_n \sin\lambda_n z \sin\lambda_n z'\, H_o^{(2)}(\xi_n r) J_o(\xi_n r') \\ &\cdot \sum_m \sin\lambda_m z' \sin\lambda_m z_o\, H_o^{(2)}(\xi_m r') r'\, dr'\, dz' \\ &- \frac{k_o^2 n_1 \pi}{2h^2}\int_r^\infty\int_o^h \sum_n \sin\lambda_n z \sin\lambda_n z'\, H_o^{(2)}(\xi_n r') J_o(\xi_n r) \\ &\cdot \sum_m \sin\lambda_m z' \sin\lambda_m z_o\, H_o^{(2)}(\xi_m r') r'\, dr'\, dz' \end{aligned} \tag{22}$$

where n_1, the constant velocity perturbation, is the difference, $n_c^2 - n_o^2$, in the squares of the true and background refractive indices.

Because the perturbation is constant, both the range and depth integrals can be evaluated explicitly. Evaluating the range integrals (see Appendix D) and following the notation of Eqs. (18), the Born scattered field for $\xi_n = \xi_m$ is

$$P_{sn}(k_o,r,r_o,z,z_o) = \frac{ik_o^2 n_1 r}{2h^2}\int_o^h \sum_n \sin\lambda_n z \sin^2\lambda_n z' \sin\lambda_n z_o \frac{H_1^{(2)}(\xi_n r)}{\xi_n}\, dz'\,. \tag{23.a}$$

For $\xi_n \neq \xi_m$, we obtain

$P_{snm}(k_o,r,r_o,z,z_o)$

single mode only, $P_o(k_o,r,0,z,z_o)$ can be written explicitly as

$$P_{o1}(k_o,r,0,z,z_o) = \frac{i}{2h}\sin\lambda_1 z \sin\lambda_1 z_o \, H_o^{(2)}(\xi_1 r) \tag{27}$$

where $P_{o1}(k_o,r,0,z,z_o)$ denotes the field expression for the first mode, λ_1 is the corresponding vertical wavenumber while ξ_1 is the corresponding horizontal wavenumber. This notation will be used throughout in deriving the subsequent single mode expressions.

Using Eq. (27), the first phase term can now be written

$$\phi_{11}(k_o,r,0,z,z_o) = \frac{k_o^2 n_1 r}{2\, H_o^{(2)}(\xi_1 r)} \, \frac{H_1^{(2)}(\xi_1 r)}{\xi_1} \, . \tag{28}$$

Using the asymptotic forms of the Hankel functions

$$H_o^{(2)}(\xi_1 r) = \left[\frac{2}{\pi\xi_1 r}\right]^{1/2} e^{-i(\xi_1 r - \frac{\pi}{4})}$$

$$H_1^{(2)}(\xi_1 r) = \left[\frac{2}{\pi\xi_1 r}\right]^{1/2} e^{-i(\xi_1 r - \frac{3\pi}{4})}, \tag{29}$$

and canceling terms, $\phi_{11}(k_o,r,0,z,z_o)$ is given by

$$\phi_{11}(k_o,r,0,z,z_o) = \frac{ik_o^2 n_1 r}{2\xi_1} \tag{30}$$

so the gradient of ϕ_{11} is just

$$\nabla\phi_{11}(k_o,r,0,z,z_o) = \frac{ik_o^2 n_1}{2\xi_1}\hat{r} \, . \tag{31}$$

Substituting Eq. (31) into Eq. (26) and evaluating the range integral for a single mode, ϕ_{21} becomes

$$\phi_{21}(k_o,r,0,z,z_o) = -\frac{k_o^2 n_1 r}{H_o^{(2)}(\xi_1 r)} \frac{H_1^{(2)}(\xi_1 r)}{\xi_1 h} \left[\frac{k_o^2 n_1}{2\xi_1}\right]^2 \int_o^h \sin^2\lambda_1 z' \, dz' \, . \tag{32}$$

Performing the depth integration and canceling like factors, the second phase term becomes

$$\phi_{21}(k_o,r,0,z,z_o) = -\frac{irk_o^4 n_1^2}{8{\xi_1}^3} \tag{33}$$

section 3.2.2 are valid for any profile perturbation, the Rytov error estimate is correct only if the scattered field is small with respect to the incident field.

In the next section, the numerical results for a constant velocity waveguide are presented and the analytical results of this section will be verified.

3.3 Constant Velocity Waveguide Example

The parameters for the constant velocity waveguide example are given in Table 1. The true and background profiles are illustrated in Figure 7. The transmission loss curves for the profiles are illustrated in Figure 8. The transmission loss is defined as $-20\log(\frac{|P|}{|P_{ref}|})$, where P is the complex field and P_{ref} is the field at 1 meter from the source.

Because the perturbation is small and the eigenfunctions are identical in the constant velocity case, the true and background curves nearly overlay each other, except perhaps at the "nulls" where the modes have interfered destructively creating a minimum amplitude. The amplitude behavior of the Born and Rytov solutions can be qualitatively predicted by studying Figure 9; the ratios $|P_s/P_o|$ vs. range. The ratios match until approximately 5 km; this is the regime in which

Table 1. Input Parameters: Test Case 1

INPUT PARAMETERS: TEST CASE 1		
Range		1.-50. km
Source Depth		500. m
Receiver Depth		500. m
Source Frequency		25. Hz
	Depth (m)	Sound Speed (m/s)
True profile	0.	1500.
	1500.	1500.
Guess profile	0.	1501.
	1500.	1501.
Maximum Perturbation		1. m/s
Perturbation Width		1500. m

recalculated Born and Rytov coefficients.

The real part of the Born coefficients are used to recalculate the Born transmission loss. The resultant curve, labeled "MDB" is illustrated in Figure 17 along with the true transmission loss and the original Born solution. As expected, the growth of the Born solution with range has disappeared. To recalculate the Rytov solution, we use the amplitude of the mode coefficients. The result, illustrated in Figure 18, and labeled "MDR" exhibits little change from the original Rytov solution.

In reviewing the results of this section, we conclude that although the amplitude of the Born approximation is strongly affected by a shift in the sound speed over the full waveguide, the Rytov approximation is insensitive to a perturbation of this magnitude and extent. In the next section, we study several two-layer waveguides in order to determine the magnitude and extent of perturbations recoverable about a known background profile.

3.4 Two-Layer Waveguide

3.4.1 Derivation of the Solutions

The two-layer model used in this section is illustrated in Figure 19. The sound speed in the upper layer is defined to be c_1, while the sound speed in the lower layer is defined to be c_o, to match the constant velocity case. The reference wavenumbers are k_1 and k_o, respectively. The depth of the layer is z_1. The total field for this geometry is

$$P(k,r,0,z,z_o)$$

$$= \frac{i}{4}\sum_n A_n \frac{\cos\lambda_{on}(h-z_o)\cos\lambda_{on}(h-z_1)}{\sin\lambda_{1n}z_1} \sin\lambda_{1n}z\, H_o^{(2)}(\zeta_n r) \qquad 0<z<z_1$$

$$P(k,r,0,z,z_o)$$

$$= \frac{i}{4}\sum_n A_n \cos\lambda_{on}(h-z_o)\cos\lambda_{on}(h-z)\, H_o^{(2)}(\zeta_n r) \qquad z_1<z<h \qquad (38)$$

where A_n is given by

$$A_n = 2\lambda_{1n}\lambda_{on}\sin^2\lambda_{1n}z_1$$

$$\cdot\left[\lambda_{on}\cos^2\lambda_{on}(h-z_1)\left(z_1\lambda_{1n} - \sin\lambda_{1n}z_1\cos\lambda_{1n}z_1\right)\right.$$

3.4.2 Error Analysis

Following the analysis in section (3.2.2), we will derive the first order errors for the case of a single mode. From Eq. (40.a), the first phase term in a two-layer waveguide is

$$\phi_{11}(k_o,r,0,z,z_o) = \frac{ik_o^2 r n_1}{2h^2 P_o}\sin(\frac{\pi z}{2h})\sin(\frac{\pi z_o}{2h})\frac{H_1^{(2)}(\xi_1 r)}{\xi_1}\int_o^{z_1}\sin^2(\frac{\pi z'}{2h})\,dz' . \tag{41}$$

Using P_o from Eq. (21), the asymptotic form of the Hankel functions (Eq. (29)), and evaluating the integral, we obtain

$$\phi_{11}(k_o,r,0,z,z_o) = \frac{ik_o^2 r n_1}{2\xi_1}\left[\frac{z_1}{h} - \frac{\sin(\frac{\pi z_1}{h})}{\pi}\right]. \tag{42}$$

The gradient of ϕ_{11} is just

$$\nabla\phi_{11}(k_o,r,0,z,z_o) = \frac{ik_o^2 n_1}{2\xi_1}\left[\frac{z_1}{h} - \frac{\sin(\frac{\pi z_1}{h})}{\pi}\right]\hat{r}\,, \tag{43}$$

so, from Eq. (26), ϕ_{21} simply becomes

$$\phi_{21}(k_o,r,0,z,z_o) = -\frac{ik_o{}^4 r n_1^2}{8\xi_1{}^3}\left[\frac{z_1}{h} - \frac{\sin(\frac{\pi z_1}{h})}{\pi}\right]^2. \tag{44}$$

From Eqs. (42) and (44), the first order relative Born error is given by

$$\frac{P-P_1^{(B)}}{P} = O\left[-\left(\frac{ik_o{}^4 r n_1^2}{8\xi_1{}^3} + \frac{k_o{}^4 r^2 n_1^2}{8\xi_1{}^2}\right)\left(\frac{z_1}{h} - \frac{\sin(\frac{\pi z_1}{h})}{\pi}\right)^2\right] \tag{45}$$

and the first order relative Rytov error is

$$\frac{P-P_1^{(R)}}{P} = O\left[-\frac{ik_o{}^4 r n_1^2}{8\xi_1{}^3}\left(\frac{z_1}{h} - \frac{\sin(\frac{\pi z_1}{h})}{\pi}\right)^2\right]. \tag{46}$$

The behavior of the first order relative errors in range thus depends critically on the width of the layer in depth. If z_1 is small compared to h, the sine can be expanded around $z_1/h = 0$ and the errors now look like

Superficially, the modal decompositions seem to suggest the same type of behavior as the first order errors. However, as will be seen in the next section, the quantity $\tilde{A}$ plays a significant role in determining the validity of the solutions.

3.5 Two-Layer Waveguide Examples

In this section, we discuss two velocity models; the first has a 100 m layer and the second a 400 m layer. The parameters for the first model are given in Table 2.

The true and background profiles are illustrated in Figure 20 and the transmission loss curves in Figure 21. Again, the guess overlays the true profile almost exactly due to the smallness of the perturbation and also its minimal extent.

We will first qualitatively predict the behavior of the Born and Rytov solutions by studying the ratio $|P_s/P_o|$ vs. range in Figure 22. Both of the

Table 2. Input Parameters: Test Case 2

INPUT PARAMETERS: TEST CASE 2		
Range		1.-50. km
Source Depth		500. m
Receiver Depth		500. m
Source Frequency		25. Hz
	Depth (m)	Sound Speed (m/s)
True profile	0.	1500.
	100.	1500.
	100.	1501.
	1500.	1501.
Guess profile	0.	1501.
	1500.	1501.
Maximum Perturbation		1. m/s
Perturbation Width		100. m

ratios are less than 1/4 (except at the spikes) and they match in amplitude except at the spikes which occur at the nulls in the amplitude of the incident field. This is a case where we are in the range of validity of both solutions; the ratio of the scattered to the incident field is small. Therefore, the solutions are expected to generate similar results.

To estimate the percentage change in the mode functions, we look at the change in the mode coefficient over the waveguide as the layer width is systematically increased. From Figure 29, we can estimate that a 400 meter layer with a 1 m/s change in the sound speed, results in approximately a 14% change in the mode coefficient as compared to the constant velocity case. It is evident, then, that a small change in the sound speed over 28% of the waveguide causes a large change in the value of the eigenfunctions and a corresponding change in the true and background transmission loss curves.

To predict the behavior of the Born and Rytov solutions, we again study the ratio of the scattered to the incident field for both approximations. From Figure 30 and a closeup in Figure 31, we see that the ratio in both cases has exceeded 1/4 by a range of approximately 13 km. Therefore, the Born solution is expected to grow for ranges greater than 13 km. The behavior of the Rytov solution is difficult to predict. Although the Rytov ratio also exceeds 1/4, we saw in the constant velocity case that a large ratio did not affect the validity of the Rytov solution.

The Born and true transmission loss plots are illustrated in Figure 32 and the Rytov and true in Figure 33. As expected, there is a slight growth in the Born solution. The Rytov solution is somewhat more accurate (see the relative error versus range in Figure 34), but again does not match the true solution; in addition, a spike in the solution appears at about 5 km in the same location as one of the spikes in the $|P_s/P_o|$ of Figure 30.

We now see the effect that a 14% change in the true and background eigenfunctions has on the accuracy of the Born and Rytov solutions. We also see the failure of the error predictions to account for this type of change. Only the factor $\tilde{A}$ in the modal decompositions gives an indication that the solutions will become invalid for layer widths less than the full waveguide.

Although difficult to analyze quantitatively, the significance of $\tilde{A}$ can be explained in terms of the constant velocity versus the two-layer solution. From Eq. (21), we know the true and background solutions in a constant velocity waveguide are constructed from an identical set of eigenfunctions; only the eigenvalues differ. In the two-layer waveguide, the eigenfunctions of the true solution vary (see Eq. (38)) depending on the receiver location in the waveguide with respect to the layer. The former case has a simple normalization factor of $\sqrt{(2/h)}$, while from Eq. (39) the latter has the expression, A_1. From the modal decomposition of the Born and Rytov approximations (Appendix E), the term $\tilde{A}$ occurs which contains, in addition to the factor $\sqrt{A_1}$, other terms resulting from the projection of the coefficients over a depth 0 to z_1 where the constant velocity eigenfunctions are not orthogonal. Therefore, for the Born and Rytov solutions to be valid representations of the true field, the term $\tilde{A}$ must give the right mode shapes for the two-layer waveguide. This is impossible because $\tilde{A}$ is constant for a given layer depth and there still remains only a single set of eigenfunctions predicting the true behavior over the entire waveguide. As a result, the Born and Rytov solutions are unable to approximate the true solution if the true and guess eigenfunctions differ by more than about 7%.

4. DEPTH-DEPENDENT BACKGROUND TEST CASES

4.1 Introduction

Although a constant background solution provides useful error estimates, it is not viable zeroth order solution in the deep ocean. For this reason, we now turn to the distorted-wave perturbative approximations in which the background profile depends on depth. Several depth-dependent velocity profiles are studied and the results compared to those predicted from the constant velocity analysis. In all cases, the trend of the sound speed profile is assumed to be known exactly; we look at the behavior of the DWB and DWR solutions when a perturbation is placed upon the background solution. Unlike the previous chapter, the results in this chapter cannot be derived explicitly even for a single mode. The reason is that the eigenfunctions are known only numerically. The DWB and DWR representations of the total field are obtained from Eqs. (7) and (10), respectively.

The background profile in the first two examples is the weakly refractive NORDA 2A test case (NORDA Parabolic Workshop 1984). Two different size perturbations (referred to as test cases 4 and 5) are placed on this profile and we study the ability of the DW approximations to construct the true solution.

In the second set of examples, the profile is strongly refractive. Two different test cases (referred to as test cases 6 and 7) are presented. The perturbation is the same is both cases but the source position and, therefore, the illumination in the waveguide is varied.

4.2 NORDA 2A Examples

The parameters used in test case 4 are given in Table 4.

Table 4. Input Parameters: Test Case 4

INPUT PARAMETERS: TEST CASE 4		
Range		1.-50. km
Source Depth		500. m
Receiver Depth		500. m
Source Frequency		25. Hz
	Depth (m)	Sound Speed (m/s)
True profile	0.	1500.0
	300.	1506.0
	400.	1507.5
	500.	1510.0
	1000.	1520.0
	1500.	1563.0
Guess profile	0.	1500.0
	1000.	1520.0
	1500.	1563.0
Maximum Perturbation		0.5 m/s
Perturbation Width		200.0 m

Table 5. Input Parameters: Test Case 5

INPUT PARAMETERS: TEST CASE 5		
Range		1.-50. km
Source Depth		500. m
Receiver Depth		500. m
Source Frequency		25. Hz
	Depth (m)	Sound Speed (m/s)
True profile	0.	1500.
	300.	1506.
	400.	1507.
	500.	1510.
	1000.	1520.
	1500.	1563.
Guess profile	0.	1500.
	1000.	1520.
	1500.	1563.
Maximum Perturbation		1. m/s
Perturbation Width		200. m

This is exactly the behavior predicted from the two-layer case in section 3.5. As the change in the true and background mode functions increases, the ability of the DWB and DWR to construct the true solution decreases.

We now turn to some deep ocean examples in which the sound energy propagates mainly through refraction.

4.3 SOFAR Channel Examples

As discussed in Chapter 1, the velocity structure of the SOFAR channel is characterized by a sound speed minimum (known as the channel axis) at about 1 km with the sound speed increasing both above and below the axis. In this section, we study the behavior of the DWB and DWR solutions when the perturbations are placed about a bilinear background sound speed profile. In particular, we investigate the effect of varying the source position with respect to the channel axis.

the perturbative solutions are expected to yield accurate results.

The DWB and DWR transmission loss curves are illustrated in Figures 55 and 56. The vertical scales on both plots have been expanded to include the spike occurring near 29 km. The DWB and DWR solutions are nearly identical as predicted by the small $|P_s/P_o|$ ratios. Both solutions match the true solution in the regions of high intensity, but fail to give the correct values in the shadow zone and in fact exhibit a greater error than the guess near the deep null. A plot of the relative errors (Figure 57) in the two solutions substantiates this conclusion. Although qualitative predictions suggest that both solutions are within their range of validity, this test case indicates that the DWB and DWR are invalid over broad regions of low intensity as well as at the isolated nulls in the field.

In the last example, the parameters are the same as in test case 6 except the source and receiver are placed on the channel axis at 1 km. The true and guess transmission loss plots are illustrated in Figure 58. The shadow zone has disappeared as expected and the background solution nearly overlays the true.

As illustrated in Figure 59, the DWB and DWR scattered to incident field ratios are nearly identical. A closeup of the plots in Figure 60 demonstrates the ratio of the trends to be less than 1/4. Although the spike at approximately 42 km indicates the possibility of a local error, the DWB and DWR solutions are predicted to give an accurate representation of the true transmission loss. This is confirmed by the transmission loss curves in Figures 61 and 62, and the relative errors in Figure 63.

The results of this chapter verify that the behavior of the DWB and DWR solutions can be qualitatively predicted from the quantitative single mode results of chapter 3. If the eigenfunctions do not change by more than approximately 7% and the receiver is well-illuminated, the perturbative solutions will give an accurate representation of the true field in the ocean waveguide to a range of 50 km.

$$P_s(k_o,r,0,z,z_o) = \int_{z_1}^{z_2} B(k_o,r,z,z_o,z')\, e^{i\theta(k_o,r,z,z_o,z')}\, n_1(z')\, dz' \,, \tag{53}$$

where z_1 and z_2 define the limits of the perturbation in depth. The amplitude of the modal sum is defined as B, and the phase as θ. $Be^{i\theta}$ is defined as the transformation kernel relating the scattered field to the profile perturbation.

To construct the transform pair

$$P_s(k_o) \overset{FT}{<=>} n_1(\theta(z'))\,, \tag{54}$$

we generate the scattered data as a function of wavenumber using either DWB or DWR approximations. We then assume that the amplitude wavenumber dependence is known and can be absorbed into the scattered data and replace $B(k_o,r,z,z_o,z')$ with its wavenumber independent equivalent, $\tilde{B}(r,z,z_o,z')$; the modified scattered field is written as $\tilde{P}_s$. Next, we multiply both sides of Eq. (53) by the phase function, $e^{-i\theta(k_o,r,z,z_o,\bar{z}')}$, and integrate over wavenumber to obtain

$$\int_{-\infty}^{\infty} P_s(k_o,\tilde{r},0,z,z_o)\, e^{-i\theta(k_o,r,z,z_o,\bar{z}')}\, dk_o$$

$$= \int_{z_1}^{z_2} n_1(z')\tilde{B}(r,z,z_o,z') \int_{-\infty}^{\infty} e^{i\theta(k_o,r,z,z_o,z') - i\theta(k_o,r,z,z_o,\bar{z}')}\, dk_o\, dz' \,. \tag{55}$$

Assuming that the phase, θ, depends linearly on wavenumber, $\theta = k_o\tilde{\theta}$ where $\tilde{\theta}$ is independent of k_o (or if not a transformation has been made to account for the dependence), and the phase is monotonic in z', then the k_o-space integral is identically equal to a delta function. The argument of the δ-function is the difference of our k_o-independent phase terms, $\tilde{\theta}(z')$ and $\tilde{\theta}(\bar{z}')$. Because the delta function is in terms of the phase instead of depth, we make a transformation obtaining the integrand as a function of the phase. As a result, the transform variables are k_o and $\tilde{\theta}(z')$. Therefore, we write Eq. (55) as

$$\int_{-\infty}^{\infty} \tilde{P}_s(k_o)\, e^{-ik_o\tilde{\theta}(\bar{z}')}\, dk_o = \int_{\tilde{\theta}z_1}^{\tilde{\theta}z_2} \frac{n_1(\tilde{\theta}(z'))\tilde{B}(\tilde{\theta}(z'))\, 2\pi\delta\left[\tilde{\theta}(z') - \tilde{\bar{\theta}}(\bar{z}')\right]}{|\, d\tilde{\theta}/dz'\,|_{z=\bar{z}'}}\, d\tilde{\theta}\,, \tag{56}$$

where $d\tilde{\theta}/dz'$ is the Jacobian of the transformation. For simplicity, we have excluded the parameter dependence in the expression; we retain only the transform variables $\tilde{\theta}(z')$ and k_o explicitly. Evaluation of the phase integral gives

$$n_1(\tilde{\theta}(z')) = \frac{|\, d\tilde{\theta}/dz'\,|_{z=\bar{z}'}}{2\pi\tilde{B}(\tilde{\theta}(z'))} \int_{-\infty}^{\infty} \tilde{P}_s(k_o)\, e^{-ik_o\tilde{\theta}(\bar{z}')}\, dk_o \,. \tag{57}$$

instance, at the deep turning points of the amplitude, the phase derivative is zero; i.e. the propagation is horizontal. Many other zero crossings are evident in the figure and each corresponds to $k_z = 0$.

Recalling that the phase needs to be monotonic for a valid inverse, we see that at least globally this criterion cannot be met. However, if we can find a region where the phase is locally monotonic, and the rest of the inversion criteria are met, then we can attempt a perturbation reconstruction over a limited range in depth.

The next step is to check the frequency dependence of the amplitude and phase derivative or equivalently, the phase, at a fixed range (the phase is constructed from the phase derivative to avoid phase unwrapping). The amplitude was found to have a $1/k_o$ approximate dependence and so are multiplied by k_o. The phase derivative, on the other hand goes approximately like k_o, and accordingly, is divided by k_o. The resultant amplitude and phase derivative curves are illustrated in Figures 67 and 68, respectively, for 10 frequency values ranging from 5 to 50 Hz. Although the curves in each plot are of the same order of magnitude, they are not identical. Therefore, only frequency-averaged versions of these functions are available for use in the inversion algorithm. In addition, because the phase is numerically constructed from its derivative, the spikes in the latter must be selectively removed using a local mean amplitude comparison in order for the algorithm to be stable. We also note that the zero crossings in Figure 68 occur at different depths for different frequencies; therefore, for this profile, the phase monotinicity is a function of frequency. The averaged (over depth and frequency) curves for the amplitude and phase derivative are illustrated in Figures 69 and 70, respectively. Note that it is these averaged functions that will be used in an inversion.

Earlier in the discussion, we postulated that a reconstruction could be attempted over a compact region in depth if the phase were locally monotonic. However, we first need to consider how band-limiting, in particular the absence of zero frequency, affects the recovery of a given perturbation. Also of importance in the reconstruction process is the effect of using numerically constructed averaged quantities. For these reasons, we next investigate the effects of phase averaging and band-limiting on the Fourier reconstruction of two different perturbations.

We first look at our ability to reconstruct a simple triangular perturbation (see Figure 71, the true perturbation has a maximum value of 1 at 100 m). The perturbation is centered at 100 m and its extent is 200 meters. The entire region over which the inversion is performed is assumed to be 700 meters. Because the perturbation is a real positive function, we know from Fourier analysis that zero frequency is required to fully reconstruct the amplitude of the perturbation. However, very low frequencies are unavailable in an actual inversion, and so first we illustrate the effect that systematically removing the lowest frequency values has on the perturbation recovery. If the sampling interval is taken to be .684 m (1024 samples), then the sampling interval in frequency (where c_o is 1500 m/s) is $\sim 1.0\, s^{-1}$. If we generate the Fourier transform of the triangular function, zero the low frequency components of the transform one sample at a time, and then inverse transform, we obtain the curves in

neighborhood (of unknown extent) about the stationary phase point in which the inversion formulation is invalid.

Although we are unable to recover a perturbation using this inversion technique, we nonetheless investigate the behavior of the Born kernel for the deep ocean profiles (examples 6 and 7, chapter 4) in order to gain additional insight. Illustrated in Figures 75, 76 and 77 are the transmission loss of the field and the amplitude and phase derivative of the Born kernel, respectively, constructed using the parameters of test case 6. Because this is a strongly refractive profile, the structure in the three figures is sharply defined. The energy is almost purely refractive. The amplitude and phase derivative curves for 10 frequencies (5 to 50 Hz) at a range of 30 km are illustrated in Figures 78 and 79 with their respective averages in Figures 80 and 81. As compared to the Figures 67 and 68, these curves are nearly identical, except at the localized spikes and low frequencies. In this case, the stationary points consistently occur within a small region at a depth of 2 km. However, at a range of 30 km and a receiver depth of 500 m, we are in a shadow zone. From the modeling results of chapter 4, we recall that the DWB and DWR solutions were unable to give a valid approximation to the true solution. Unfortunately, if we move farther out in range the amplitude and phase derivative behavior again varies with wavenumber. Therefore, although the DWB kernel is stable (in the sense that the Fourier inversion is valid) over the upper region of the waveguide, the lack of field structure in this region makes a perturbation reconstruction impossible.

In the last example, we investigate the DWB kernel when the waveguide is strongly refractive and well-illuminated; test case 7. The transmission loss and the amplitude and phase derivative of the DWB kernel are illustrated in Figures 82, 83 and 84. Although the structure is regular as compared to the NORDA 2A test case, we see from the phase derivative that there are many zero crossings over the depth of the waveguide. As illustrated by the amplitude and phase derivative curves versus wavenumber, (Figures 85 and 86) and their averages (Figures 87 and 88), the behavior of the DWB kernel varies with wavenumber. In Figure 88, we observe two stationary points and, in addition, a higher order stationary point in the vicinity of the source. Therefore, for this source geometry, we have a well-illuminated waveguide, but the points of stationarity render the inversion algorithm invalid.

5.4 Summary of the Inverse Problem

The refractive nature of propagation in the ocean waveguide makes a wide-band Fourier-like inversion for a single source-receiver, invalid. In regions where the waveguide is well-illuminated, there are multiple turning points (where the Jacobian goes through a zero) and the transformation relating the scattered field data and a depth-dependent perturbation is no longer 1 to 1. If the energy is trapped within a narrow beam due to source placement, then the regions in which the phase is monotonic coincide with shadow zones in the waveguide; in these regions, the DWB and DWR approximations yield inaccurate results.

CONCLUSIONS

The Born and Rytov approximations to the transmitted field, in which the direction of propagation is in range and the perturbation is in depth, behave in much the same way as the solutions in a layered earth. In a constant velocity earth, the depth-dependent wave functions are have the same functional form for the true and background fields; therefore, the errors are simple to derive and interpret. In fact, the Born and Rytov mode coefficients can be projected from the solutions to give the exact error in the approximations for a single mode. As verified by the constant velocity example, the validity of the Born solution depends on the size and extent of the perturbation; the scattered field must be less than the incident field in order to obtain an accurate approximation. The Rytov solution, however, is insensitive to the distance traveled in the perturbed medium. The accuracy of the approximation instead depends on the gradient of the ratio of the scattered to incident fields.

The behavior of the solutions in a layered waveguide is a bit more difficult to quantize. The true and background eigenfunctions no longer have the same form and the projected mode coefficients are difficult to interpret. However, through numerical examples, we found the mode functions can differ by up to 7%; at this limit, accurate representations of the true field will be obtained for ranges less than 25 km.

The information obtained from the two-layer test cases is used to estimate the magnitude and extent of perturbations permissible when the background sound speed depends on depth. The accuracy of the approximations depends both on the profile and the source-receiver configuration. If the receiver is in a shadow zone, the correct field structure is not well approximated. In general, however, if the receiver is well-illuminated, the behavior of the DWB and DWR fields (for a depth-dependent perturbation) follows that predicted in the two layer case. Accordingly, the extent to which the background profile can deviate from the true profile in an inhomogeneous environment can be estimated; therefore indicating the size and extent of profile perturbations which can be recovered in an inverse problem using either the DWB and DWR approximations to the scattered field.

The inverse algorithm was formulated as a Fourier inversion assuming the phase of the DWB kernel and the wavenumber to be Fourier transform variables. Because the kernel is written as a modal sum, no explicit expressions for the amplitude and phase were available; therefore, the analysis was completely numerical. Although the gross wavenumber dependence was determined and numerically removed from the amplitude and phase, the functions were necessarily averaged over wavenumber to smooth any local dependence. When the averaging process is applied to the phase, the information content of the Fourier constituents is distorted; in effect the phase function is no longer contins the correct information on the perturbation. In addition, the phase was not monotonic in regions in which the waveguide was well-illuminated and so in these regions the inverse algorithm was no longer valid. As a result of these limitations (plus band-limiting), no perturbations were recovered using either the DWB or DWR

ACKNOWLEDGMENTS

I would like to thank the Office of Naval Research, Ocean Acoustics Division and the Naval Research Laboratory in Washington, DC for partially supporting this research. I also thank Brian Sumner for writing the plot package used in generating the graphics in this thesis.

Special thanks goes to the Center for Wave Phenomena, especially my advisor, John DeSanto, for providing support and encouragement throughout both my Master's and Ph.D. programs at the School of Mines.

Last of all, I thank my parents who always believed in me and my husband, Russell, for enduring my manic-depressive pre-Ph.D. personality. I love you, Russell.

Leontovich, M. A. and V. A. Fock, 1946, Zh. Eksp. Teor. Fiz. **16**, 557-573, English transl., 1946, J. Phys. USSR **10, 13-24.**

Kamel, A., and L. B. Felsen, 1982, On the ray equivalent of a group of modes, **71**, 1445-1452.

Keller, J. B., 1969, Accuracy and validity of the Born and Rytov approximations, J. Opt. Soc. Am., **59**, 1003-1004.

Mueller, R. K., M. Kaveh and G. Wade, 1979, Reconstructive Tomography and Applications to Ultrasonics, Proc. of the IEEE, **67**, No. 4, 567-587.

Munk, W. H. and C. Wunsch, 1979, Ocean acoustic tomography: a scheme for large scale monitoring, Deep Sea Res., **26**, 123-161.

Munk, W. H. and C. Wunsch, 1982, Up-down resolution in ocean acoustic tomography, Deep Sea Res., **29**, 1415-1436.

Munk, W. H. and C. Wunsch, 1983, Ocean acoustic tomography: rays and modes for large scale monitoring, Reviews of Geophys. and Space Phys., **21**, No. 4, 777-793.

Officer, C. B., 1966, Introduction to the Theory of Sound Transmission, McGraw-Hill, New York.

Pedersen, M. A., and D. F. Gorden, 1972, Normal-mode and ray theory applied to underwater acoustic conditions of extreme downward refraction, J. Acoust. Soc. Am. **51**, 323-368.

Porter, M., 1988, The KRAKEN Normal Mode Program (DRAFT), personal communication.

Raz, S., 1981, Direct reconstruction of velocity and density profiles from scattered field data, Geophys. **46**, No. 6, 832-836.

Rytov, S. M., 1937, Diffraction of light by ultrasonic waves, Izv., Akad. Nauk SSSR Ser. Fiz. **2**, 223-259. (In Russian)

Slaney, M., A. C. Kak and L. E. Larsen, 1984, Limitations of imaging with first-order diffraction tomography, IEEE Trans. on Microwave Theory and Techniques, **MTT-32**, No. 8, 860-873.

Spiesberger, J., R. Spindel and K. Metzger, 1980, Stability and identification of ocean acoustic multipaths, J. Acoust. Soc. Amer., **67**, 2011-2017.

Spiesberger, J., P. F. Worcester, 1983, Perturbations in travel time and ray geometry due to mesoscale disturbances: A comparison of exact and approximate calculations, J. Acoust. Soc. Amer., **74**, 219-225.

Tolstoy, I., and C. S. Clay, 1966, Ocean Acoustics, McGraw-Hill, New York.

Tolstoy, I., and C. S. Clay, 1987, Ocean Acoustics: Theory and Experiment in Underwater Sound, American Institute of Physics, Inc., New York.

Taner, M. T., F. Koehler, and R. E. Sheriff, 1979, Complex seismic trace analysis, Geophys., **44**, No. 6, 1041-1963.

APPENDIX A:

Derivation of the Normal Mode Representation of the Field

The integral representation of the sound field of a point source contains the normal modes (discrete spectrum) as well as the continuous spectrum. The discrete spectrum constitutes the main contribution since the normal modes are only weakly attenuated, whereas the continuous spectrum rapidly attenuates with range. If we are in the far field of the source, then, to a good approximation, only the normal modes contribute significantly to the pressure field. In this appendix, the modal field representation is derived for a specific set of boundary conditions.

We begin with the inhomogeneous Helmholtz equation

$$\left[\nabla^2 + k_o^2 n_o^2(z)\right] P_o(k_o,r,r_o,z,z_o) = -\frac{\delta(r-r_o)\delta(z-z_o)}{2\pi r} \qquad \text{(A.1)}$$

in cylindrical coordinates for an arbitrary source point, (r_o,z_o). The boundary conditions are chosen to be

$$P_o(k_o,r,r_o,z,z_o) \mid_{z=o} = 0, \qquad \frac{\partial}{\partial z} P_o(k_o,r,r_o,z,z_o) \mid_{z=h} = 0$$

where h is the width of the ocean waveguide.

The homogeneous form of Eq. (A.1) is separable and the pressure field of a wave outgoing from a source located at r_o can be written as

$$P_o(k_o,r,r_o,z,z_o) = C(z_o,\xi) H_o^{(2)}(\xi r) J_o(\xi r_o) \psi(z,\xi) \qquad r > r_o \qquad \text{(A.2.a)}$$

$$P_o(k_o,r,r_o,z,z_o) = C(z_o,\xi) H_o^{(2)}(\xi r_o) J_o(\xi r) \psi(z,\xi) \qquad r < r_o \qquad \text{(A.2.b)}$$

The time dependence was chosen to be $\exp(i\omega t)$. In the first equation $H_o^{(2)}(\xi r)$ constitutes a right-traveling wave. The second equation contains both right and left-traveling components, but at large r the right-going wave is only seen in its effect due to the coupling with Eq. (A.2.a). The range-dependent solution, which I will call $G(\xi r \mid \xi r_o)$ for simplicity, is derived in Appendix B. The depth dependent solution, $\psi(z,\xi)$, satisfies

$$\left[\frac{d^2}{dz^2} + (k_o^2 n_o^2(z) - \xi^2)\right] \psi(z,\xi) = 0 \qquad \text{(A.3)}$$

with boundary conditions

$$\sum_n C(z_o,\xi_n)\psi(z,\xi_n) = \frac{i}{4}\delta(z-z_o)\,. \tag{A.9}$$

Multiplying by $\psi(z,\xi_m)$, integrating over the depth of the waveguide and using orthogonality of the normal modes gives

$$C(z_o,\xi_n) = \frac{i}{4}\frac{\psi(z_o,\xi_n)}{\int_0^h \psi(z,\xi_n)\psi(z,\xi_n)\,dz}\,. \tag{A.10}$$

Normalizing the $\psi's$ in such a way that the integral is equal to 1, $C(z_o,\xi_n)$ is equal to $\frac{i}{4}\psi(z_o,\xi_n)$, and the final solution is written as

$$P_o(k_o,r,r_o,z,z_o) = \frac{i}{4}\sum_n G(\xi_n r \mid \xi_n r_o)\psi(z,\xi_n)\psi(z_o,\xi_n)\,. \tag{A.11}$$

Substituting the $G(\xi_n r \mid \xi_n r_o)$ from Appendix B, the incident field modal solution is

$$P_o(k_o,r,r_o,z,z_o) = \frac{i}{4}\sum_n H_o^{(2)}(\xi_n r)J_o(\xi_n r_o)\psi(z,\xi_n)\psi(z_o,\xi_n) \qquad r>r_o$$

$$P_o(k_o,r,r_o,z,z_o) = \frac{i}{4}\sum_n H_o^{(2)}(\xi_n r_o)J_o(\xi_n r)\psi(z,\xi_n)\psi(z_o,\xi_n) \qquad r<r_o. \tag{A.12}$$

$$-\frac{i}{2\pi}\int_{-\infty}^{\infty}\frac{H_o^{(1)}(k_r r)H_o^{(2)}(k_r r_o)k_r dk_r}{k_r^2-{\xi_n}^2}\,. \tag{B.6}$$

If we now change the integration along the real line into a contour integral by making k_r complex, the evaluation of these integrals is accomplished using the residue theorem. If the time dependence is chosen to be $e^{i\omega t}$, then the form of an outgoing wave is $e^{-ik_r r}$. Using the asymptotic form of the Hankel functions, these integrals can be rewritten as

$$G(\xi_n r\,|\,\xi_n r_o)\sim -\frac{1}{\pi^2}(rr_o)^{-1/2}\int_C\frac{e^{ik_r(r+r_o)}}{k_r^2-{\xi_n}^2}dk_r$$

$$-\frac{1}{\pi^2}(rr_o)^{-1/2}\int_C\frac{e^{ik_r(r-r_o)}}{k_r^2-{\xi_n}^2}dk_r\,. \tag{B.7}$$

The asymptotic forms are used simply to make the pole evaluation more transparent. In the first integral of Eq. (B.7), $r+r_o$ is always greater than 0; therefore, if k_r is positive imaginary, we have convergence in the upper half plane. We have two poles at which to evaluate the integrand. Evaluation at the positive pole results in an incoming wave and so this solution is discarded. Evaluation at the negative pole gives the outgoing wave contribution. Asymptotically, the first integral becomes

$$\frac{i}{\pi\xi_n}(rr_o)^{-1/2}\,e^{-i\xi_n(r\,+\,r_o)}\,, \tag{B.8}$$

and therefore, the solution is

$$\frac{1}{2}H_o^{(2)}(\xi_n r_o)H_o^{(2)}(\xi_n r)\,. \tag{B.9}$$

The phase of the second integral looks like $k_r(r-r_o)$ and must be evaluated depending on whether r is greater than or less than r_o. For $r>r_o$, we have convergence in the upper half plane. Evaluation at $k_r=-\xi_n$ gives the outgoing wave and the solution is

$$\frac{1}{2}H_o^{(1)}(\xi_n r_o)H_o^{(2)}(\xi_n r)\,. \tag{B.10}$$

For $r<r_o$, we have convergence in the lower half plane. Evaluation at the positive pole gives the outgoing wave solution

$$\frac{1}{2}H_o^{(2)}(\xi_n r_o)H_o^{(1)}(\xi_n r)\,. \tag{B.11}$$

Summing Eqs. (B.9) and (B.10) and using Eq. (B.4), we obtain the solution for r greater r_o.

APPENDIX C:

Derivation of the Full DWR Solution

The DWR approximation is derived by first assuming the total field solution can be written as

$$P(k_o,r,r_o,z,z_o) = P_o(k_o,r,r_o,z,z_o)\,e^{\Phi(k_o,r,r_o,z,z_o)}\,, \tag{C.1}$$

where $P_o(k_o,r,r_o,z,z_o)$ is a known incident field and $\Phi(k_o,r,r_o,z,z_o)$ is a complex phase function. Substituting Eq. (C.1) into the Helmholtz equation, (1), and performing the differentiation gives

$$\left[\nabla^2 + \left(\nabla^2\Phi + (\nabla\Phi)^2 + k_o^2 n^2(r,z)\right)\right] P_o + 2\,\nabla P_o\cdot\nabla\Phi = -\frac{\delta(r-r_o)\delta(z-z_o)}{2\pi r}\,e^{-\Phi}\,. \tag{C.2}$$

From Chapter 2, we know the incident field satisfies

$$\left[\nabla^2 + k_o^2 n_o^2(z)\right] P_o = -\frac{\delta(r-r_o)\delta(z-z_o)}{2\pi r}\,. \tag{C.3}$$

Therefore, by evaluating $e^{-\Phi}$ at the source (Φ is zero at the source because the scattered field is zero), Eq. (C.2) can be reduced to

$$P_o\,\nabla^2\Phi + 2\,\nabla P_o\cdot\nabla\Phi = -P_o\,(\nabla\Phi)^2 - k_o^2(n^2(r,z) - n_o^2(z))P_o\,. \tag{C.4}$$

We would like to write Eq. (C.4) in the form of a Helmholtz equation and solve for Φ using our Green's function, P_o. Away from the source, we can set

$$P_o\,\nabla^2\Phi + 2\,\nabla P_o\cdot\nabla\Phi = \left[\nabla^2 + k_o^2 n_o^2(z)\right](P_o\Phi) \tag{C.5}$$

so using Eq. (C.5) our differential equation, (C.4), becomes

$$\left[\nabla^2 + k_o^2 n_o^2(z)\right](P_o\Phi) = -P_o\,(\nabla\Phi)^2 - k_o^2(n^2(r,z) - n_o^2(z))P_o\,. \tag{C.6}$$

Therefore, the complex phase function, Φ, is given by the non-linear integral equation

APPENDIX D:

Evaluation of the Range-Dependent Solution

As defined in chapter 2, the range-dependent solution for a point source located at $r_0 = 0$ is given by

$$I(n,m) = H_o^{(2)}(\xi_n r)\int_o^r J_o(\xi_n r')H_o^{(2)}(\xi_m r')r'\,dr' + J_o(\xi_n r)\int_r^\infty H_o^{(2)}(\xi_n r')H_o^{(2)}(\xi_m r')r'\,dr' . \tag{D.1}$$

For clarity in the evaluation, the first integral is defined to be I_1 and the second to be I_2. The integrals are evaluated differently depending on whether $\xi_n = \xi_m$ or $\xi_n \neq \xi_m$.

For $\xi_n \neq \xi_m$, the integrals are evaluated as follows. We know $J_o(\xi_n r)$ and $H_o^{(2)}(\xi_m r)$ satisfy Bessel's equation. Choosing $x(r)$ and $y(r)$ to represent any Bessel functions, we write

$$x'' + \frac{1}{r}x' + \xi_n{}^2 x = 0$$

and

$$y'' + \frac{1}{r}y' + \xi_m{}^2 y = 0.$$

Multiplying the first equation by $r\,y$, the second by $r\,x$, subtracting the two equations and combining terms gives

$$r\left[y\,x'' - x\,y''\right] + x'\,y - y'\,x = (\,\xi_n{}^2 - \xi_m{}^2\,)r\,x\,y$$

or

$$\left[r(x\,y' - y\,x')\right]' = \left[\xi_n{}^2 - \xi_m{}^2\right]r\,x\,y\,.$$

To evaluate the first integral in Eq. (D.1), we set $J_o(\xi_n r) = x$, $H_o^{(2)}(\xi_m r) = y$ and integrate from 0 to r to obtain

$$\int_o^r J_o(\xi_n r')H_o^{(2)}(\xi_m r')r'\,dr' = \frac{\left[r'\,\xi_m J_o(\xi_n r')\,H_1^{(2)}(\xi_n r') - r'\,\xi_n J_1(\xi_n r')H_o^{(2)}(\xi_n r')\right]\Big|_o^r}{\xi_n{}^2 - \xi_m{}^2}. \tag{D.2}$$

The solution of the second integral is obtained in a similar manner. Multiplying the terms by their respective constants, I_1 and I_2 become

integrals become

$$I = \frac{H_o^{(2)}(\xi_n r)}{{\xi_n}^2} \int_o^{\xi_n r} J_o(y) H_o^{(2)}(y) y dy + \frac{J_o(\xi_n r)}{{\xi_n}^2} \int_{\xi_n r}^{\infty} H_o^{(2)}(y) H_o^{(2)}(y) y dy \,. \tag{D.9}$$

Again, we define the first integral as I_1 and the second as I_2 and integrate by parts. To evaluate I_1, we write

$$u = J_o(y) H_o^{(2)}(y) \qquad du = -\left[J_o(y) H_1^{(2)}(y) + J_1(y) H_o^{(2)}(y) \right] dy$$

$$dv = y dy \qquad v = \frac{y^2}{2}$$

to obtain

$$I_1 = \frac{H_o^{(2)}(\xi_n r)}{{\xi_n}^2} \cdot \left[\frac{y^2}{2} J_o(y) H_o^{(2)}(y) \Big|_o^{\xi_n r} - \int_o^{\xi_n r} \frac{y^2}{2} [J_o(y) H_1^{(2)}(y) + J_1(y) H_o^{(2)}(y)] \, dy \right] . \tag{D.10}$$

Evaluating the first term at $\xi_n r$, (the expression is zero at $y = 0$), we obtain

$$\frac{r^2 H_o^{(2)}(\xi_n r)}{2} J_o(\xi_n r) H_o^{(2)}(\xi_n r) \,. \tag{D.11}$$

To evaluate the remaining integral, I_{11}, in Eq. (D.10), we substitute Eqs. (D.5) for $J_o(y)$ and $J_1(y)$ and combine terms. The result is

$$I_{11} = -\frac{H_o^{(2)}(\xi_n r)}{{\xi_n}^2} \cdot \int_o^{\xi_n r} \frac{y^2}{4} \left[2 H_o^{(2)}(y) H_1^{(2)}(y) + H_o^{(1)}(y) H_1^{(2)}(y) + H_1^{(1)}(y) H_o^{(2)}(y) \right] dy \,. \tag{D.12}$$

Defining the first term as I_{111} and using Bessel's Equation

$$y^2 H_o^{(2)}(y) = -y H_o'^{(2)}(y) - y^2 H_o''^{(2)}(y) \tag{D.13}$$

we obtain

$$+ \frac{H_o^{(2)}(\xi_n r) r^2}{4} \left[J_1(\xi_n r) \right]^2 + \frac{H_o^{(2)}(\xi_n r) r^2}{4} \left[Y_1(\xi_n r) \right]^2 \qquad \text{(D.20)}$$

Writing $H_o^{(2)}(\xi_n r) = J_o(\xi_n r) - iY_o(\xi_n r)$ in the second term and recombining terms gives

$$I = - \frac{H_o^{(1)}(\xi_n r) r^2}{4} \left[H_1^{(2)}(\xi_n r) \right]^2 + \frac{H_o^{(2)}(\xi_n r) r^2}{4} \left[H_1^{(1)}(\xi_n r) \left(H_1^{(1)}(\xi_n r) \right)^* \right] \qquad \text{(D.21)}$$

where * denotes complex conjugate. Now, $\left[H_1^{(1)}(\xi_n r) \right]^* = H_1^{(2)}(\xi_n{}^* r)$, so for real eigenvalues

$$I = - \frac{H_o^{(1)}(\xi_n r) r^2}{4} \left[H_1^{(2)}(\xi_n r) \right]^2 + \frac{H_o^{(2)}(\xi_n r) r^2}{4} \left[H_1^{(1)}(\xi_n r) H_1^{(2)}(\xi_n r) \right] \qquad \text{(D.22)}$$

or recognizing the Wronskian

$$H_1^{(1)}(\xi_n r) H_1^{(2)}(\xi_n r) - H_o^{(1)}(\xi_n r) H_1^{(2)}(\xi_n r) = - \frac{4i}{\pi \xi_n r} \qquad \text{(D.23)}$$

we obtain the solution when $\xi_n = \xi_m$ as

$$I = - \frac{ir}{\pi} \frac{H_1^{(2)}(\xi_n r)}{\xi_n} \qquad \text{(D.24)}$$

Therefore, evaluation of the range integral for a depth-dependent profile results in the solutions

$$\frac{2i}{\pi} \frac{H_o^{(2)}(\xi_m r)}{\xi_m{}^2 - \xi_n{}^2} \cdot \qquad \xi_n \neq \xi_m \qquad \text{(D.25.a)}$$

$$- \frac{ir}{\pi} \frac{H_1^{(2)}(\xi_n r)}{\xi_n} \qquad \xi_n = \xi_m \cdot \qquad \text{(D.25.b)}$$

It is interesting to note that Eq. (D.25.b) also follows by applying l'Hopital's rule to Eq. (D.25.a), in which case the result is not confined to real eigenvalues.

the expressions will now be evaluated for a single mode for the test cases discussed in Chapter 3.

The first example is of a constant velocity waveguide in which the perturbation spans the entire waveguide. Eqs. (E.1.b) and (E.2.b) do not contribute because the perturbation is constant. In addition, we are finding solutions for only 1 mode. From Eq. (26), the eigenfunctions are sines; replacing the ψ's with sines (see also Eq. (18.b)) in Eq. (E.1.a) and combining terms, the single mode Born expression becomes

$$\left(\frac{2}{h}\right)^{1/2} \int_o^h P_{11}{}^{(B)}(k_o, r, 0, z, z_o) \sin\lambda_1 z \, dz = \frac{i}{4} H_o^{(2)}(\xi_1 r)$$

$$\cdot \left(\frac{2}{h}\right)^{3/2} \sin\left(\frac{\pi z_o}{2h}\right) \int_o^h \left[\sin\left(\frac{\pi z}{2h}\right) - \frac{irk_o^2 n_1}{2\xi_1} \sin\left(\frac{\pi z}{2h}\right)\right] \sin\left(\frac{\pi z}{2h}\right) dz \qquad \text{(E.3)}$$

where λ_1 has been replaced by $\frac{\pi}{2h}$. Integrating the right hand side yields

$$\left(\frac{2}{h}\right)^{1/2} \int_o^h P_{11}{}^{(B)}(k_o, r, 0, z, z_o) \sin\left(\frac{\pi z}{2h}\right) dz$$

$$= \frac{i}{4} H_o^{(2)}(\xi_1 r) \left(\frac{2}{h}\right)^{1/2} \sin\left(\frac{\pi z_o}{2h}\right) \left[1 - \frac{irk_o^2 n_1}{2\xi_1}\right]. \qquad \text{(E.4)}$$

Dividing through by the range solution, $\frac{i}{4} H_o^{(2)}(\xi_1 r)$, the resulting Born mode coefficient, C_{1B}, in a constant velocity waveguide is given by

$$C_{1B} = \left(\frac{2}{h}\right)^{1/2} \sin\left(\frac{\pi z_o}{2h}\right) \left[1 + \frac{irk_o^2 n_1}{2\xi_1}\right]. \qquad \text{(E.5)}$$

Because the Rytov solution is essentially an exponentiated Born, to avoid the simple analysis, we will simply state the result. The Rytov mode coefficient, C_{1R} is

$$C_{1R} = \left(\frac{2}{h}\right)^{1/2} \sin\left(\frac{\pi z_o}{2h}\right) \exp\left[\frac{irk_o^2 n_1}{2\xi_1}\right]. \qquad \text{(E.6)}$$

The second example for which the first mode coefficient is derived is a two-layer waveguide. The velocity is constant in each layer and the background profile a constant over the entire waveguide. Again, Eqs. (E.1.b) and (E.2.b) are not evaluated because we are interested in single mode analytic solutions.

In this case, the mode functions are not the same for the true and background profiles. The true mode functions are given in Eq. (38) and the background modes are

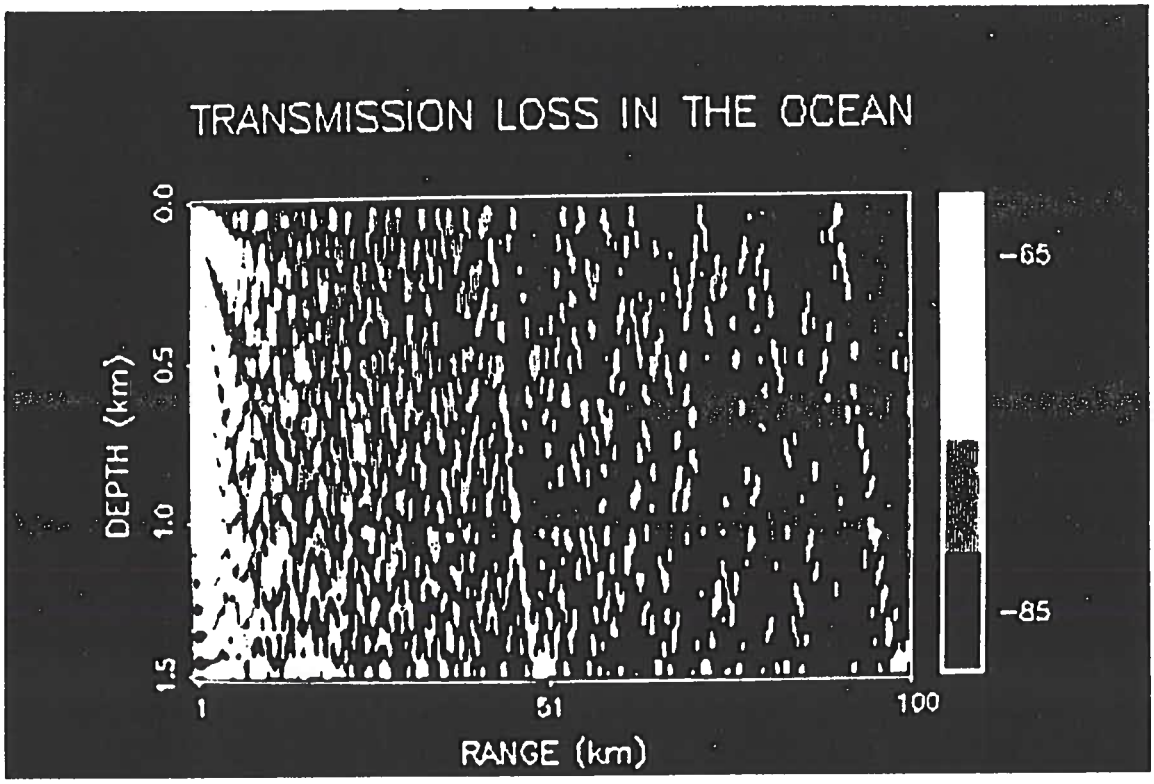

Figure 1. Transmission loss in a constant velocity waveguide. The source frequency is 25 Hz.

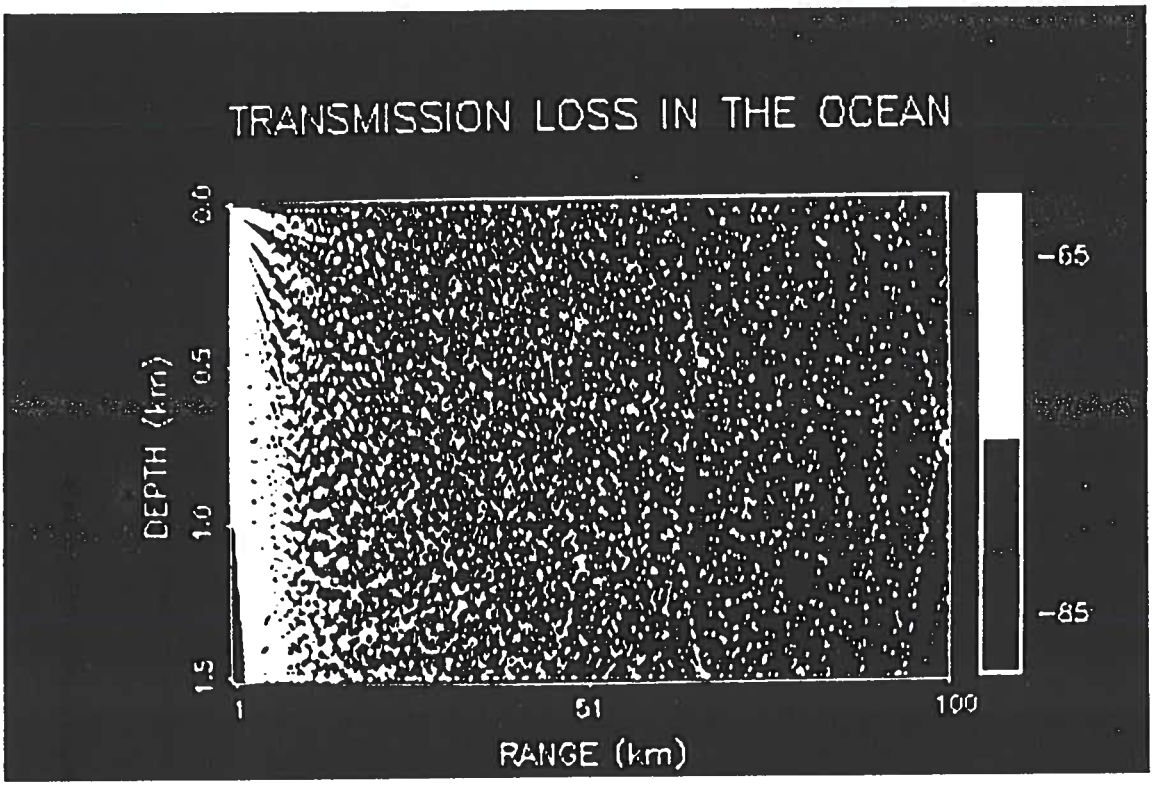

Figure 2. Transmission loss in a constant velocity waveguide. The source frequency is 100 Hz.

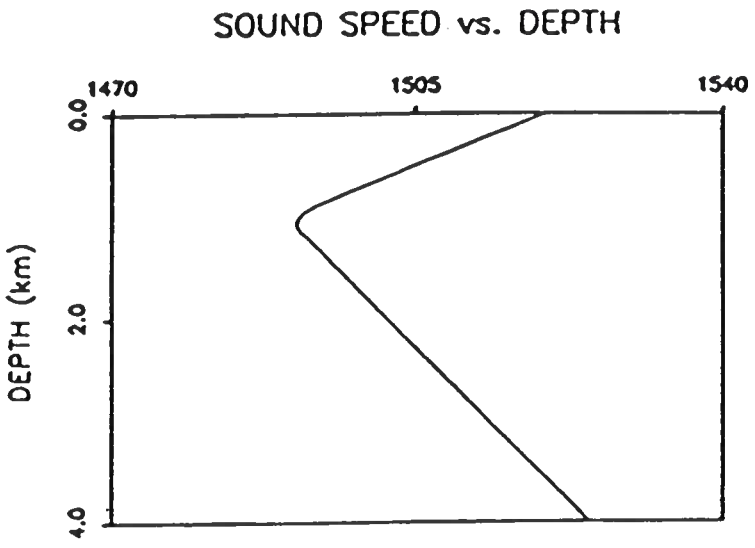

Figure 3. Sound speed profile used in generating the results in Figures 4, 5 and 6. We assume an infinite half-space below the waveguide in which the sound speed is constant and matches the sound speed at the bottom of the waveguide.

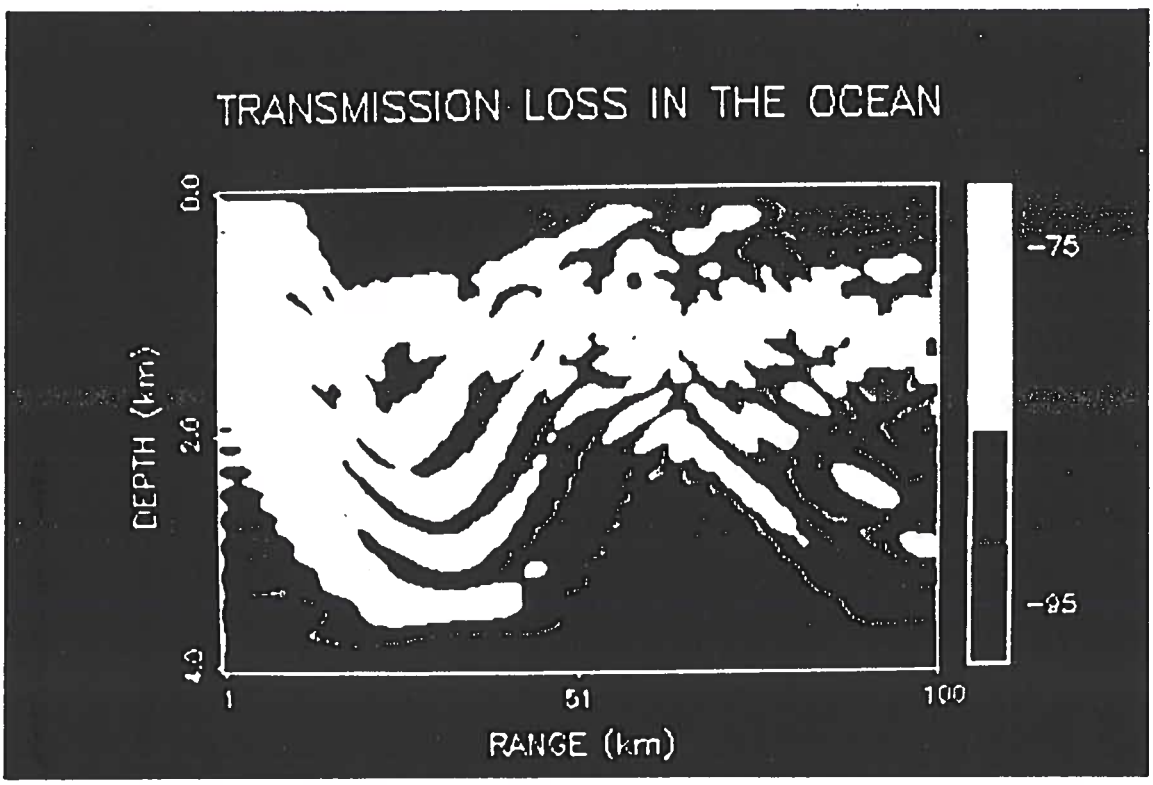

Figure 4. Transmission loss in a refractive medium generated using the profile in Figure 3. The source is placed on the channel axis at 1 km and the source frequency is 25 Hz.

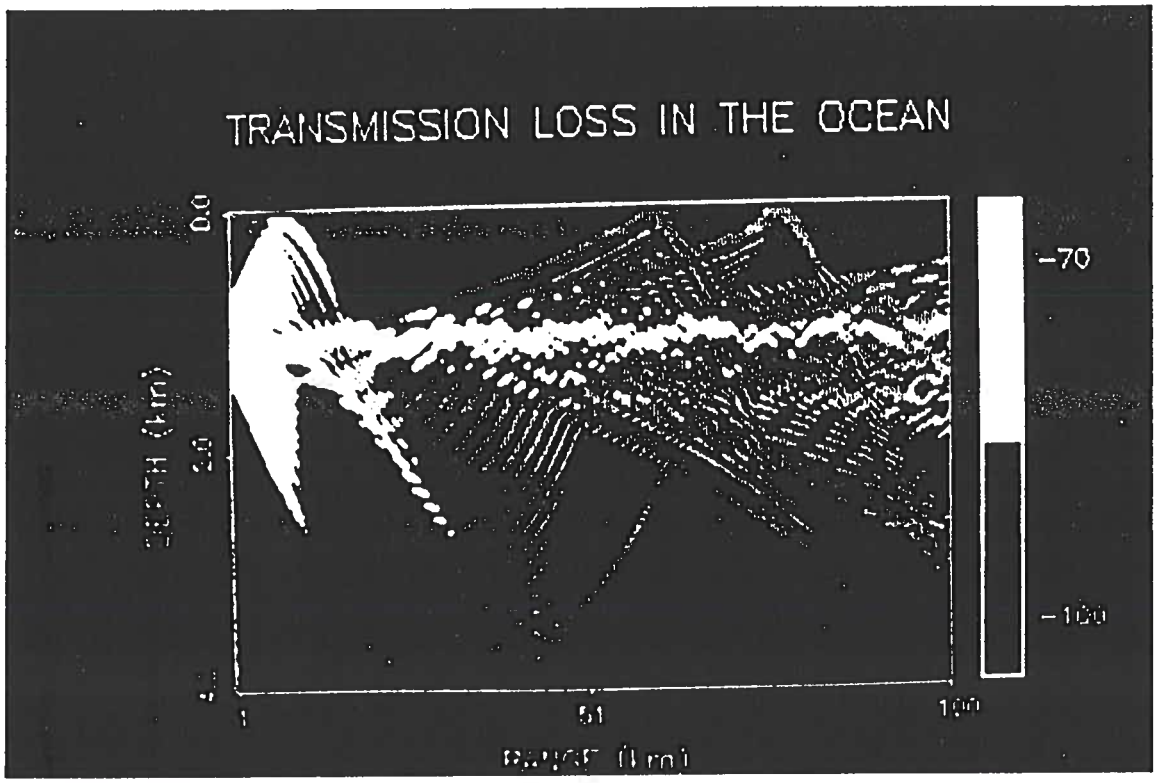

Figure 5. Transmission loss in a refractive medium generated using the profile in Figure 3. The source is placed on the channel axis at 1 km and the source frequency is 100 Hz.

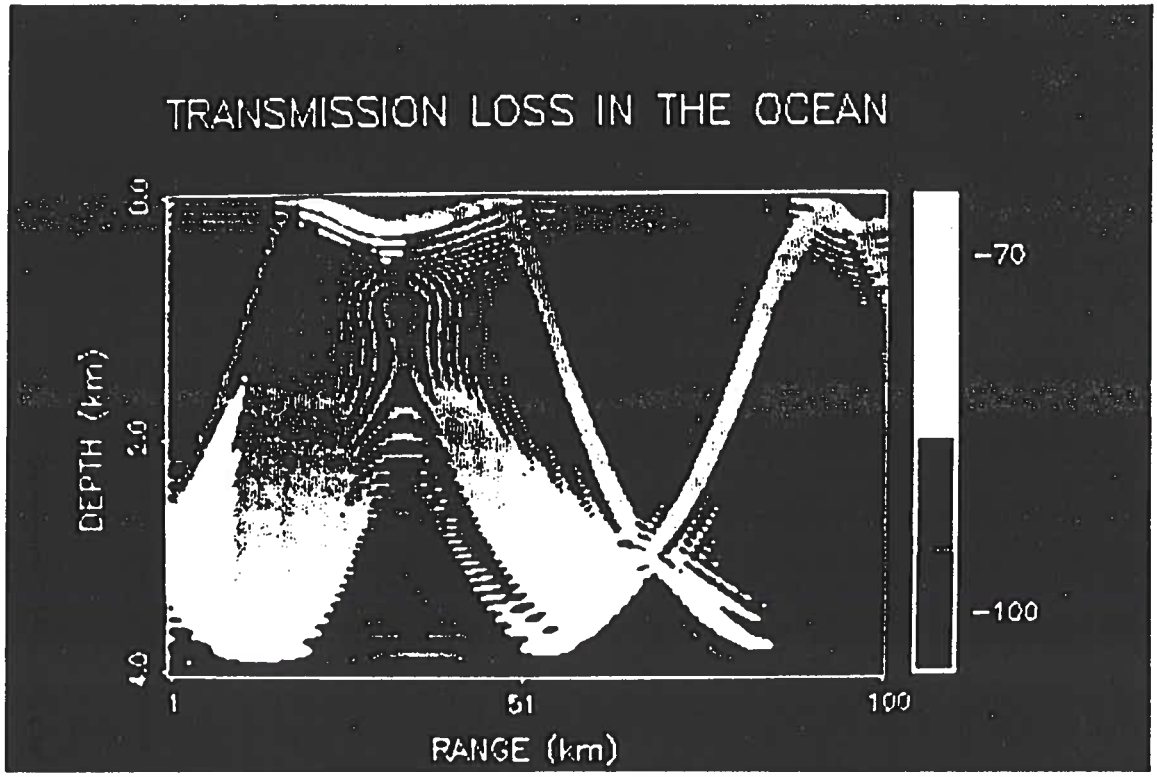

Figure 6. Transmission loss in a refractive medium generated using the profile in Figure 3. The source is placed at a depth of 3 km and the source frequency is 100 Hz.

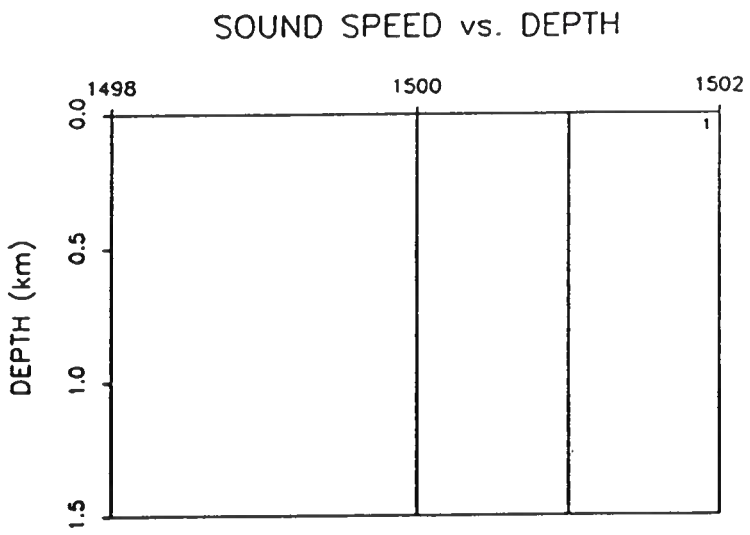

Figure 7. Constant velocity profiles. The true sound speed is 1500 m/s. The guess sound speed in 1501 m/s.

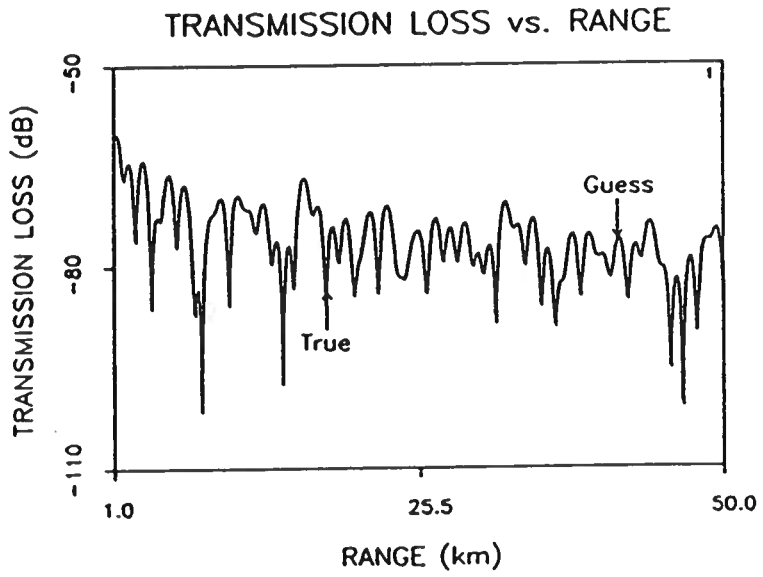

Figure 8. True and background transmission loss curves for test case 1. The curves are generated using the profiles in Figure 7. Because the eigenfunctions have the same functional form, the curves are indistinguishable.

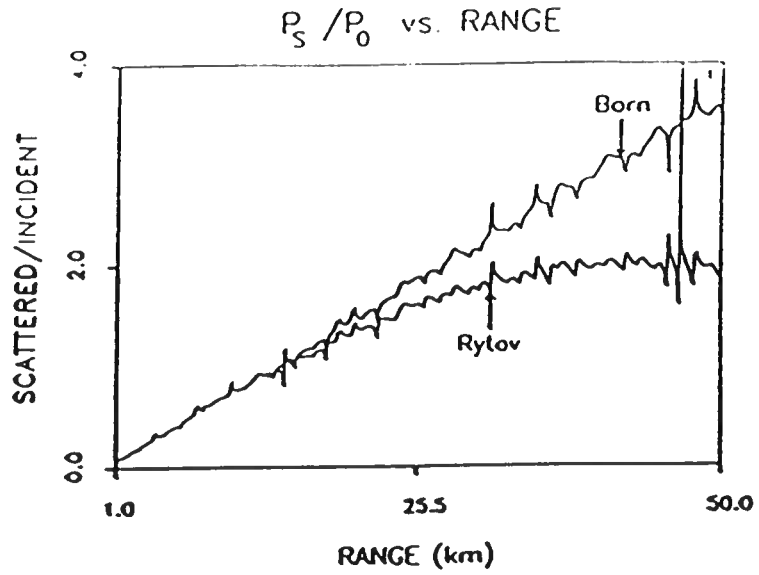

Figure 9. Ratio of the scattered field to the incident field for the Born and Rytov solutions for test case 1. The solutions are generated using the background profile in Figure 7.

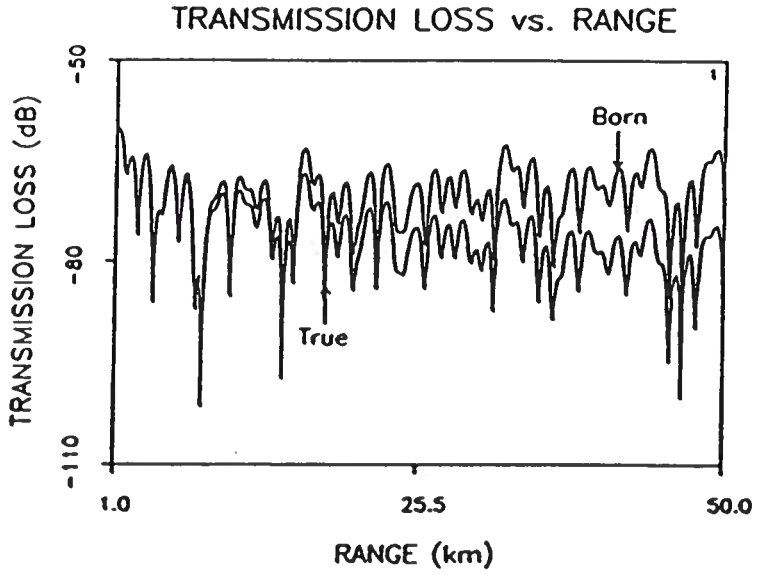

Figure 10. True and Born transmission loss curves for test case 1. The growth of the Born solution with range is clearly seen.

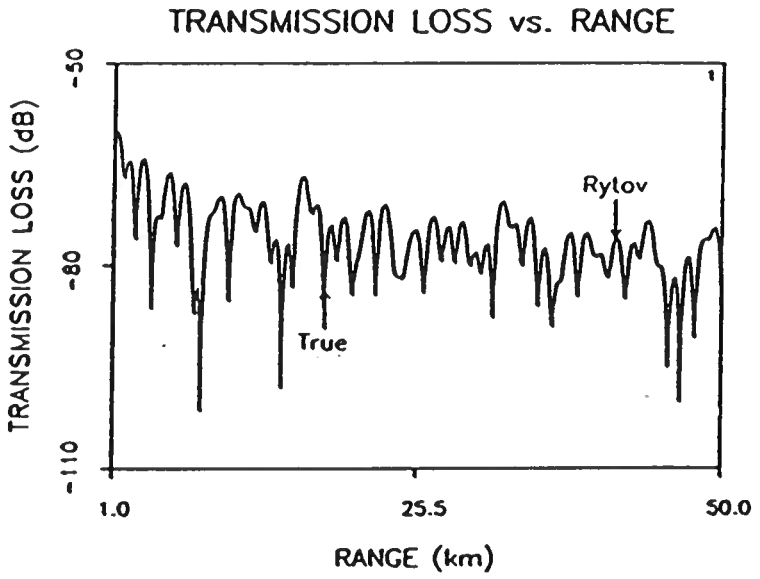

Figure 11. True and Rytov transmission loss curves for test case 1. Unlike the Born solution, the Rytov is unaffected by the extent of the perturbation.

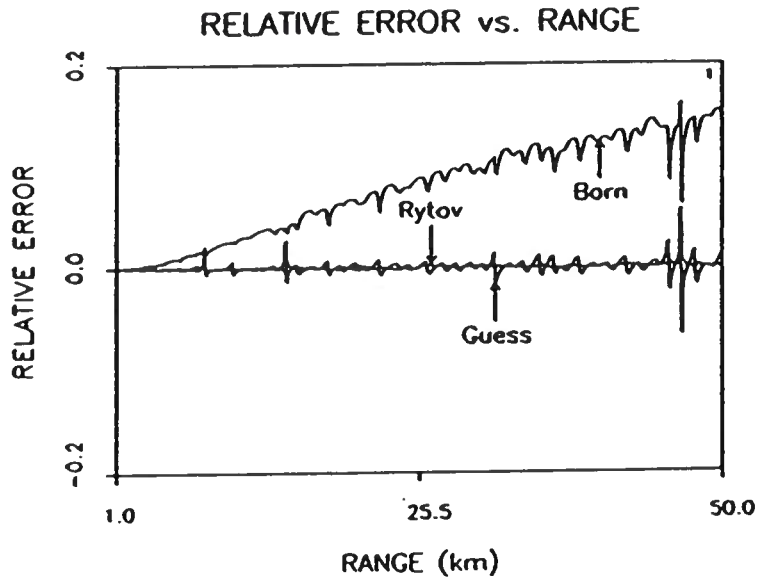

Figure 12. Relative error in the background, Born and Rytov transmission loss curves for test case 1. The Born error is approximately 17% at 50 km. The error in the Rytov solution is approximately zero over the entire range of propagation.

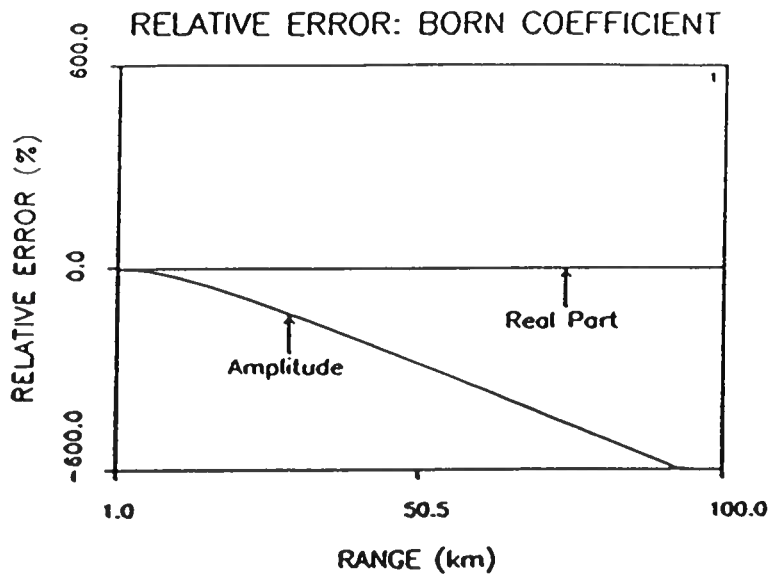

Figure 13. Relative error in the amplitude and real part of the Born mode coefficient for a single mode in test case 1. The real part of the Born coefficient is identically equal to the true coefficient.

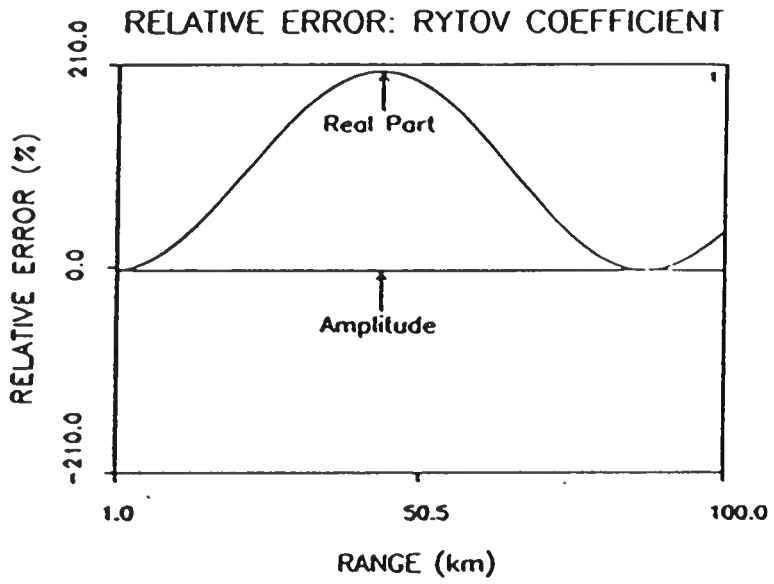

Figure 14. Relative error in the amplitude and real part of the Rytov mode coefficient for a single mode in test case 1. The amplitude of the Rytov coefficient is identically equal to the true coefficient.

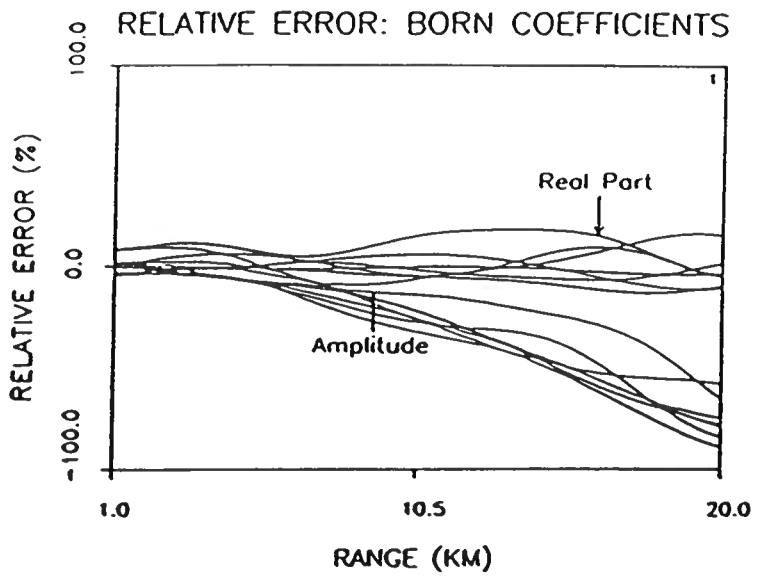

Figure 15. Relative error in the amplitude and real part of the Born mode coefficient for the first seven modes in test case 1.

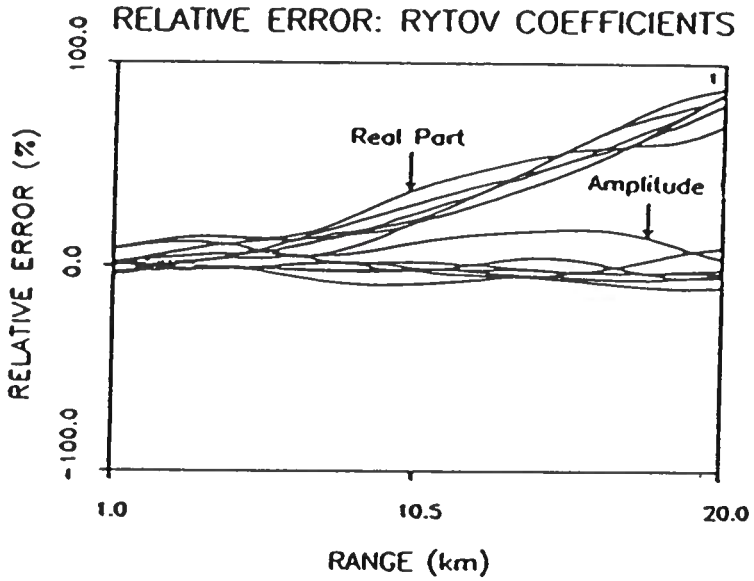

Figure 16. Relative error in the amplitude and real part of the Rytov mode coefficient for the first seven modes in test case 1.

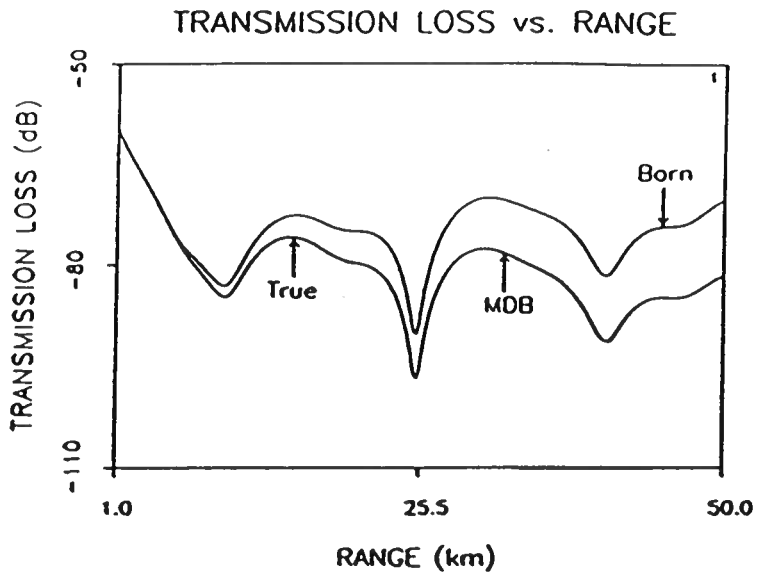

Figure 17. True, Born and the reconstructed Born transmission loss curves generated using the first seven modes in test case 1. The reconstructed Born solution is calculated using the real part of the projected mode coefficients.

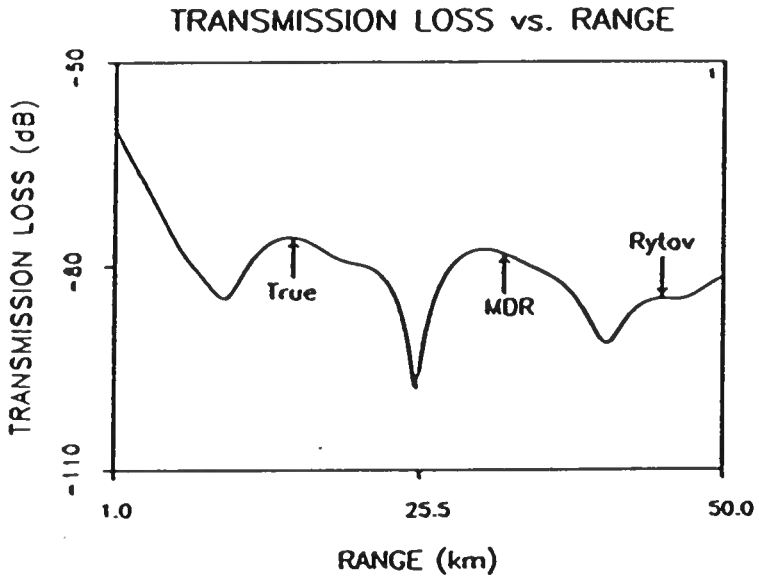

Figure 18. True, Rytov and the reconstructed Rytov transmission loss curves generated using the first seven modes in test case 1. The reconstructed Rytov solution is calculated using the amplitude of the projected mode coefficients.

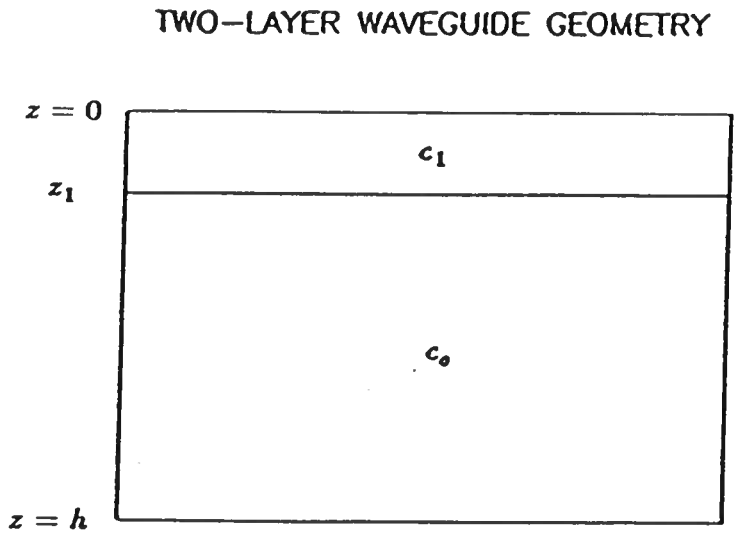

Figure 19. Two-layer geometry used in test cases 2 and 3.

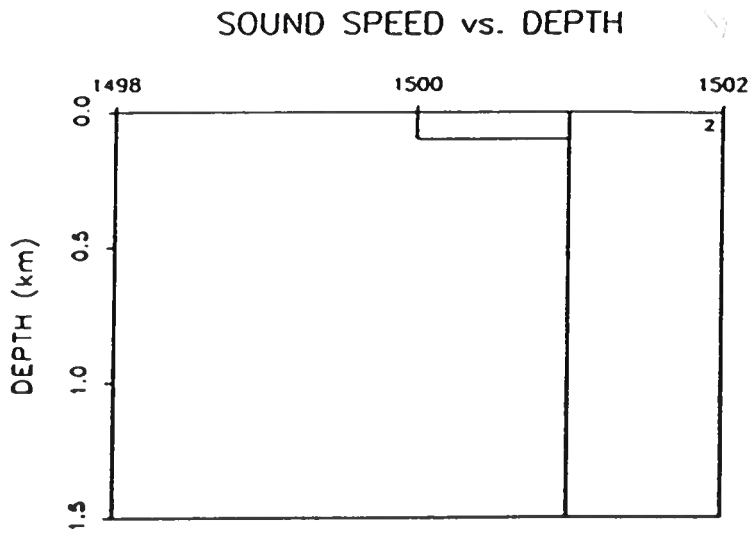

Figure 20. The true and background sound speed profiles used in test case 2. The background profile is constant over the entire waveguide at 1501 m/s. The true profile has a 100 meter layer in which the sound speed is 1500 m/s. Below the layer, the true and background sound speeds are identical.

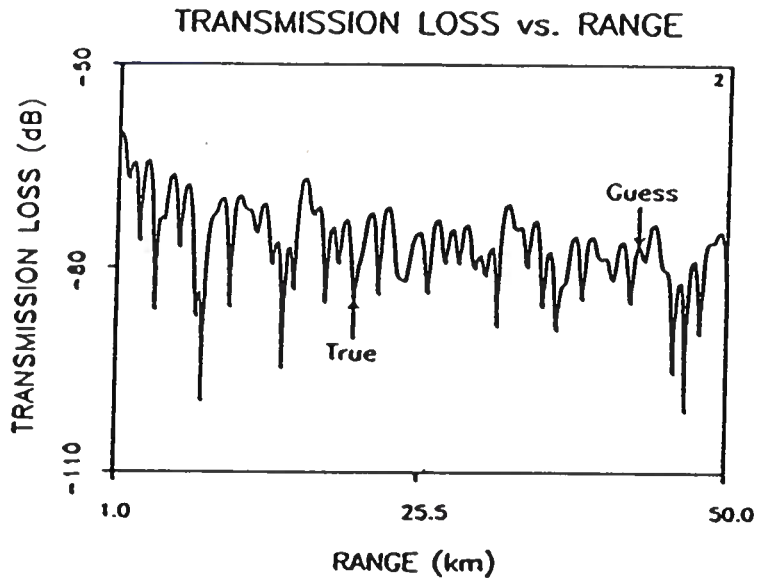

Figure 21. The true and background transmission loss curves for test case 2. Because the perturbation is small (1 m/s) and extends only 100 meters in depth, the two curves are nearly identical.

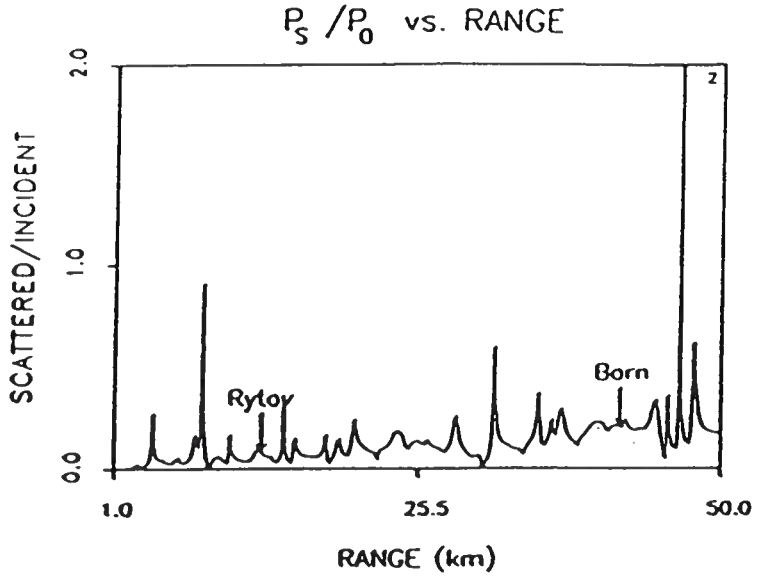

Figure 22. Ratio of the scattered field to the incident field for the Born and Rytov solutions in the two-layer waveguide of test case 2. Because the trend of the ratio is less than 1/4 over the range of propagation, both solutions are expected to yield accurate results.

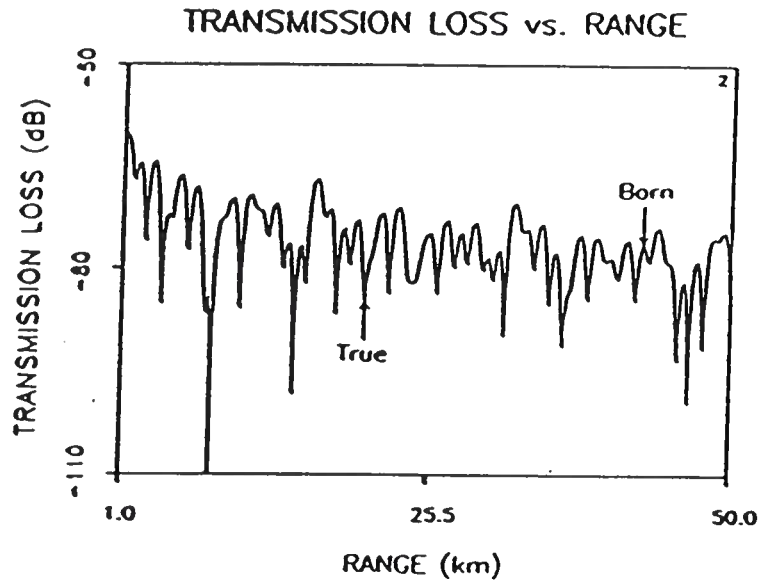

Figure 23. The true and Born transmission loss curves for test case 2. The Born solution matches the true except at the nulls in the field.

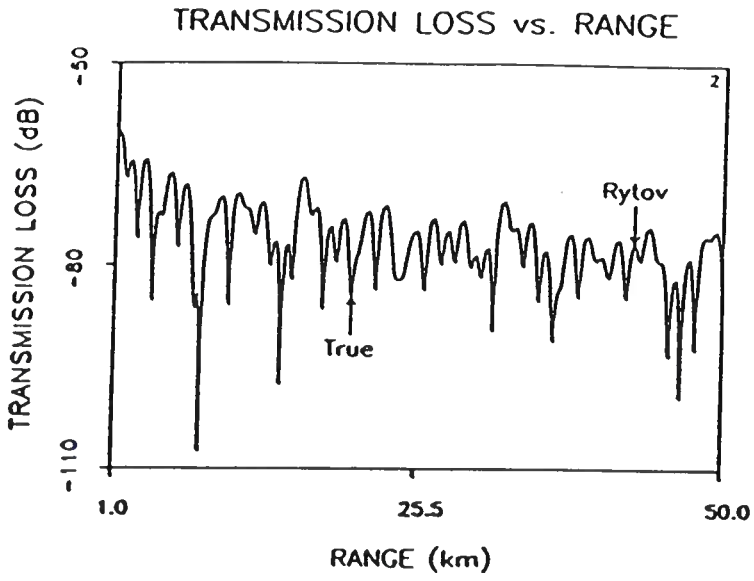

Figure 24. The true and Rytov transmission loss curves for test case 2. The Rytov solution matches the true except at the nulls in the field.

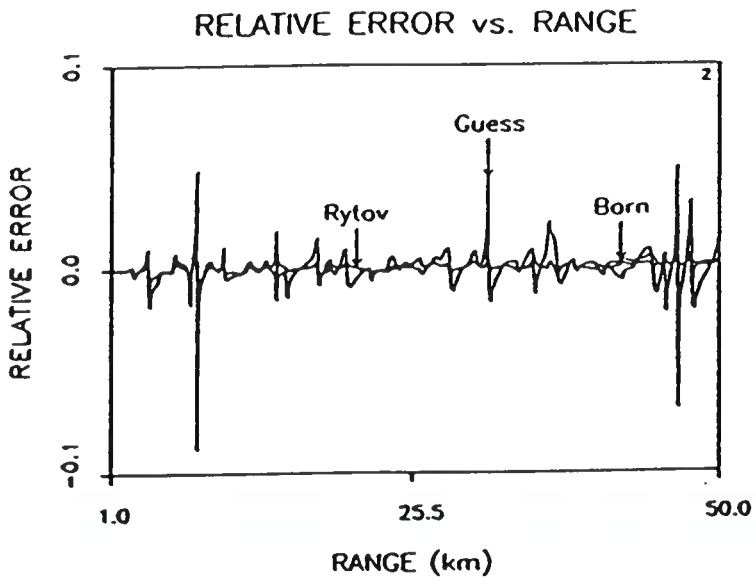

Figure 25. Relative error in the background, Born and Rytov transmission loss curves for test case 2. The error in the the solutions is always less than 10%.

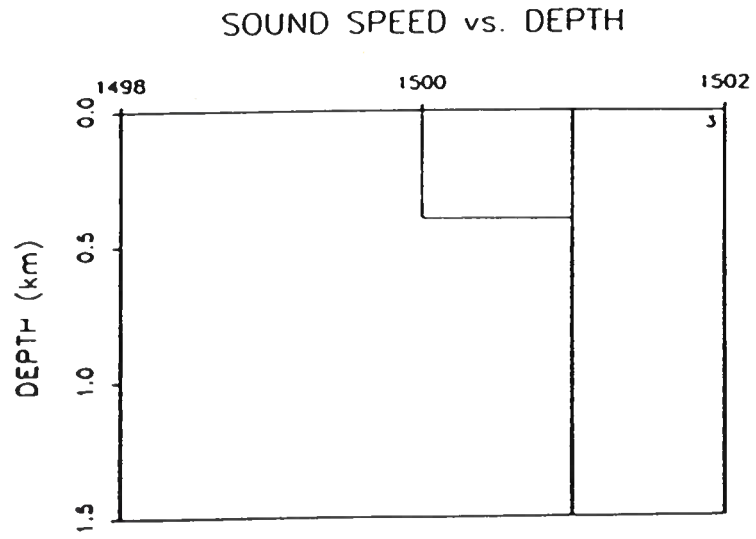

Figure 26. The true and background sound speed profiles used in test case 3. The background profile is constant over the entire waveguide at 1501 m/s. The true profile has a 400 meter layer in which the sound speed is 1500 m/s. Below the layer, the true and background sound speeds are identical.

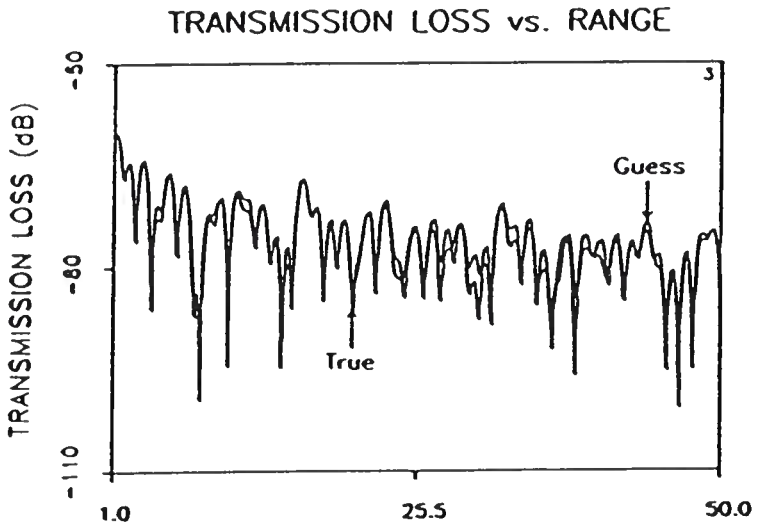

Figure 27. The true and background transmission loss curves for test case 3. Although the perturbation is small (1 m/s), it extends over 28% of the waveguide; therefore the guess transmission loss differs from the true.

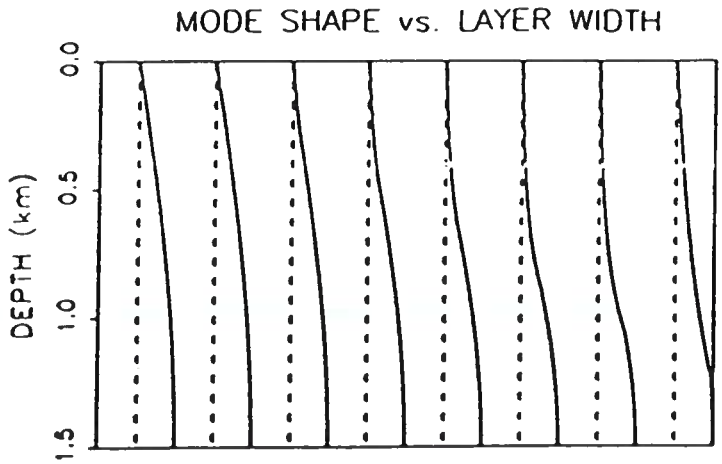

Figure 28. Illustrated is the variation of the lowest order mode in test case 3 as a function of layer depth. The curve on the far left represents the mode shape in a constant velocity waveguide and the second curve from the left is the mode shape when a 200 m layer is present, etc. The curve on the far right is the shape of the lowest order mode when a 1.4 km layer is present. When the layer extends to 1.5 km, the shape returns to that in a constant velocity waveguide.

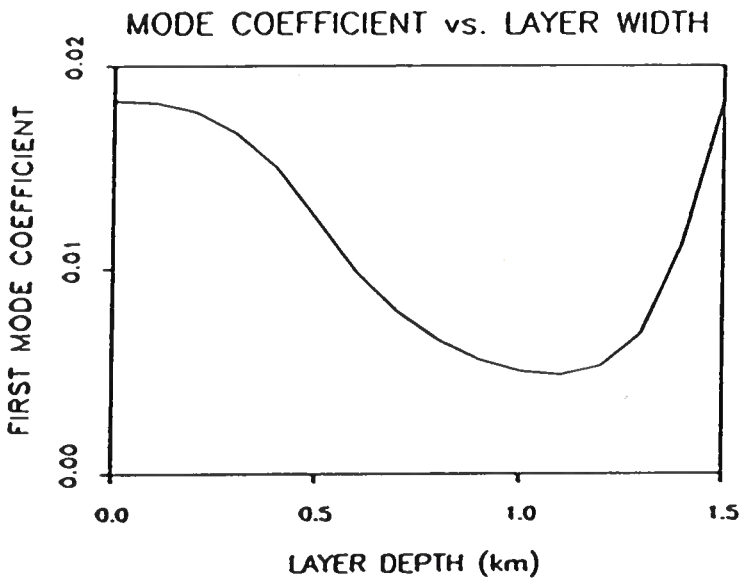

Figure 29. The change in the mode coefficient for the lowest-order mode as a function of the layer width. In a constant velocity waveguide, the numerical value is ~0.018. The value of the coefficient decreases to ~.005 at 1 km, and at 1.5 km returns to the original value of 0.018.

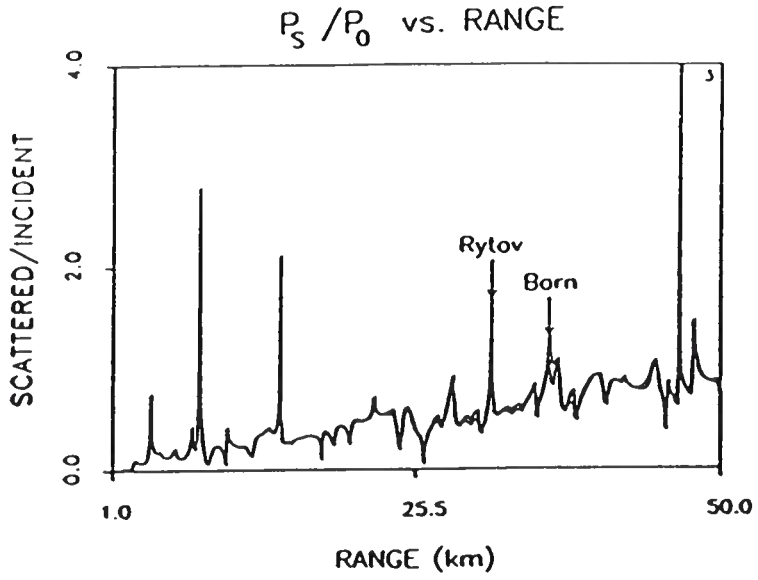

Figure 30. Ratio of the scattered field to the incident field for the Born and Rytov solutions for the two-layer waveguide of test case 3. Because large localized spikes are present in the ratios, the solutions are also expected to have large local errors.

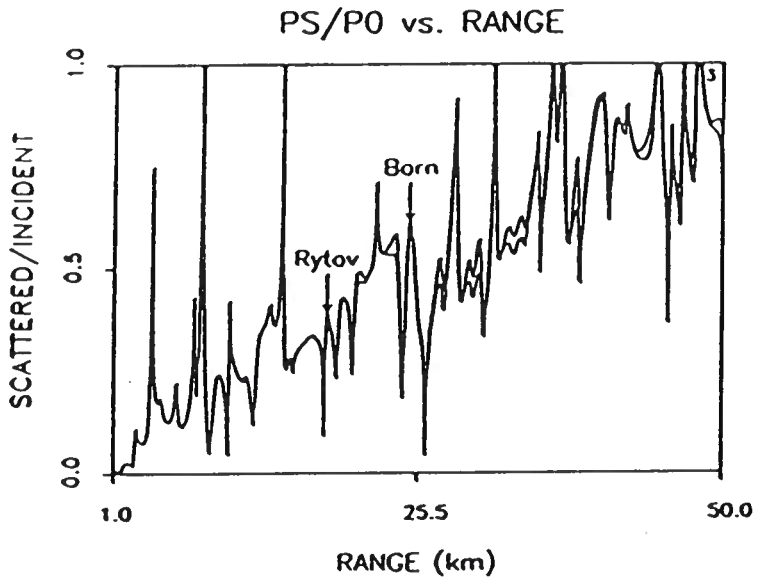

Figure 31. Expanded version of Figure 30. Note the trend of the ratio of both coefficients exceeds 1/4 by ~13 km; as a result a growth in the Born solution is predicted.

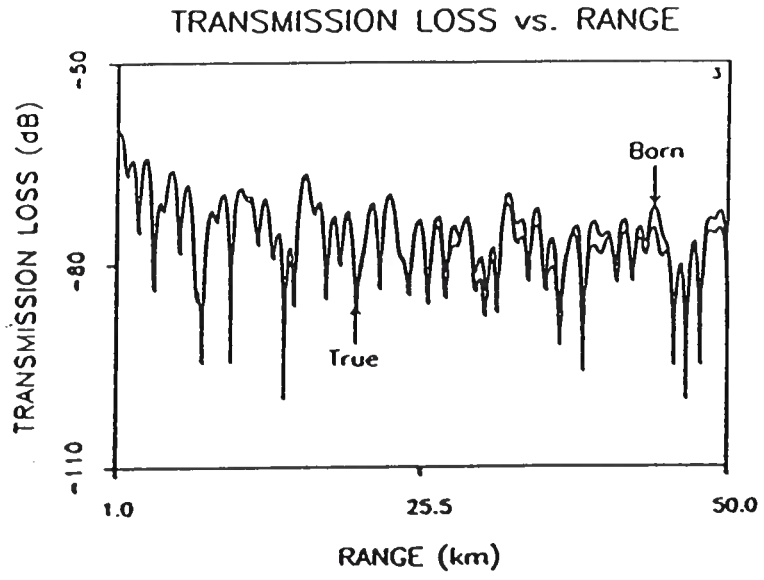

Figure 32. The true and Born transmission loss curves for test case 3. Although the Born reconstructs the general shape of the curve, the growth of the solution is apparent for ranges greater than ~13 km.

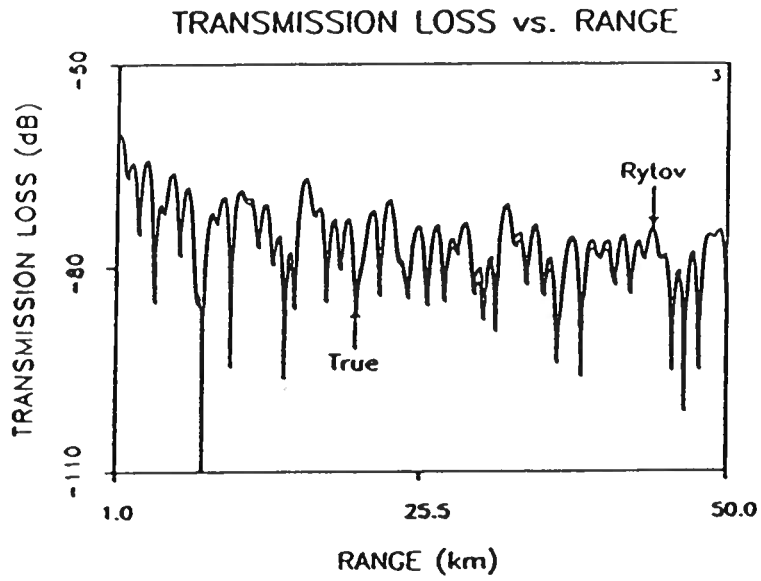

Figure 33. The true and Rytov transmission loss curves for test case 3. Although the Rytov approximates the true solution better than the Born, amplitude errors are apparent in both the nulls and peaks in the field.

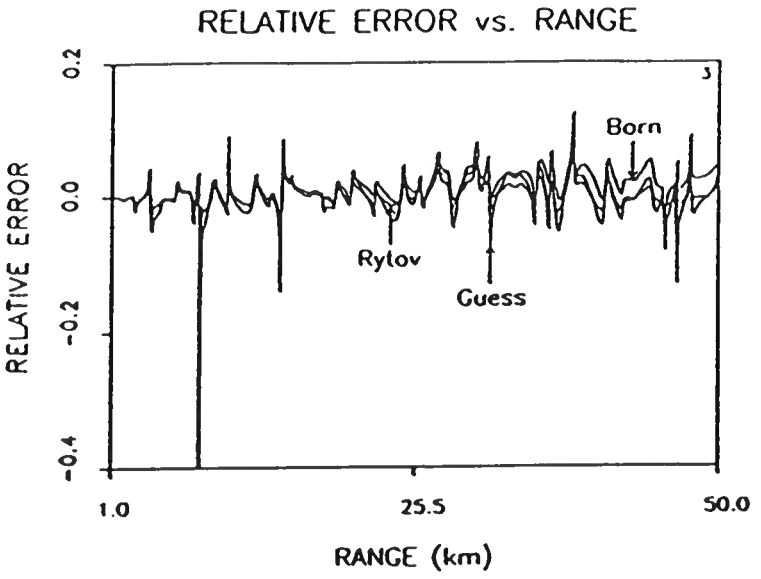

Figure 34. Relative error in the background, Born and Rytov transmission loss curves for test case 3. Although the Rytov has the least error, neither of the perturbative solutions were able to duplicate the true transmission loss curve.

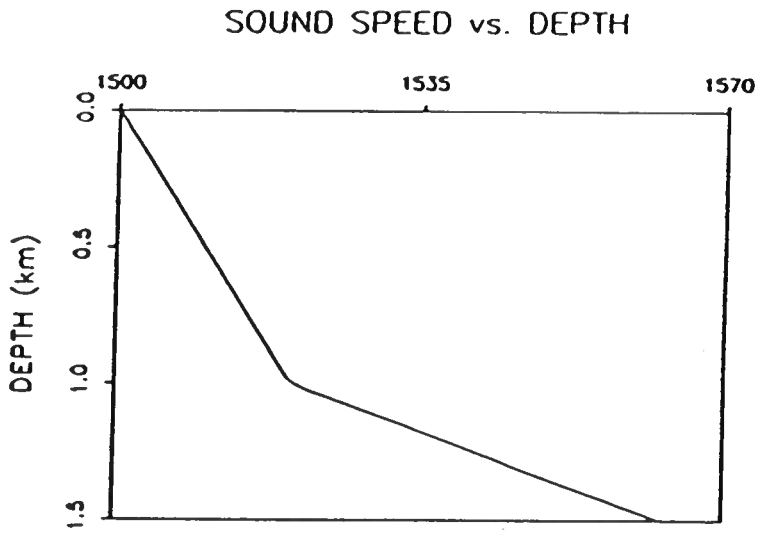

Figure 35. NORDA 2A bilinear background profile used in test cases 4 and 5.

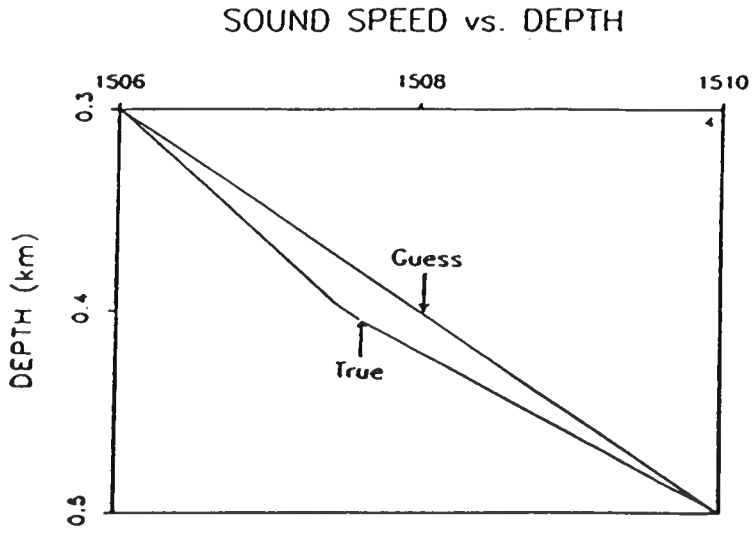

Figure 36. The profile perturbation used in test case 4. The perturbation extends from 300 to 500 m in depth and the maximum variation from the background is .5 m/s. In the remainder of the waveguide, the true sound speed matches the background.

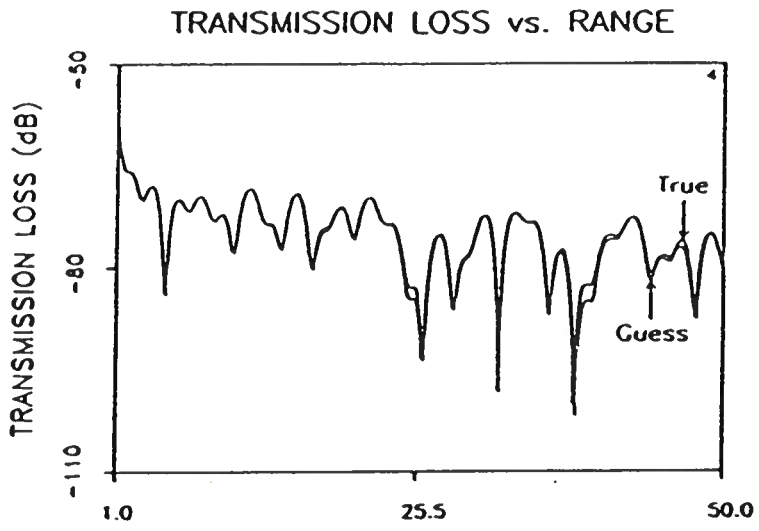

Figure 37. True and background transmission loss curves for test case 4. Although the maximum difference in sound speed is only 0.5 m/s, the perturbation extent is ~13% of the waveguide; therefore the curves differ as we propagate in range.

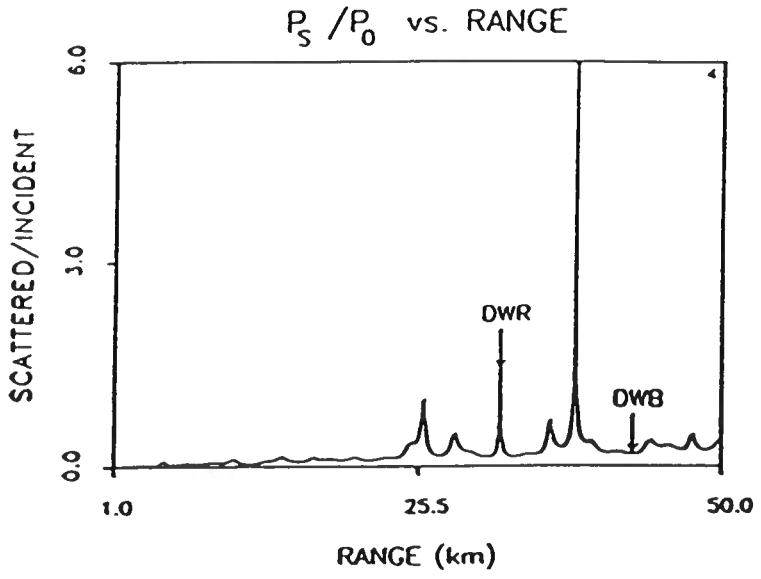

Figure 38. Ratio of the scattered field to the incident field for the DWB and DWR solutions for test case 4. The spike at ~40 km suggests the possibility of a local error in the solutions.

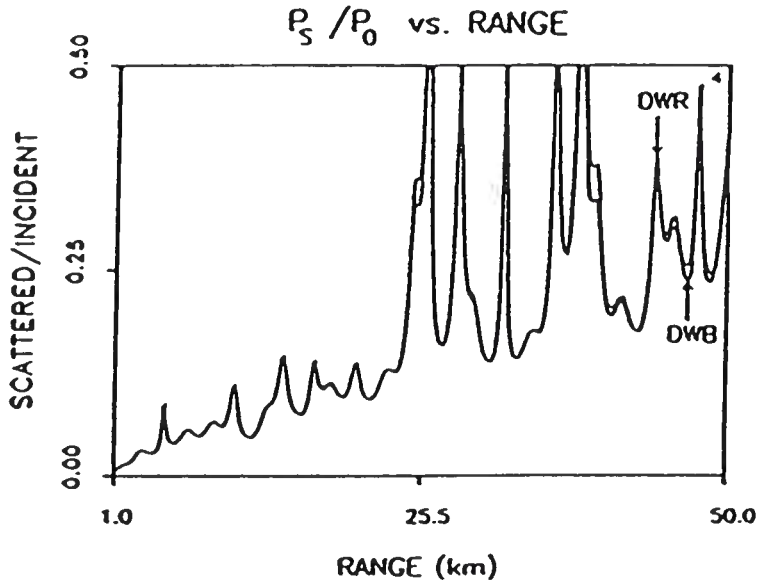

Figure 39. Expanded version of Figure 38. The trend of the ratios is less than 1/4 and the DWB and DWR are predicted to give accurate results.

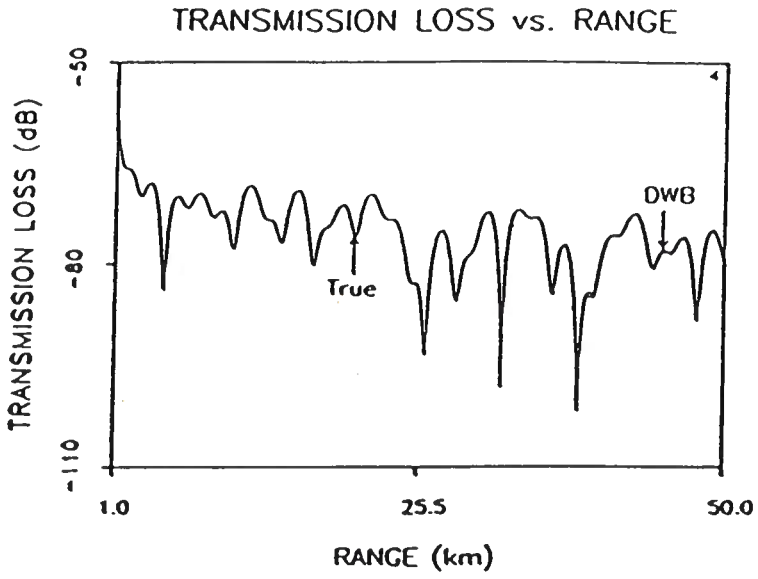

Figure 40. True and DWB transmission loss curves for test case 4. As predicted, the DWB is a good approximation to the true solution.

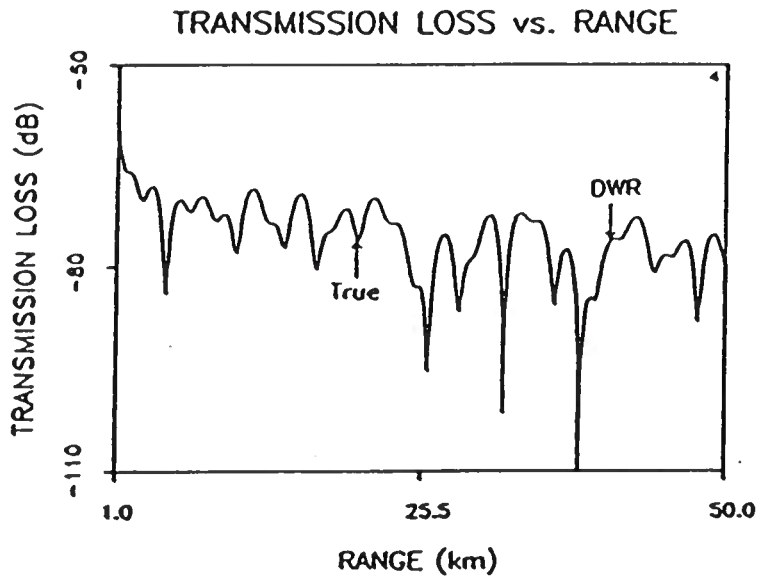

Figure 41. True and DWR transmission loss curves for test case 4. As predicted, the DWR is a good approximation to the true solution except at the null near 40 km.

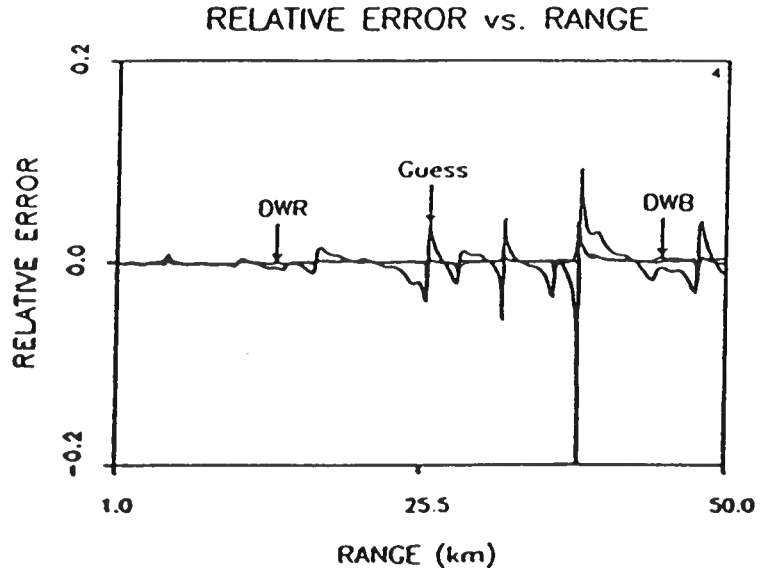

Figure 42. Relative error in the background, Born and Rytov transmission loss curves for test case 4.

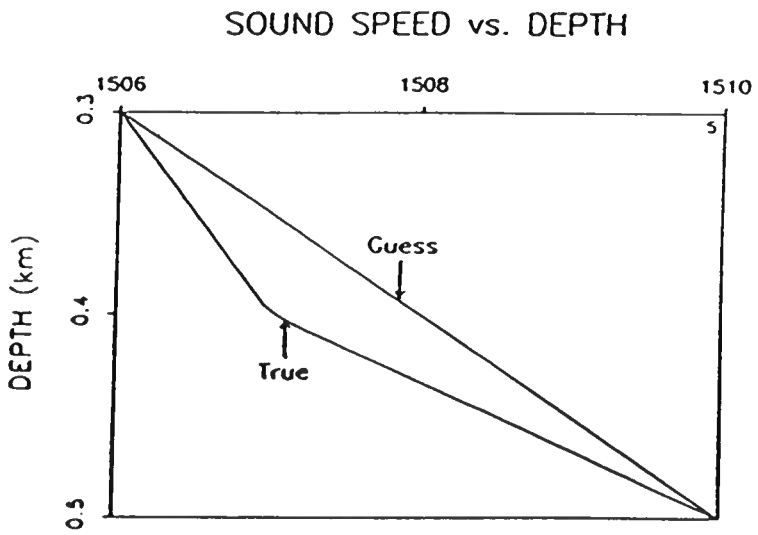

Figure 43. Profile perturbation for test case 5. The maximum variation from the background is now 1 m/s and the extent is ~13% of the waveguide.

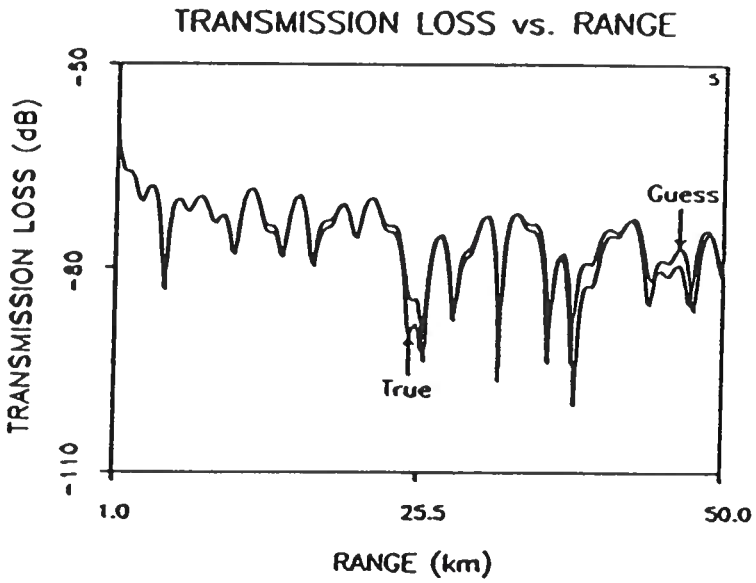

Figure 44. True and background transmission loss curves for test case 5. Note the difference in the two curves as compared to Figure 37.

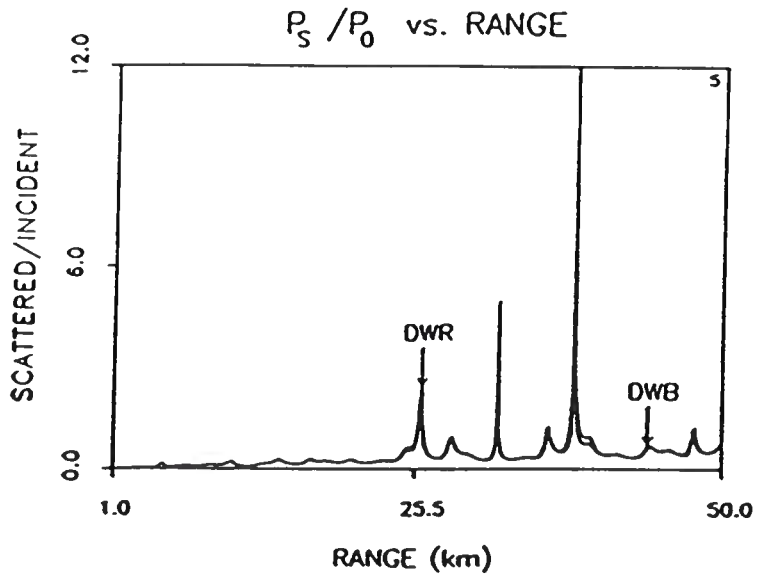

Figure 45. Ratio of the scattered field to the incident field for the DWB and DWR solutions for test case 5. As in Figure 38, the spike at ~40 km suggests the possibility of a local error the solutions.

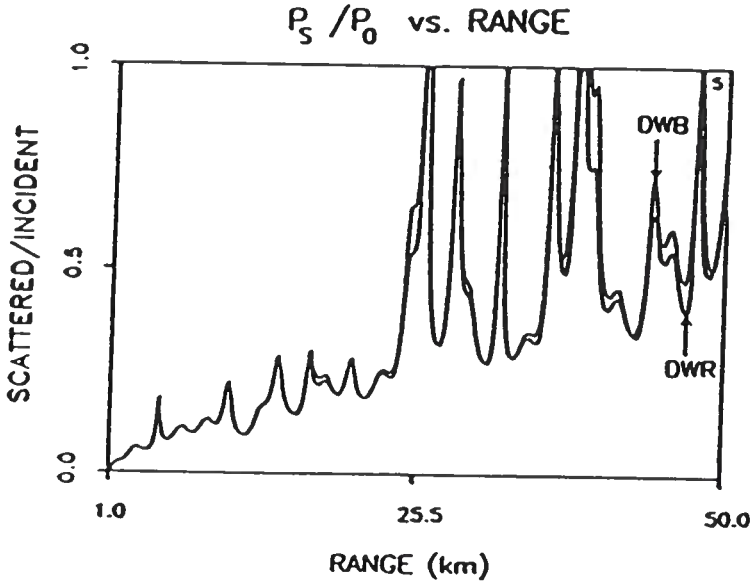

Figure 46. Expanded version of Figure 45. The DWB solution is expected to be in error past 25 km when the ratio exceeds 1/4.

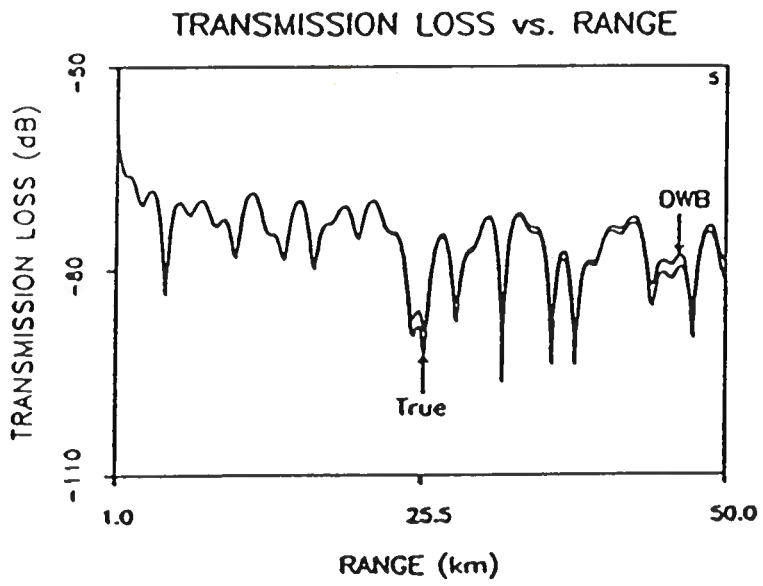

Figure 47. True and DWB transmission loss curves for test case 5. Although the shape of the curve is correct, the growth in the DWB solution for ranges greater than 25 km is evident.

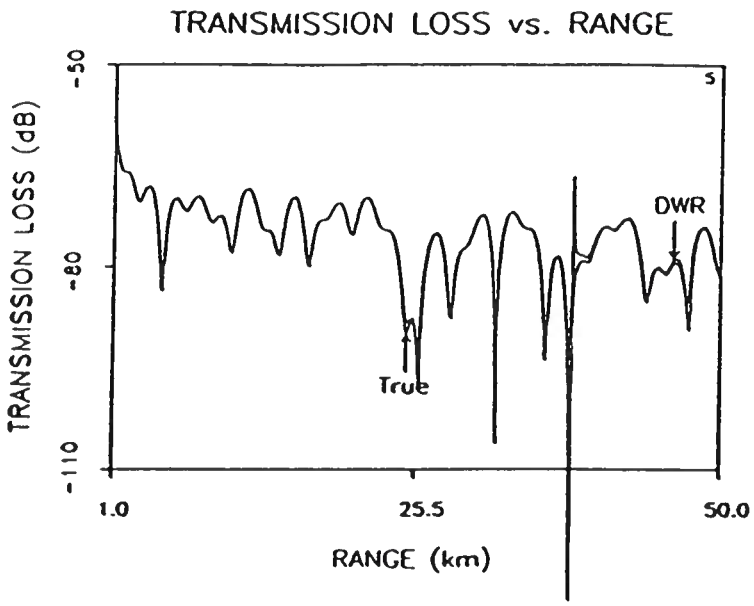

Figure 48. True and DWR transmission loss curves for test case 5. The error in the DWR solution near ~40 km has increased (compare Figure 41) and there are errors in the amplitude. In addition, the DWR fails to correctly position the nulls of the solution.

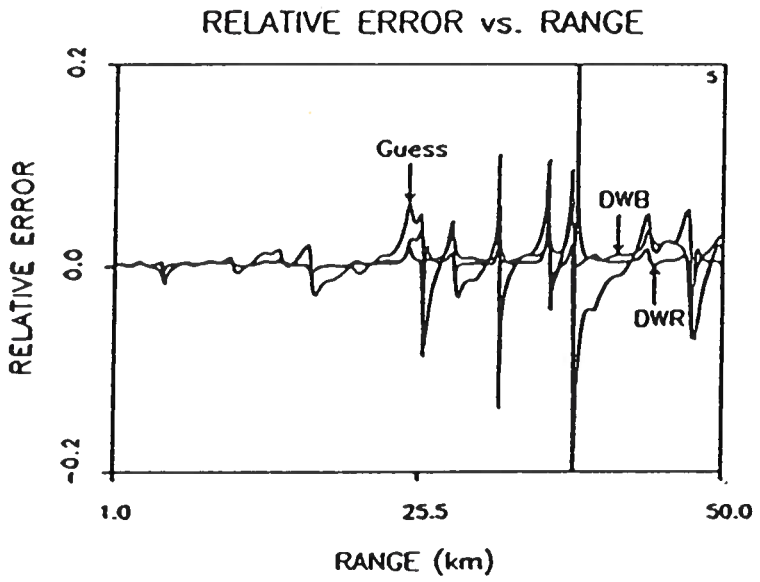

Figure 49. Relative error in the background, DWB and DWR transmission loss curves for test case 5. The vertical scale has been expanded to differentiate the errors.

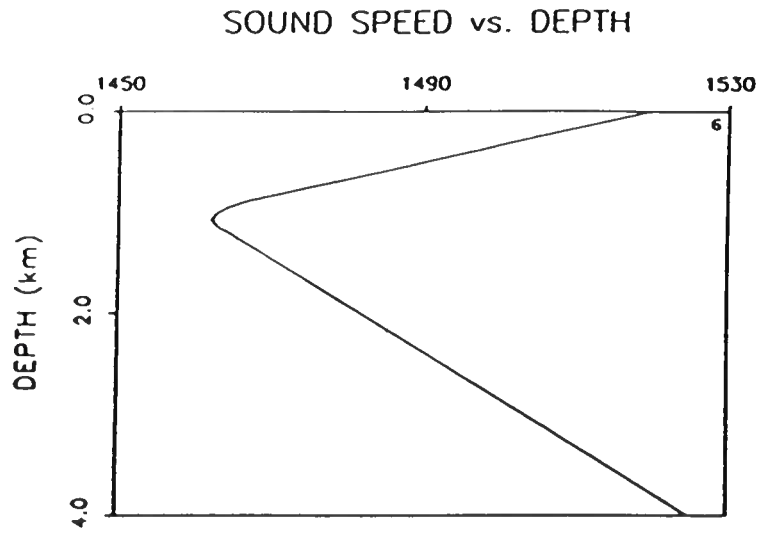

Figure 50. Background profile used in test cases 6 and 7.

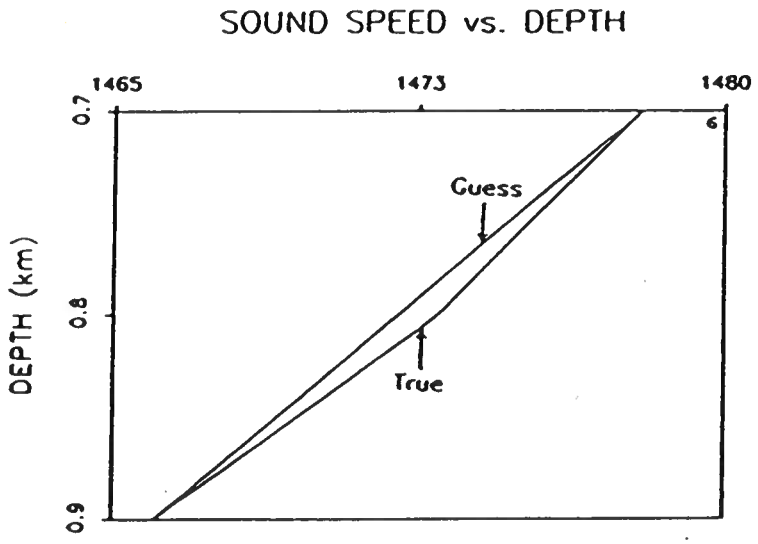

Figure 51. Profile perturbation for test cases 6 and 7. The maximum variation from the background is 1 m/s and the extent is ~5% of the waveguide.

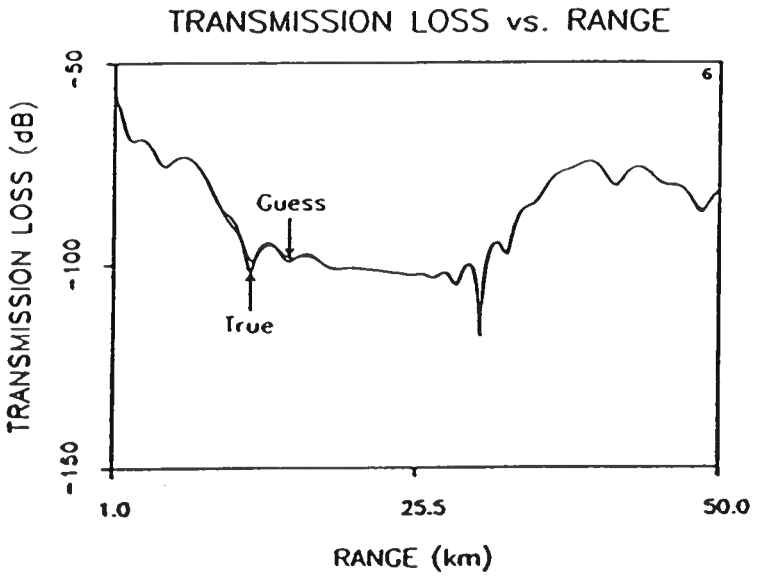

Figure 52. True and background transmission loss curves for test case 6. Note the broad region of low intensity.

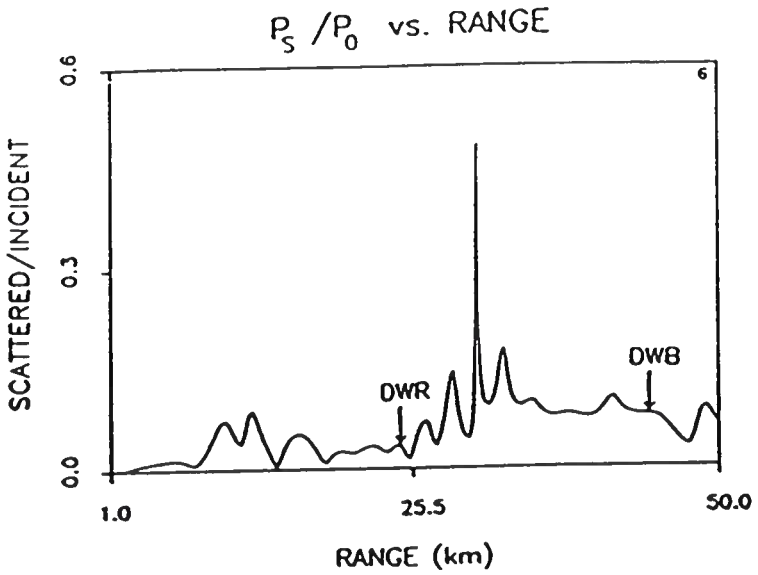

Figure 53. Ratio of the scattered field to the incident field for the DWB and DWR solutions for test case 6.

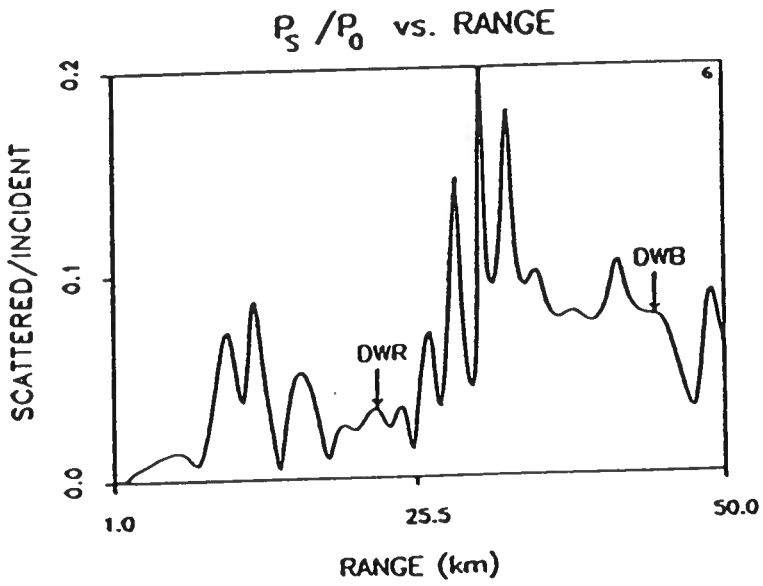

Figure 54. Expanded version of Figure 53. Note the maximum error occurs in the region of low intensity.

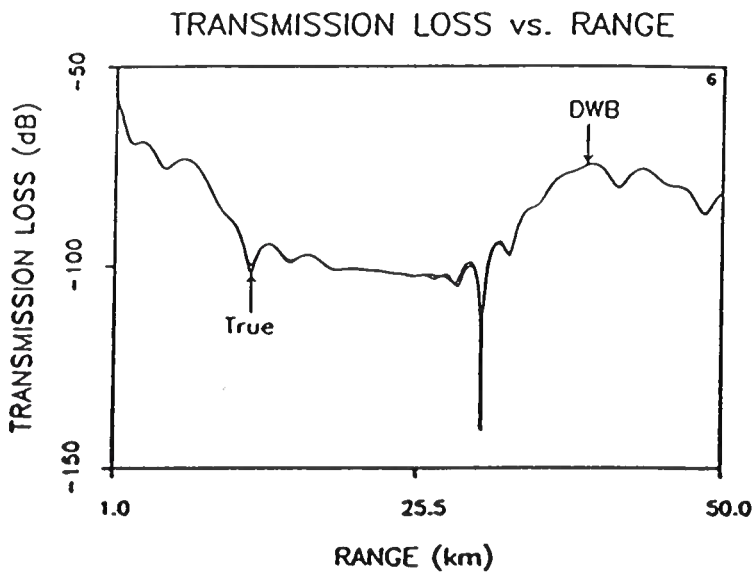

Figure 55. True and DWB transmission loss curves for test case 6. The vertical scale has been expanded to include the spike near 29 km.

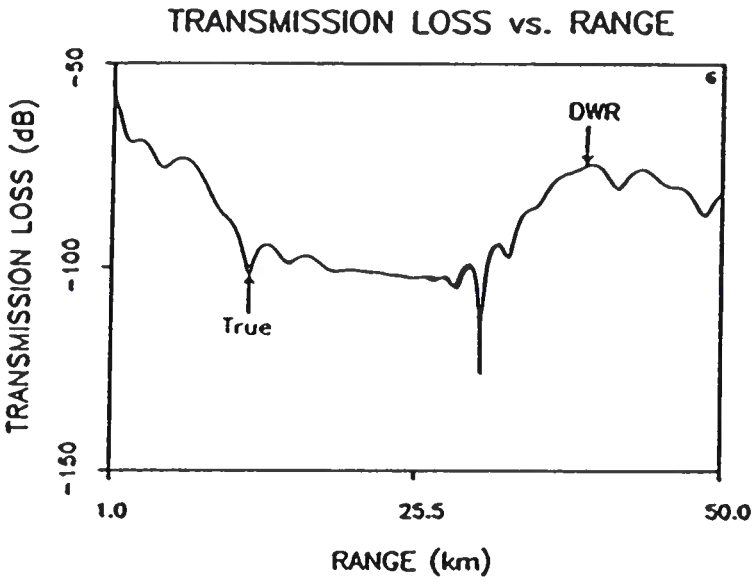

Figure 56. True and DWR transmission loss curves for test case 6. The vertical scale has been expanded to include the spike near 29 km.

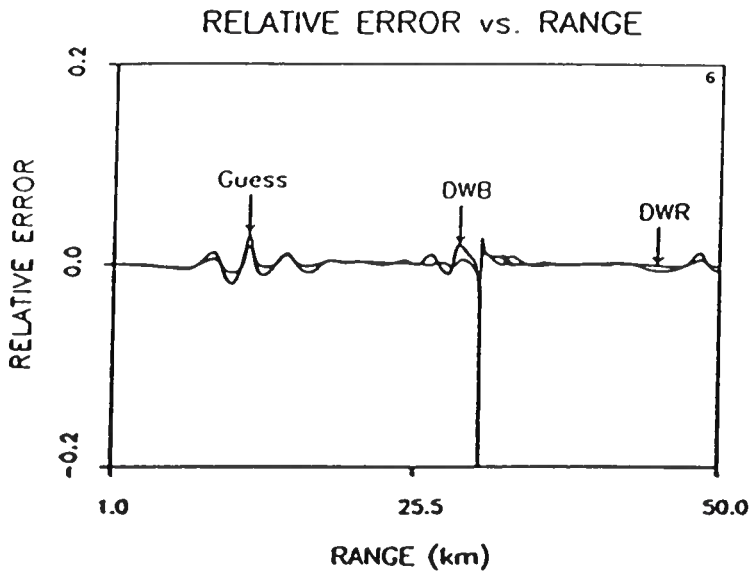

Figure 57. Relative error in the background, DWB and DWR transmission loss curves for test case 6.

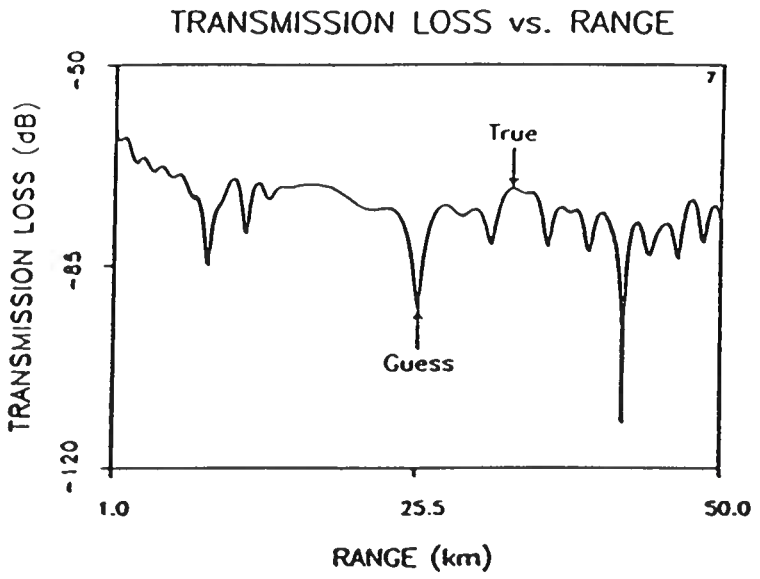

Figure 58. True and background transmission loss curves for test case 7. Because the source is placed on the channel axis, the shadow zone has disappeared.

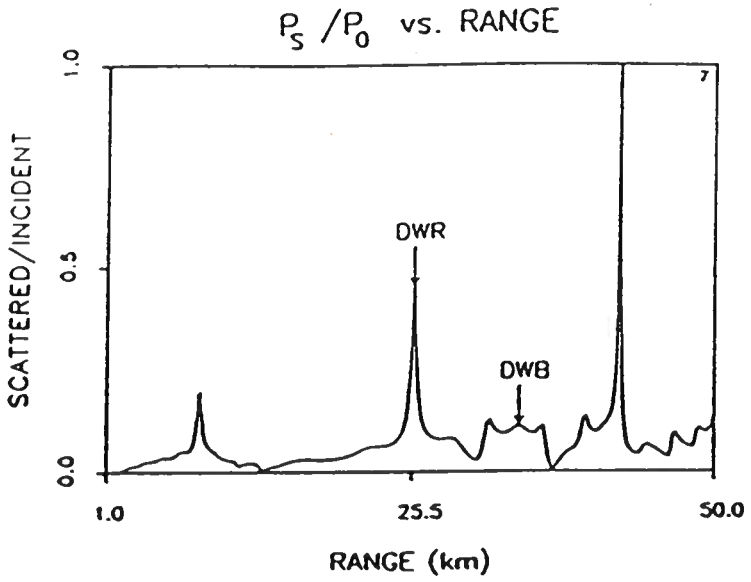

Figure 59. Ratio of the scattered field to the incident field for the DWB and DWR solutions for test case 7.

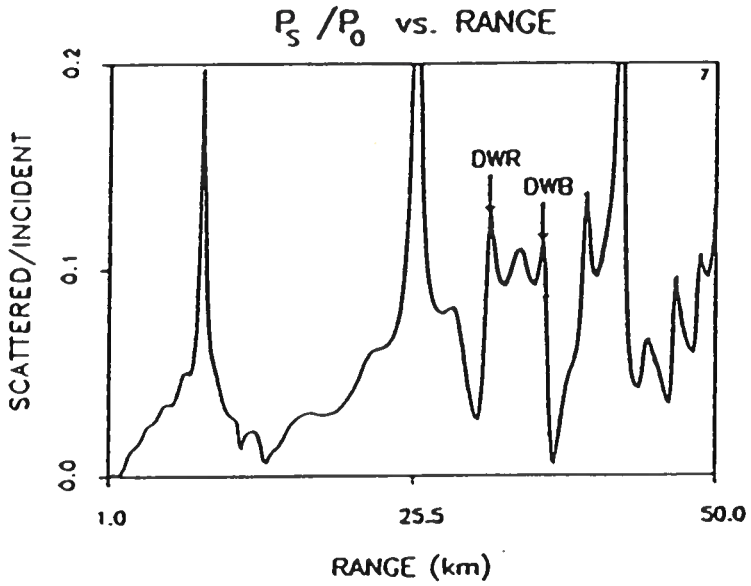

Figure 60. Expanded version of Figure 59. The ratio is always less than 1/4 and the DWB and DWR are expected to give accurate results.

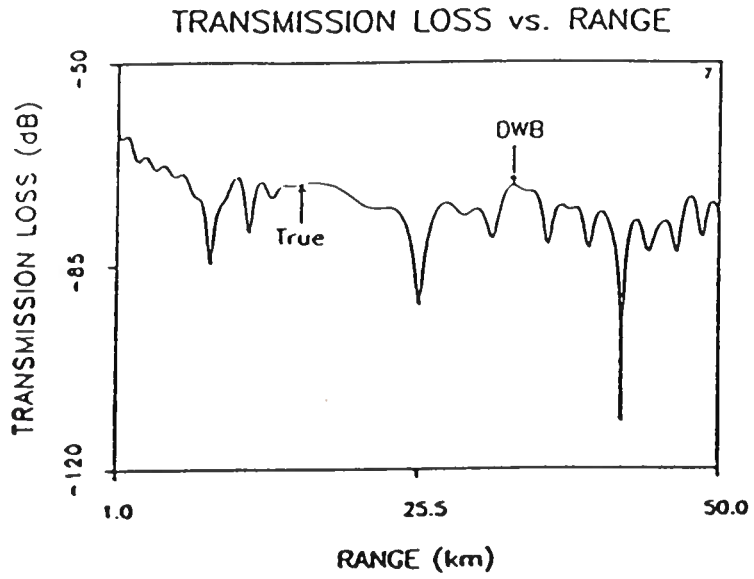

Figure 61. True and DWB transmission loss curves for test case 7. Because the waveguide is well-illuminated and the perturbation is small, the DWB gives a good approximation to the true solution.

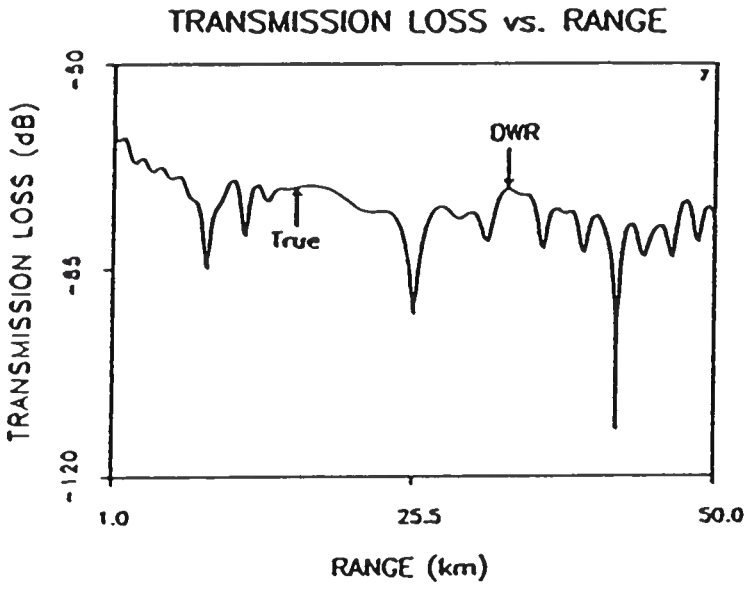

Figure 62. True and DWR transmission loss curves for test case 7. Because the waveguide is well-illuminated and the perturbation is small, the DWR gives a good approximation to the true solution.

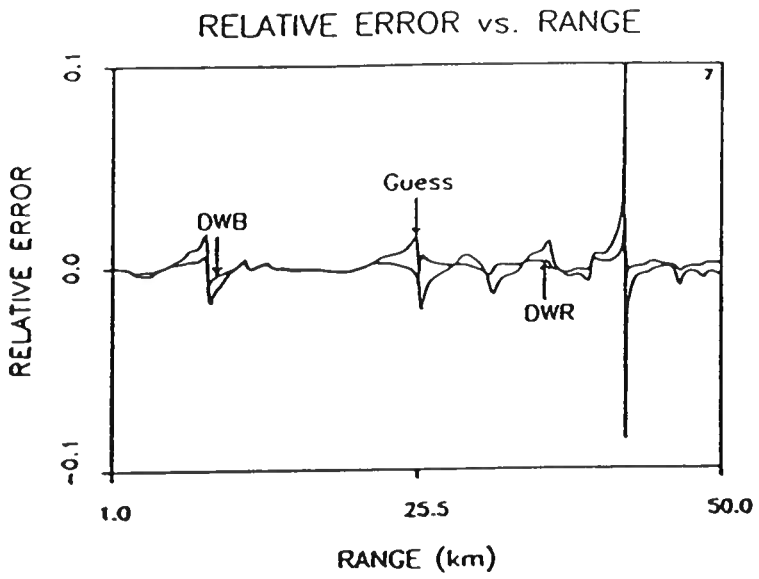

Figure 63. Relative error in the background, DWB and DWR transmission loss curves for test case 7.

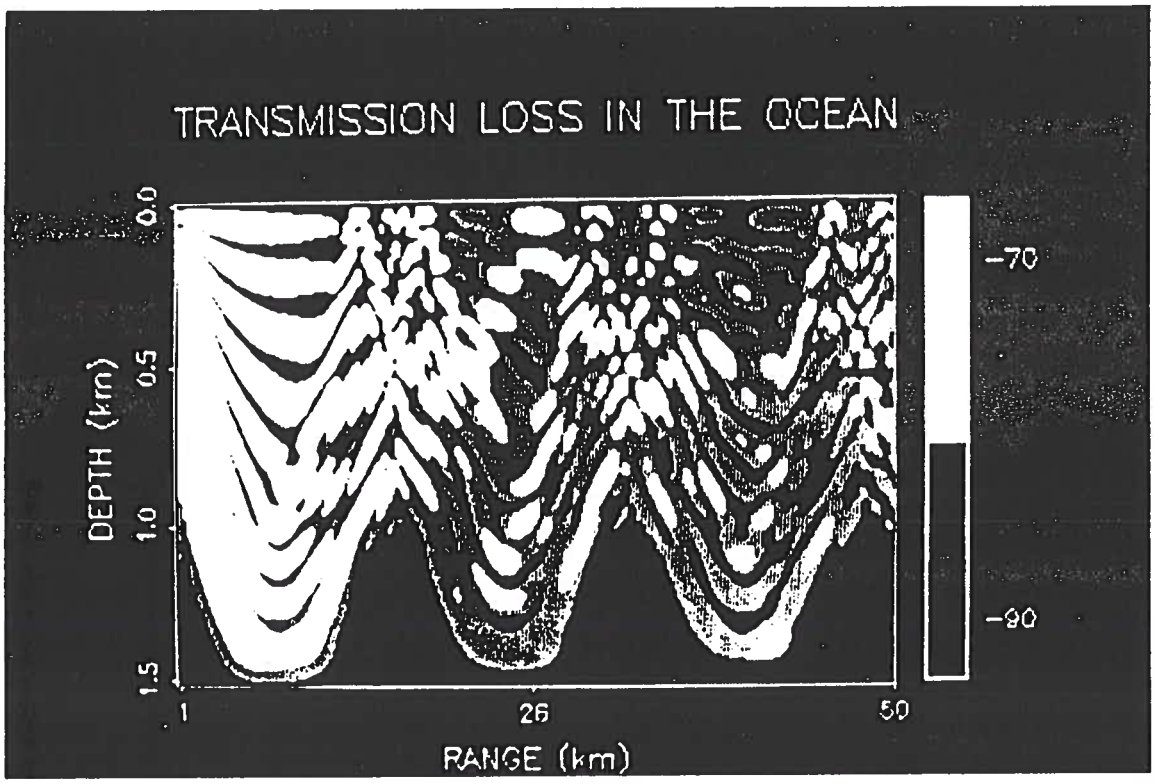

Figure 64. Transmission loss for the NORDA 2A profile illustrated in Figure 35. The source is placed at a depth of .5 km and the source frequency is 50 Hz.

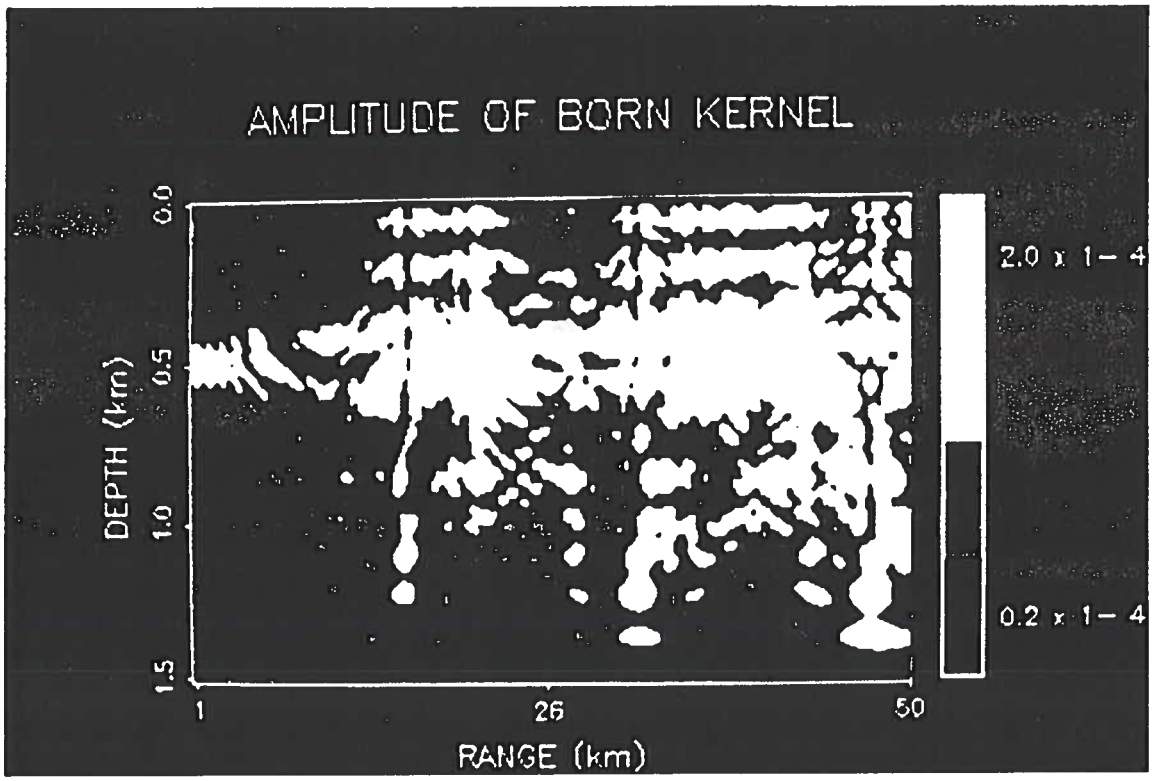

Figure 65. Amplitude of the DWB kernel for the NORDA 2A profile. The source is placed at a depth of .5 km and the source frequency is 50 Hz. Note the position of the lower turning points as compared to Figure 64.

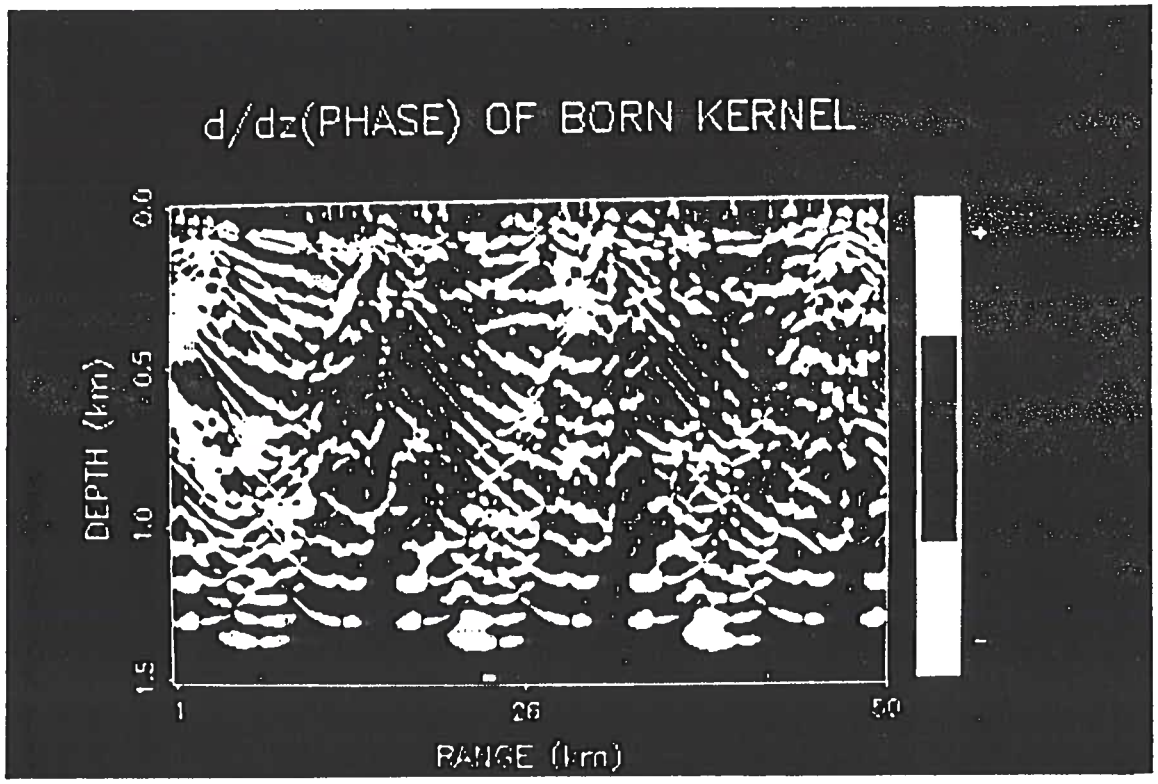

Figure 66. Derivative of the phase with respect to depth for the NORDA 2A profile. The source is placed at a depth of .5 km and the source frequency is 50 Hz. The complicated pattern of zero crossings is due to the interference of reflected and refracted energy.

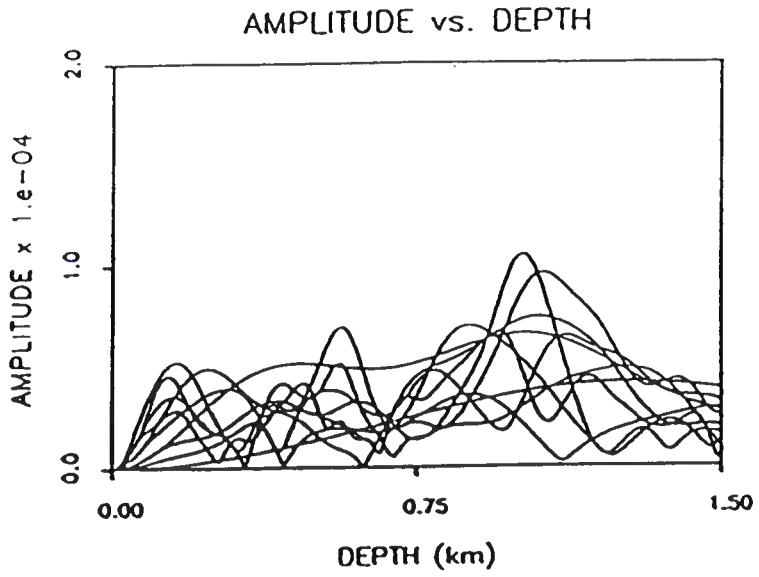

Figure 67. Amplitude of DWB kernel for 10 source frequencies generated using the NORDA 2A profile. The source depth is .5 km and the range is 30 km.

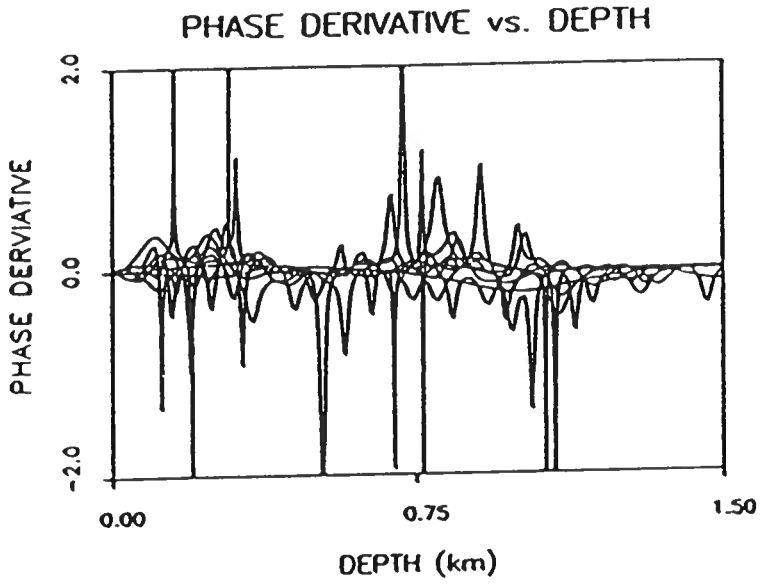

Figure 68. Derivative of the phase with respect to depth for 10 source frequencies generated using the NORDA 2A profile. The source depth is .5 km and the range is 30 km.

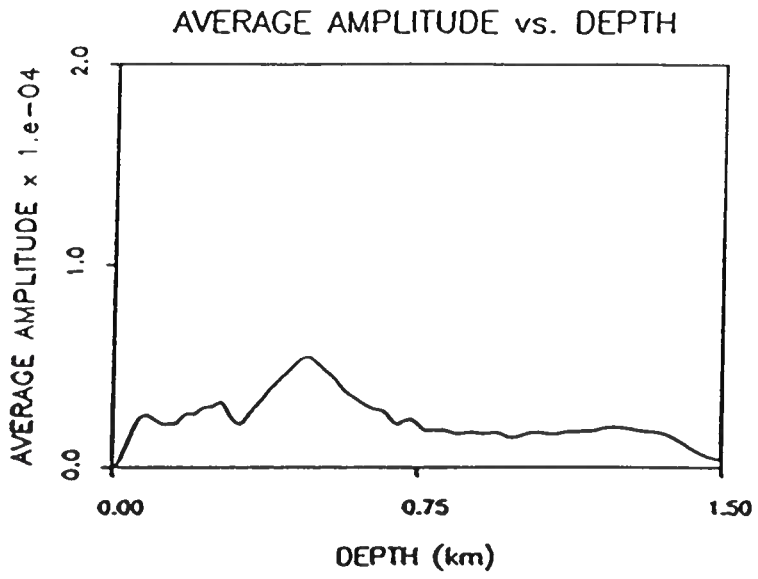

Figure 69. Frequency-averaged amplitude of DWB kernel generated using the NORDA 2A profile. The source depth is .5 km and the range is 30 km.

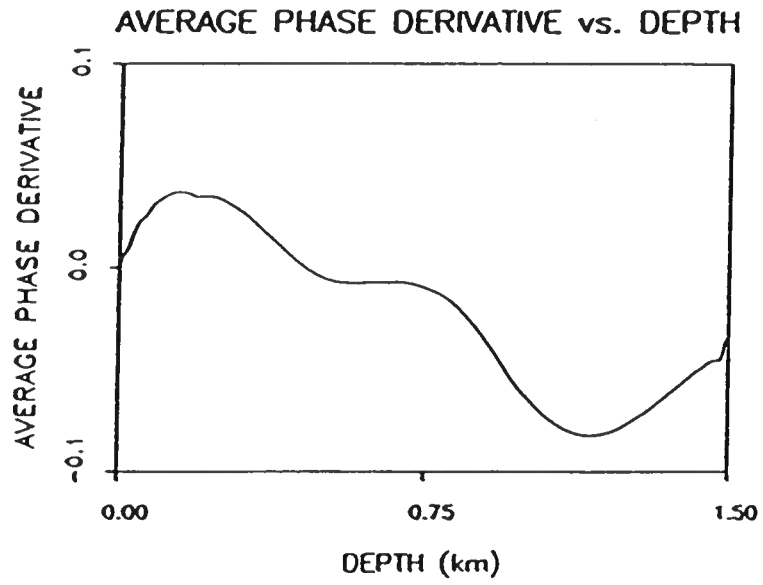

Figure 70. Frequency and depth-averaged derivative of the phase with respect to depth generated using the NORDA 2A profile. The source depth is .5 km and the range is 30 km.

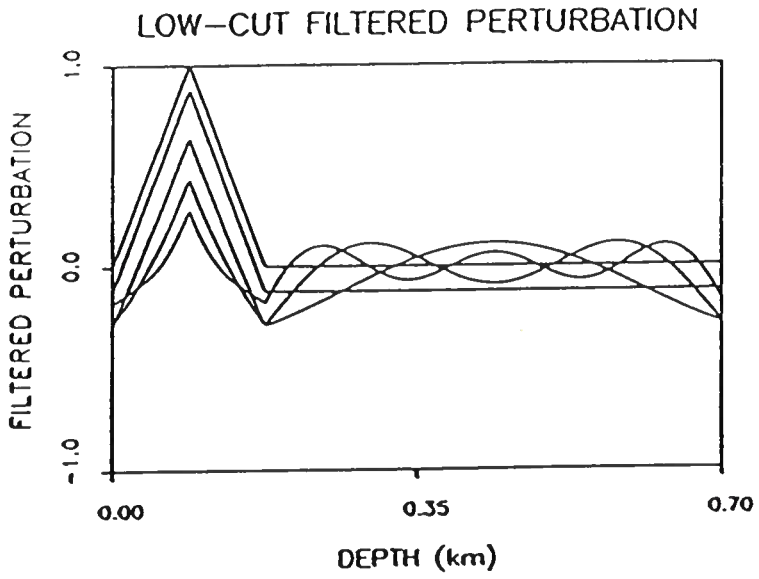

Figure 71. Effect of low-cut filtering on the Fourier reconstruction of a positive triangular perturbation.

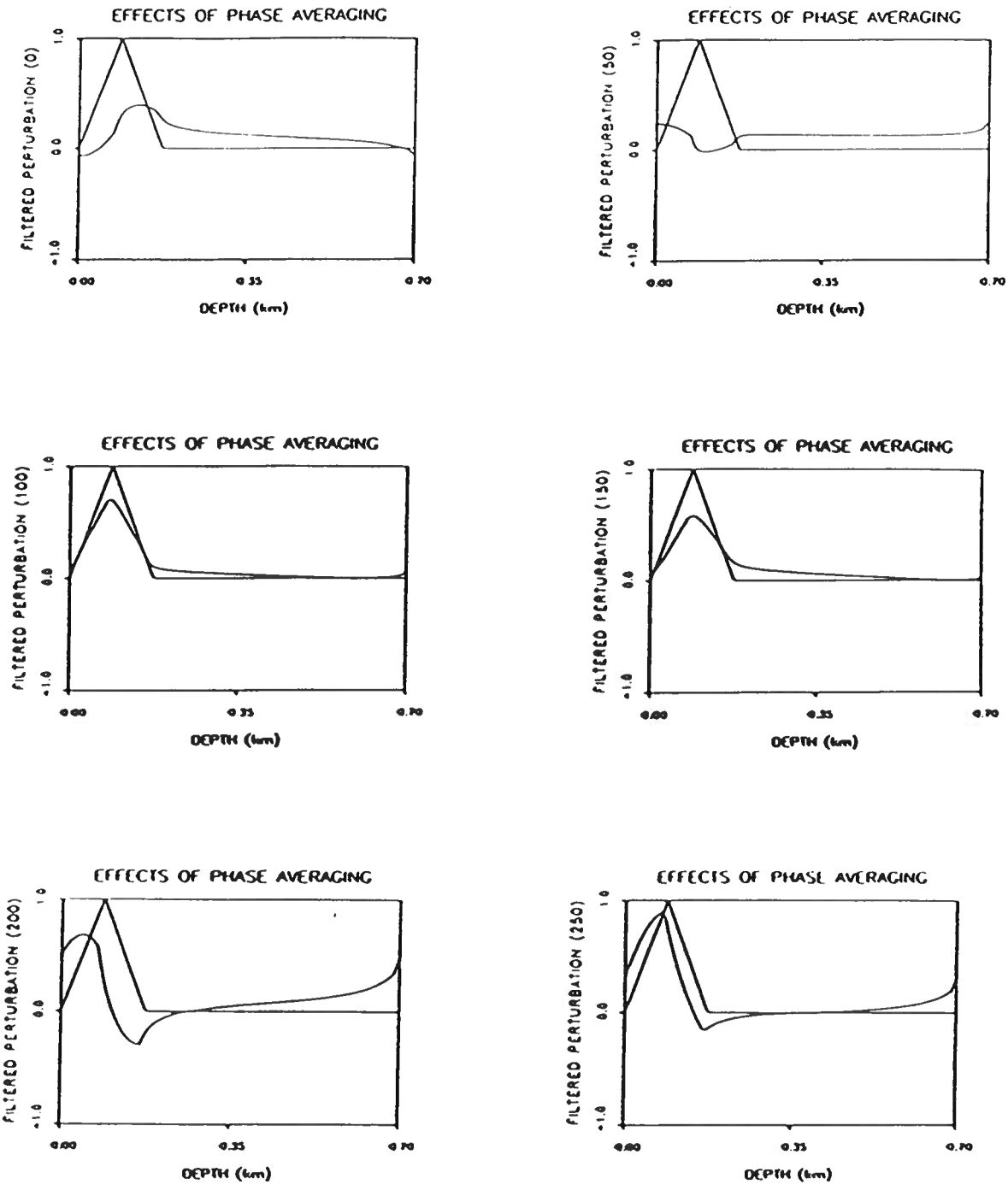

Figure 72. Effect of phase-averaging on the Fourier reconstruction of a positive triangular perturbation.

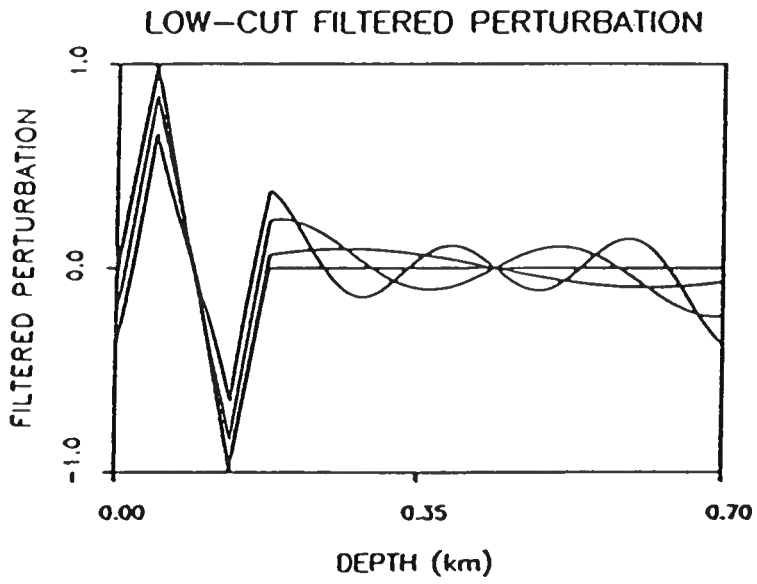

Figure 73. Effect of low-cut filtering on the Fourier reconstruction of a symmetric (about zero) perturbation.

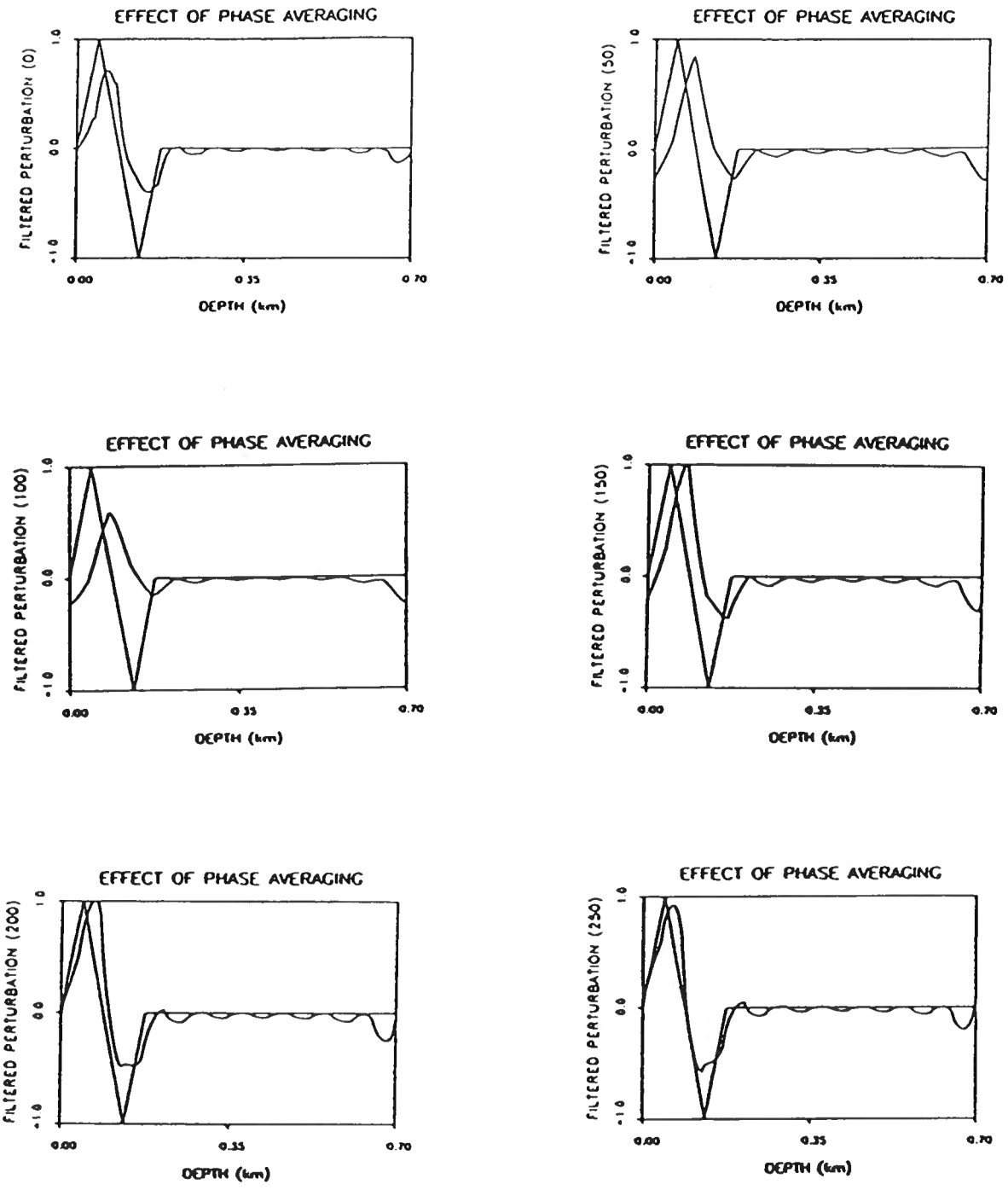

Figure 74. Effect of phase-averaging on the Fourier reconstruction of a symmetric perturbation.

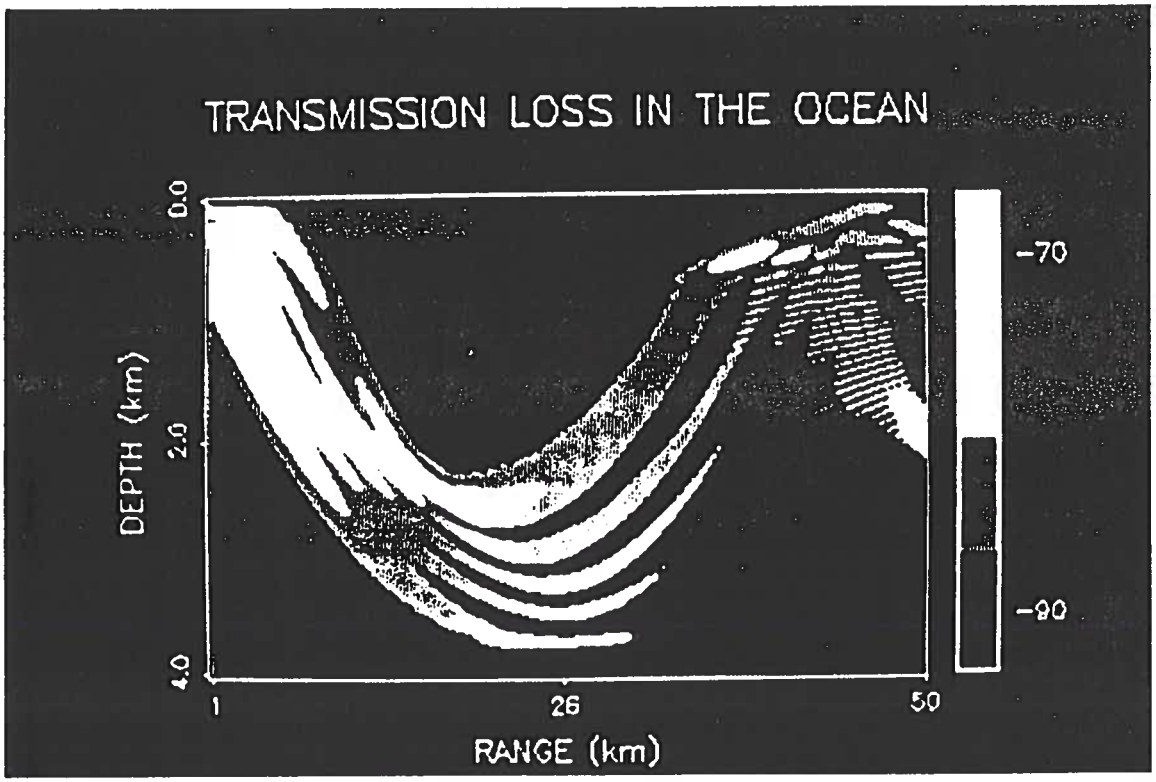

Figure 75. Transmission loss calculated using the profile and source-receiver geometry of test case 6. The source frequency is 50 Hz.

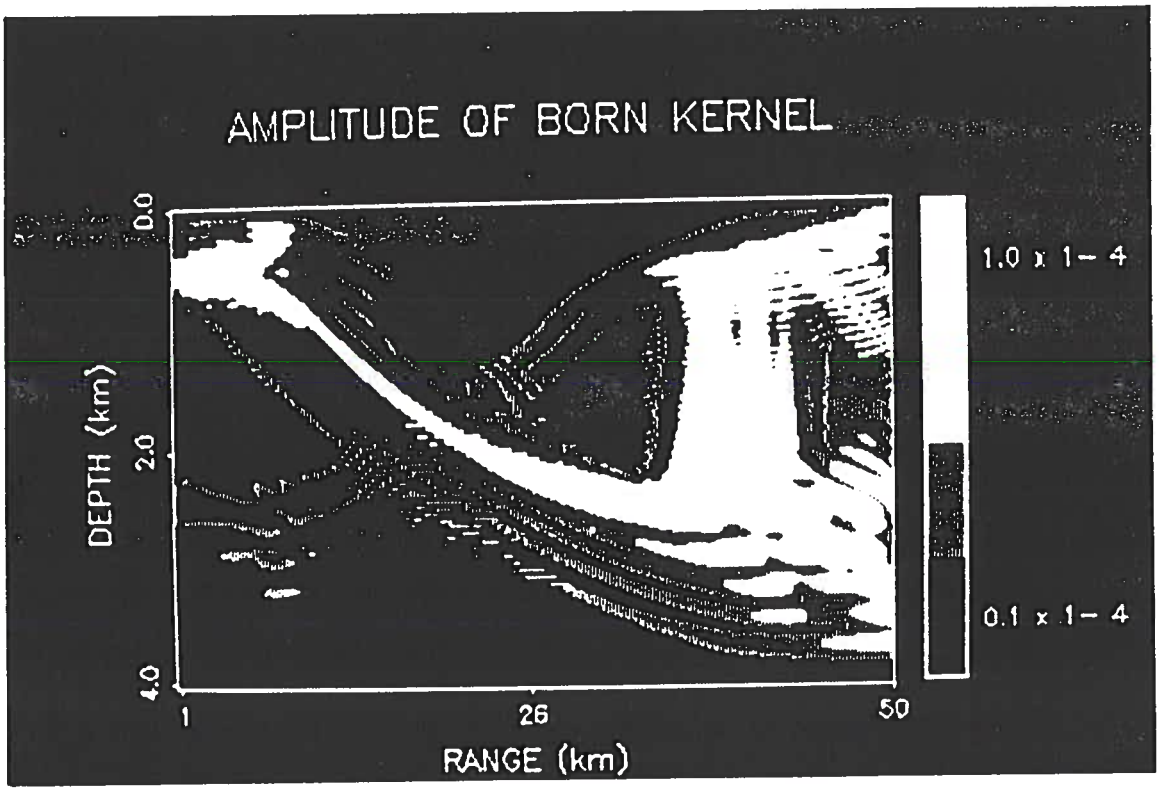

Figure 76. Amplitude of the DWB kernel calculated using the profile and source-receiver geometry of test case 6. Note the trapping of energy in narrow bands due to the source placement.

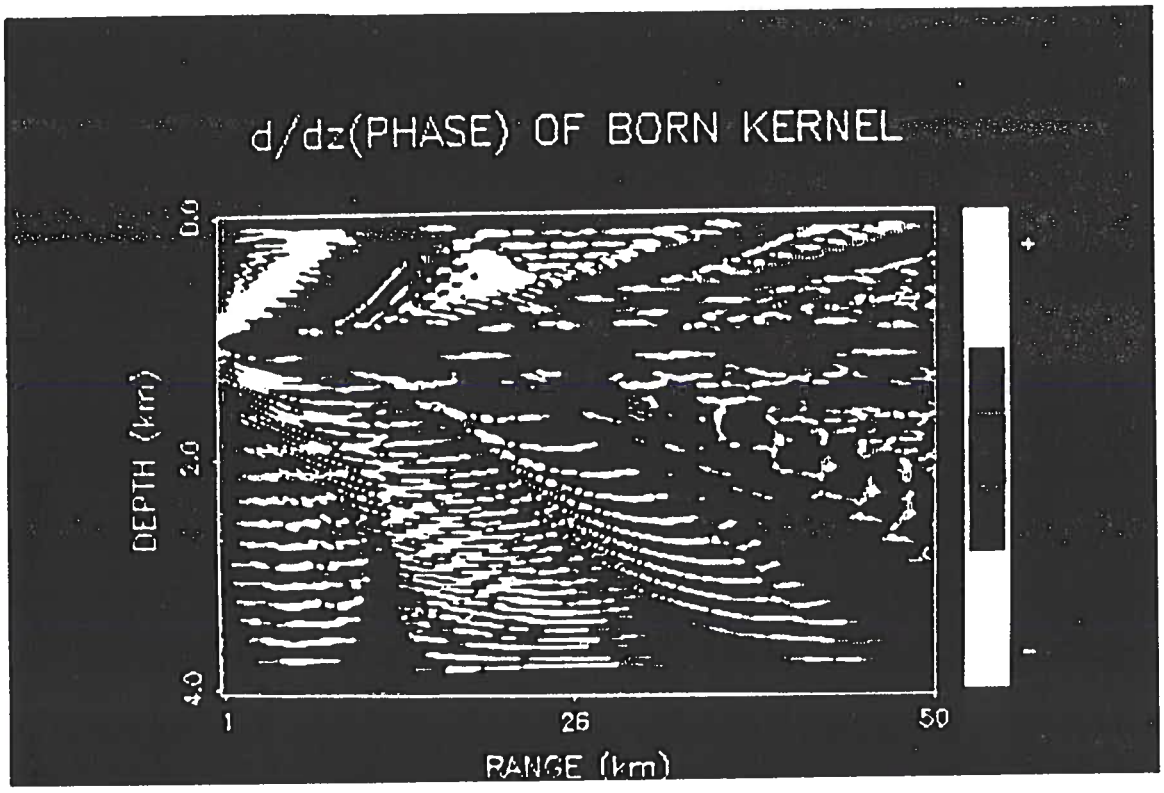

Figure 77. Derivative of the phase with respect to depth calculated using the profile and source-receiver geometry of test case 6. As compared to Figure 66, there are broad regions in depth for which the phase is monotonic.

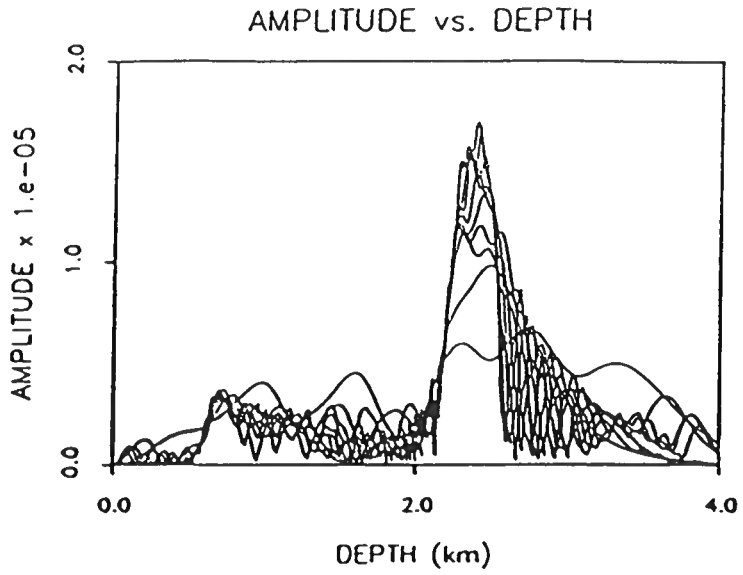

Figure 78. Amplitude of DWB kernel for 10 source frequencies generated using the profile and source-receiver geometry of test case 6. The range is 30 km.

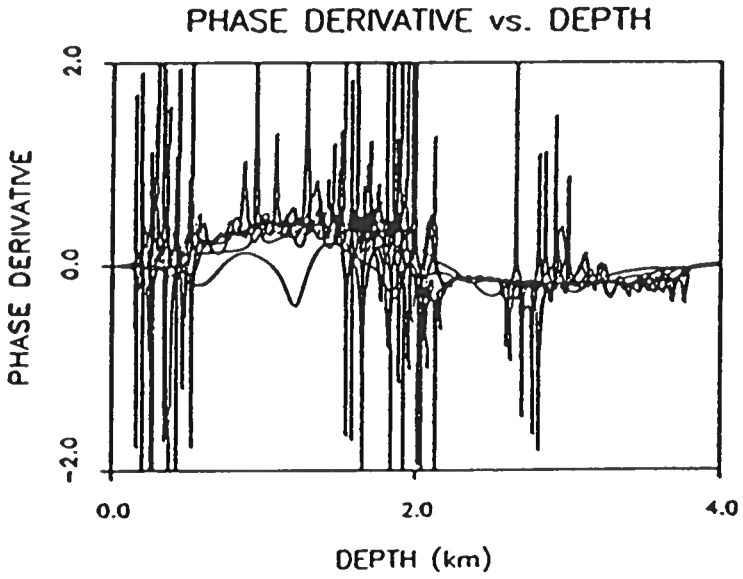

Figure 79. Derivative of the phase with respect to depth for 10 source frequencies generated using the profile and source-receiver geometry of test case 6. The range is 30 km.

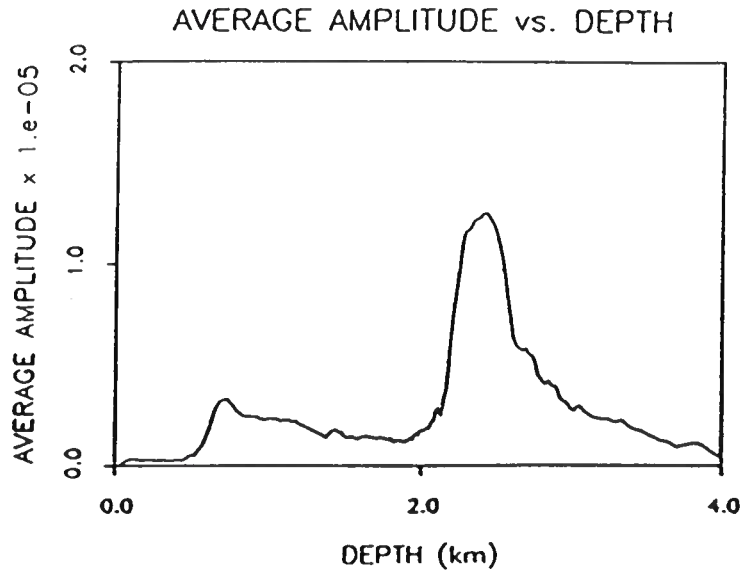

Figure 80. Frequency-averaged amplitude of DWB kernel generated using the profile and source-receiver geometry of test case 6. The range is 30 km.

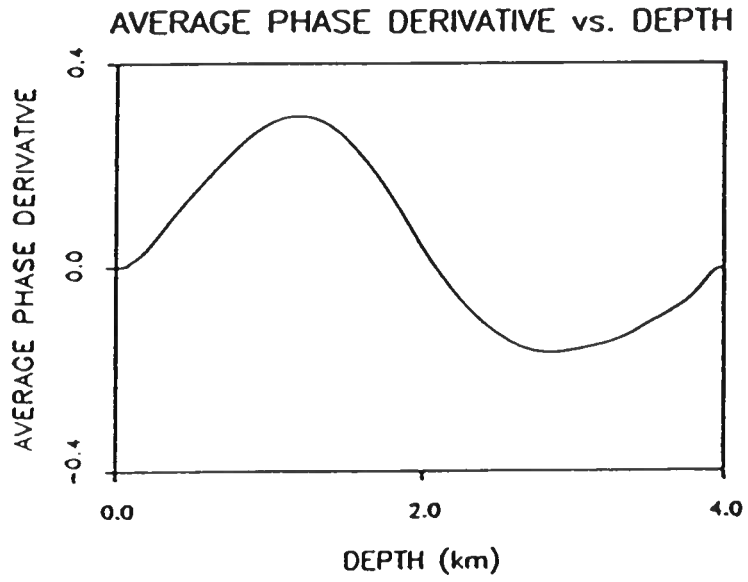

Figure 81. Frequency and depth-averaged derivative of the phase with respect to depth generated using the profile and source-receiver geometry of test case 6. The range is 30 km.

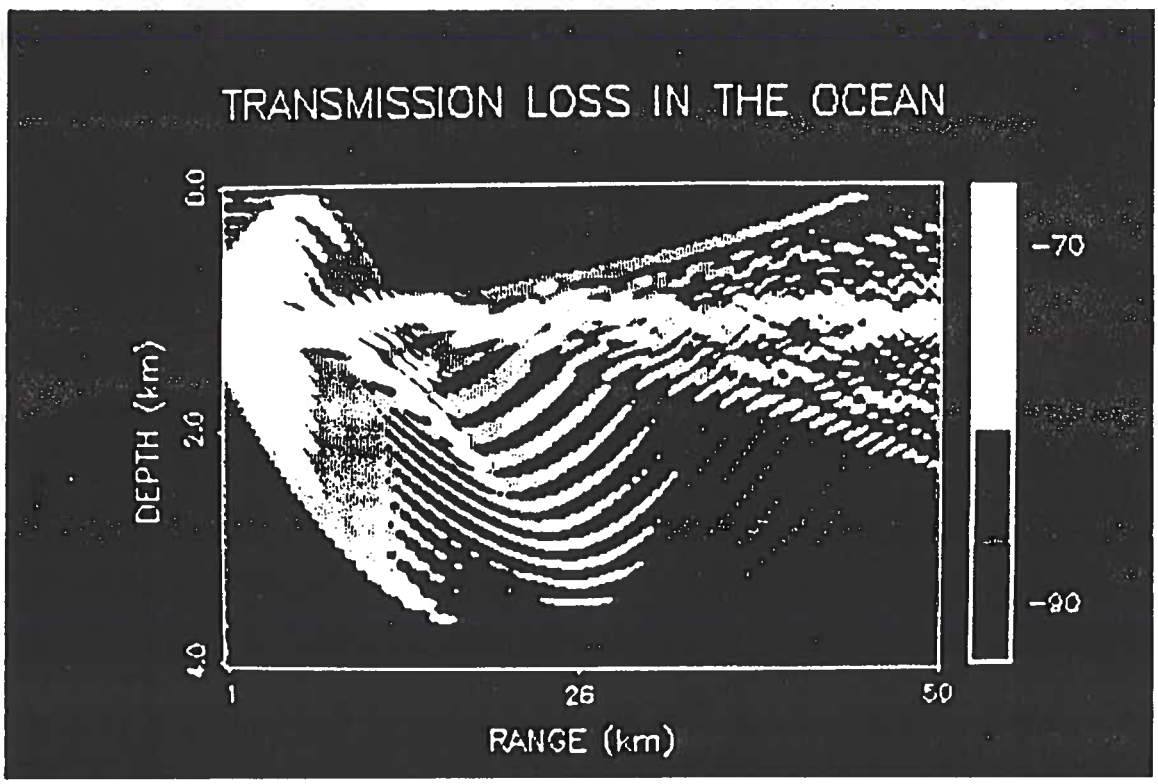

Figure 82. Transmission loss generated using the profile and source-receiver geometry of test case 7. The source frequency is 50 Hz.

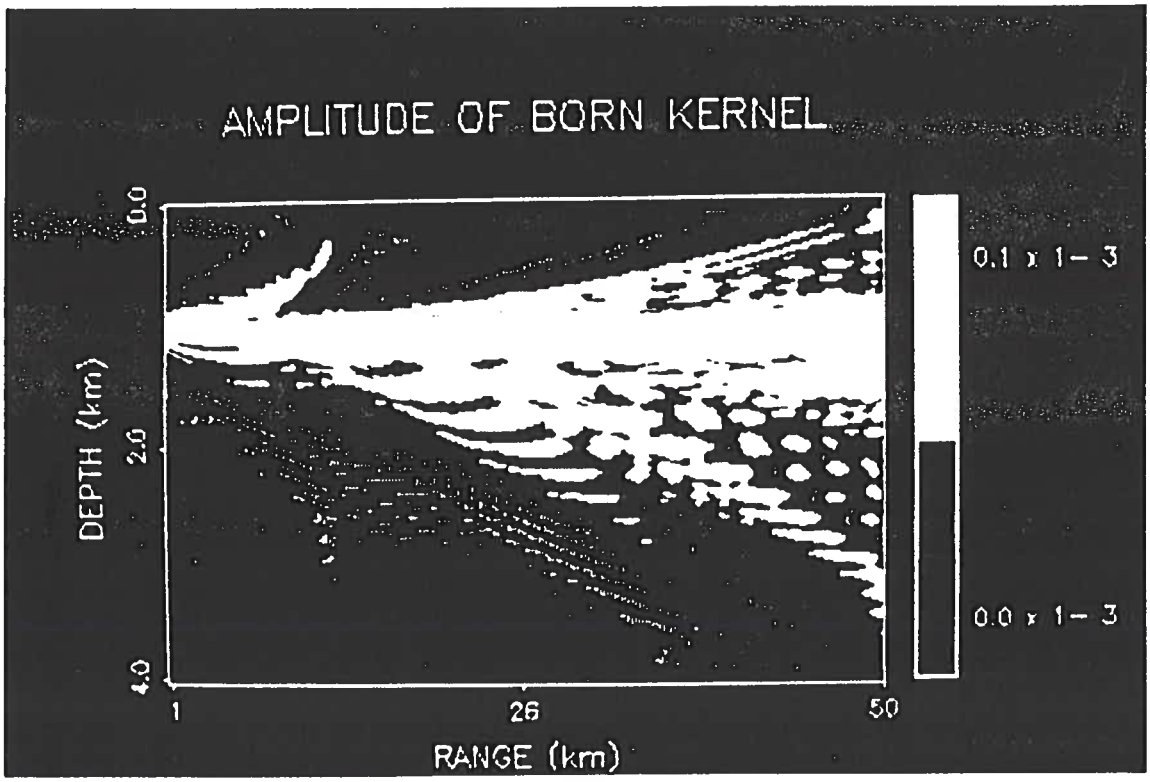

Figure 83. Amplitude of the DWB kernel generated using the profile and source-receiver geometry of test case 7. Note the trapping of energy near the channel axis.

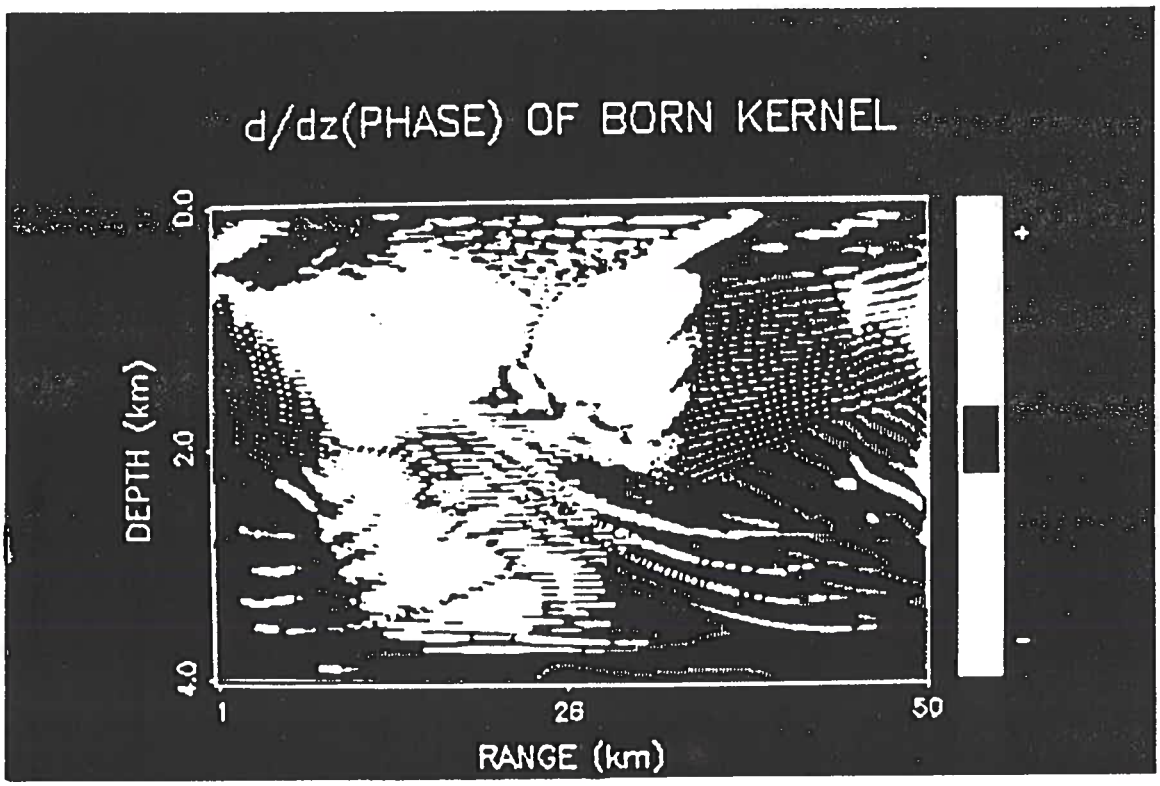

Figure 84. Derivative of the phase with respect to depth generated using the profile and source-receiver geometry of test case 7. As in Figure 66, there are many zero crossings. In this case the turning points are due to refraction within the waveguide.

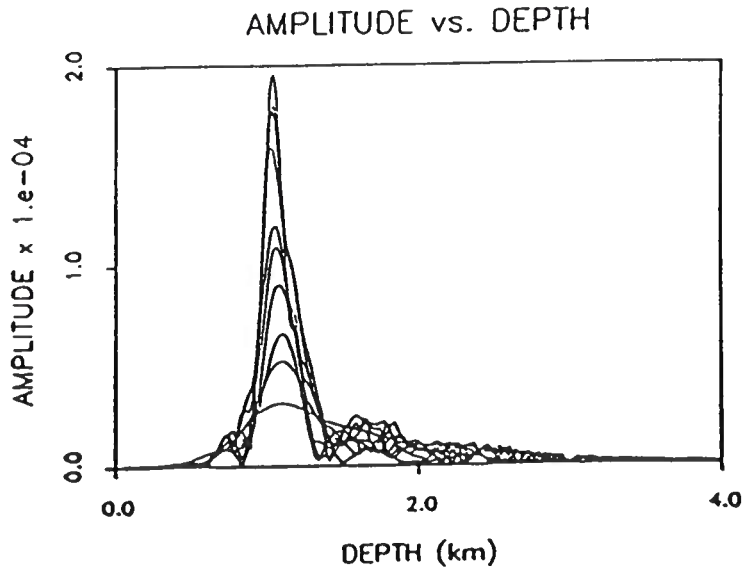

Figure 85. Amplitude of DWB kernel for 10 source frequencies generated using the profile and source-receiver geometry of test case 7. The range is 30 km.

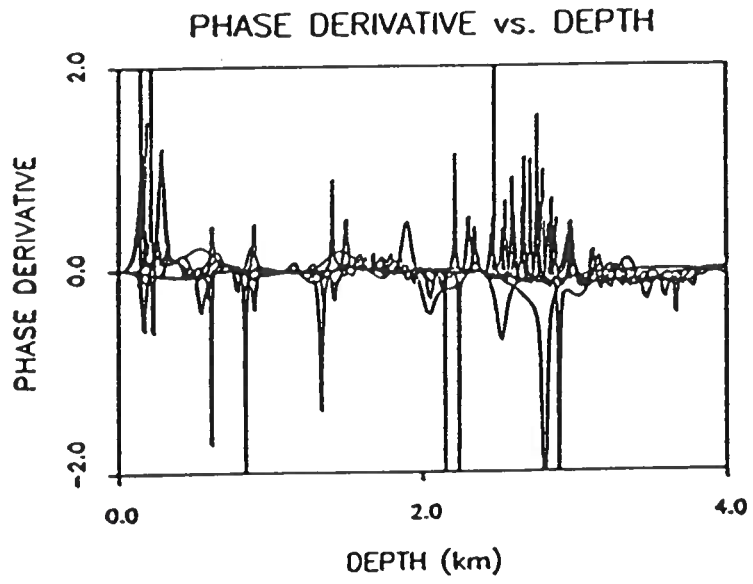

Figure 86. Derivative of the phase with respect to depth for 10 source frequencies generated using the profile and source-receiver geometry of test case 7. The range is 30 km.

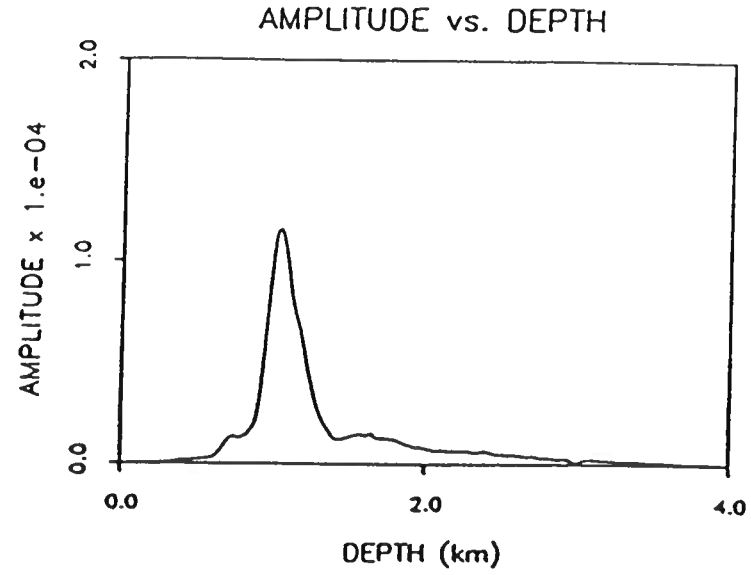

Figure 87. Frequency-averaged amplitude of DWB kernel generated using the profile and source-receiver geometry of test case 7. The range is 30 km.

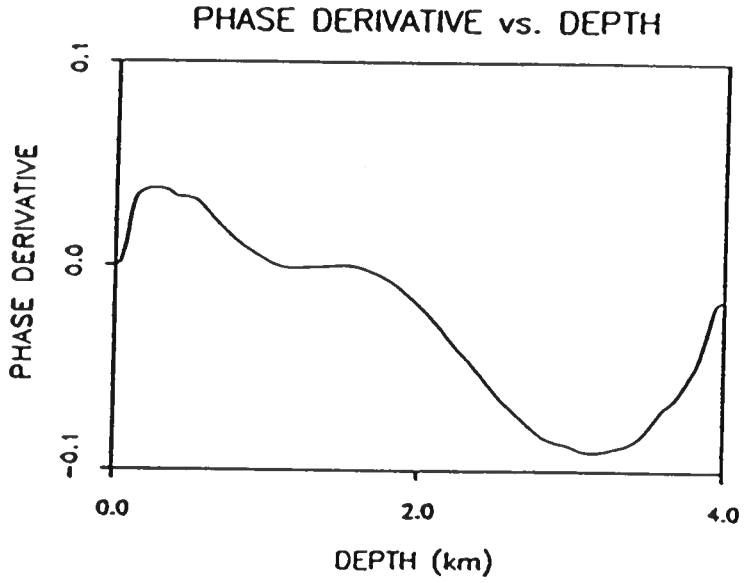

Figure 88. Frequency and depth-averaged derivative of the phase with respect to depth generated using the profile and source-receiver geometry of test case 7. The range is 30 km.